

Computational Investigation of Crystalline and Amorphous Borosilicates

Abdul Ghaffar Rashidi

Supervisors: Prof. C. R. A. Catlow, Dr R. G. Bell, and Dr A. Takada

Centre for Doctoral Training in Molecular Modelling & Materials Science

Department of Chemistry

University College London

This thesis is submitted for the degree of Doctor of

Philosophy

Feb 2021

DECLARATION

I, Abdul Ghaffar Rashidi, submit this thesis as per guidelines specified by UCL. This thesis is submitted with full acknowledgement that the work provided is my own unless hereby specified. Where I have consulted the work of others, this has been specified and referenced.

Signed: Abdul Ghaffar Rashidi

Date: 26/02/2021

ABSTRACT

By utilising both Molecular Dynamics (MD) and Density Functional Theory (DFT), the project focuses on the structure and bonding in glassy and crystalline boron oxide and borates, particularly on the distribution of BO_3 and BO_4 groups through ring and structural analysis and on the bonding and structural properties of borates. There are two main areas of this research: the first section presents the results of the computational investigation of Boron Trioxide (B_2O_3) via MD. The second focuses on the alkali-infused crystalline borates to understand their network structure in detail.

The MD component of this investigation concentrates on pure B_2O_3 including the crystalline, molten, and glassy structure. The atomic structure of this material is one that has been widely debated and was a key topic in this project. Characteristics are identified through various structural and mechanical properties and *via* ring analysis. The results of the initial MD simulations indicate a substantial proportion of BO_3 groups present in the structure of pure B_2O_3 (87.5%). However, expanding the simulation cell size reveals an increase in the BO_4 subgroup, indicating a possibility of an increase in boroxol ring formation, this finding demonstrates the need for large simulation cells which is now possible with contemporary computational resources

The thesis then focusses on the testing and identification of a force field to utilise in the MD studies. It explores the two available force fields, containing two- and three-body terms and shows that both can model the molten structure. However, as the

quenching of the simulation takes place, the two-body potential fails to adequately create the glassy phase; whereas the potential with the three-body term is able to achieve the glassy-B₂O₃ structures at a much quicker rate.

Crystalline borates with a range Na₂O/B₂O₃ ratios are next investigated using Density Functional Theory. Various crystals compositions are analysed, with a focus primarily on electronic and mechanical properties. We show that an increase in sodium content in these types of crystals has a direct effect on elasticity and mechanical strength. The results reveal interesting aspects of the bonding in these materials and give insight into the relationship between structure and composition.

ACKNOWLEDGEMENTS

I would like to kindly thank Prof. Richard Catlow, Dr Robert Bell and Dr Akira Takada for their supervision for the length of this project. Thank you for allowing me to be part of this research. I am very grateful for Dr John Buckeridge and Dr Jamie Christie for all their help. Thank you to Dr Zhimei Du, for all your support throughout my journey here at UCL. I appreciate all the help and advice along the way. I would like to thank the EPSRC, Asahi Glass Company and the UCL doctoral centre for supporting my research.

A special thanks to all the students in Room 205! Qamreen thanks for laughing when no-one else did. You helped me enjoy those small funny moments and you are such a motivating spirit. I appreciate you for supporting me through my cookie addiction...perhaps accelerating the problem but I'm grateful. Amy, you were my musical buddy! I loved your positivity despite this journey and thank you for entertaining my crazy even when you might not want to. Emilia, you're literally the person people will say they want to grow up to be like. Last but not least my family who were the most supportive and patient for the entire duration of this project. Thank you so much.

IMPACT STATEMENT

Context

The scope of research into the area of 'glass' has an impact on the practicality of everyday materials for industrial and public use. There has been a huge increase in technological and chemical advances in glass used in applications within mobile screens, architecture, and art.

Research into one of the most common types of glass, borosilicate, has been of focus for scientists across the globe over the past decade. In these glasses, silica is the major component and has been analysed thoroughly. A literature search on 01/02/2018 of "*silica glass*" shows 1,436 papers being published just in the past 5 years. However, the second major component of this type of glass is known as boron trioxide which also has the ability to form glass solely. Despite this molecule being a significant component (usually 5-20% in borosilicates), when searching for "*boron trioxide glass*" in *PubMed*, only 3 papers have been published in the past 10 years, all related to boron trioxide glass being infused with other material.

Approach to Impact

As the problem area has been identified, we must identify the approach. Experimentally, research into this area can be time-consuming, dangerous (due to high temperatures) and expensive (costs of furnaces and composition of glasses). The conditions are unique and complex; therefore, a computational approach was undertaken.

Within academia, the content of this research can help identify the great significance of boron trioxide within borosilicate glass, and also, it's potential as a sole glass former. There has been little research into this material; comparisons to boron trioxide with alkali oxide addition can be significant in network structure identification and manipulation for properties to help with experimental use.

Industrial Use

The potential users include the co-sponsors of this project, Asahi Glass Company (AGC) Inc. AGC is a Japanese based company who works on manufacturing glass across the world and is one of the industry leaders in glass production. The products and areas include display glasses, automotive material, electronics, and optics. They are particularly known for being the largest flat glass producers in the world, extending over 30 regions based particularly in Asia, Europe, and America. The company's R&D structure is based over a three-part process, which focuses on Intellectual Property, business development and productivity innovation. Universities play a role in aiding

both short and long-term market perspective missions. My research can potentially help with the production process and in turn, help with resource balance and scientific innovation through understanding the network alongside the chemical and mechanical properties. This is through understanding optimal conditions for formation at each step of the glass formation process. Furthermore, the results of alkali oxide addition provide more information for industrial user to help identify the glass structure and how this can be modified to suit commercial needs.

CONTENTS

1 Introduction.....	28
1.1 PROJECT SCOPE.....	28
<i>1.1.1 History of Glass</i>	<i>29</i>
1.2 PRODUCTION.....	31
<i>1.2.1 Conventional Method of Glass Formation</i>	<i>35</i>
<i>1.2.2 Unconventional Methods of Glass Formation.....</i>	<i>36</i>
1.3 GLASS FORMATION	38
<i>1.3.1 Glass Transition State.....</i>	<i>38</i>
<i>1.3.2 Zachariassen's Rules.....</i>	<i>40</i>
<i>1.3.3 Glass Network.....</i>	<i>43</i>
1.3.3.1 Network Former.....	44
1.3.3.2 Modifiers and Intermediates.....	45
1.3.3.3 Other Constituents.....	47
1.4 TYPES OF GLASS	47
<i>1.4.1 Natural Glass.....</i>	<i>47</i>
<i>1.4.2 Inorganic Glass.....</i>	<i>48</i>
1.5 GLASS APPLICATION	50
1.6 RESEARCH AREA.....	54

<i>1.6.1 Borosilicate Glass</i>	54
1.6.1.1 Boron Trioxide Structure.....	60
1.6.1.2 Borate Systems.....	66
1.6.1.3 Previous Structural Research.....	67
1.6.1.4 Specific Project Objectives	70
1.6.1.5 Thesis Layout.....	71
2 Methodology: Molecular Dynamics	73
2.1 EQUATIONS OF MOTION	73
2.1.1 <i>Finite Difference Methods</i>	76
2.2 TIME STEP	76
2.3 VELOCITIES	77
2.4 PERIODIC BOUNDARY CONDITIONS.....	78
2.5 FORCE FIELDS/POTENTIALS	79
2.6 ENSEMBLES.....	82
2.6.1 <i>Constant Temperature</i>	83
2.6.2 <i>Constant Pressure</i>	83
2.7 ANALYSIS TOOLS	83
2.7.1.1 Radial Distribution Function.....	84
2.7.1.2 Mean Squared Displacement.....	86

2.8 COMPUTATIONAL PROGRAMS	88
2.8.1.1 DL_POLY	89
2.8.1.2 Benchmarking	89
3 Force Field Investigation	91
3.1 ABSTRACT.....	91
3.2 AIMS AND INTRODUCTION.....	92
3.3 COMPUTATIONAL DETAILS	93
3.5: RESULTS AND DISCUSSION.....	96
3.3 <i>Interatomic Potential Models</i>	96
3.3.2 <i>The Two-Body Potential</i>	98
3.3.1 <i>The Three-Body Potential</i>	100
3.5. <i>RDF Data</i>	101
3.3.1.1 Atomic Diffusion	105
3.3.1.2 Atomic Diffusion	108
3.3.2 <i>Comparison of Force Field Performance for B₂O₃ Crystal, Melt and Quench structures</i>	109
3.4 SUMMARY AND CONCLUSIONS.....	111
4 Molecular Dynamics Studies on Boron Trioxide	112
4.1 ABSTRACT.....	112

4.2 AIMS AND INTRODUCTION.....	113
4.3 STRUCTURAL MODEL AND COMPUTATIONAL DETAILS	114
4.4 RESULTS AND DISCUSSION.....	117
4.4.1.1 Radial Distribution Functions	117
4.4.1.2 Density and Enthalpy	120
4.4.2 Molten B_2O_3 System.....	121
4.4.2.1 Molten B_2O_3 Substructure Analysis	125
4.4.3 Quenching the System.....	129
4.5 COMPARISON OF THE THREE B_2O_3 PHASES	130
4.5.1 RDF comparison.....	132
4.5.2 Diffusivity analysis.....	136
4.6 CHAPTER CONCLUSION	137
5 Boron Trioxide : Larger Simulation Cells.....	138
5.1 ABSTRACT.....	138
5.2 AIMS AND INTRODUCTION.....	139
5.3 COMPUTATIONAL DETAILS	139
5.4 RESULTS AND DISCUSSION.....	141
5.4.1 B1 System.....	141
5.4.2 C1 System.....	142

5.4.3 <i>Bond and ring analysis</i>	143
5.5 CHAPTER CONCLUSIONS	145
6 Methodology: Electronic Structure methods	147
6.1 ABSTRACT.....	147
6.2 SCHRÖDINGER EQUATION	148
6.2.1 <i>Born-Oppenheimer Approximation</i>	149
6.3 DENSITY FUNCTIONAL THEORY	150
6.3.1 <i>Hohenberg-Kohn Theorem</i>	151
6.3.2 <i>Kohn-Sham Theory</i>	152
6.3.3 <i>Exchange-Correlation</i>	153
6.3.4 <i>Local Density Approximation</i>	153
6.3.5 <i>General Gradient Approximation</i>	154
6.4 ANALYSIS OF DFT OPTIMISED STRUCTURES.....	154
6.4.1 <i>Band Structure</i>	155
6.4.2 <i>Density of states</i>	155
6.4.3 <i>Thermal Stress / Temperature Stress Point</i>	156
6.4.4 <i>Pulay Stress</i>	157
6.5 ELASTIC/MECHANICAL PROPERTIES	157
6.5.1 <i>Bulk Modulus</i>	158
6.5.2 <i>Young's Modulus/Elastic Constant</i>	159

6.5.3 Dielectric Function	160
6.6 VASP.....	160
6.7 POLYHEDRA ANALYSIS	161
7 Electronic Classification of B₂O₃ Crystals.....	162
7.1 ABSTRACT.....	162
7.2 AIMS AND INTRODUCTION.....	163
7.3 COMPUTATIONAL DETAILS	164
7.4 RESULTS AND DISCUSSION	165
7.4.1 B ₂ O ₃	165
7.4.2 Caesium Enneaborate. Crystal, Cs ₂ O(B ₂ O ₃) ₉	167
7.4.3 Porosity.....	169
7.5 CHAPTER CONCLUSIONS	172
8 Sodium Borate Crystal	173
8.1 ABSTRACT.....	173
8.2 AIMS AND INTRODUCTION.....	174
8.3 COMPUTATIONAL DETAILS	175
8.4 RESULTS AND DISCUSSION.....	176
8.4.1 Disodium Borate Na ₄ B ₈ O ₁₄	176

Computational Investigation of Crystalline and Amorphous Borosilicates

8.4.1.1 Structural Analysis of $\text{Na}_4\text{B}_8\text{O}_{14}$	176
8.4.1.2 $\text{Na}_4\text{B}_8\text{O}_{14}$ Polyhedra	177
8.4.1.3 $\text{Na}_4\text{B}_8\text{O}_{14}$ Ring and Bonding Info.....	179
8.4.1.4 $\text{Na}_4\text{B}_8\text{O}_{14}$ Electric and Elastic Properties	184
8.4.1.4.1 Dielectric Properties.....	184
8.4.1.4.2 Mechanical Properties.....	186
8.4.1.4.3 $\text{Na}_4\text{B}_8\text{O}_{14}$ Charge Density	189
8.4.2 Monosodium Borate $\text{Na}_{36}\text{O}_{72}\text{B}_{36}$.....	191
8.4.2.1 $\text{Na}_{36}\text{O}_{72}\text{B}_{36}$ Structural Information	191
8.4.2.2 $\text{Na}_{36}\text{O}_{72}\text{B}_{36}$ Polyhedra	194
8.4.2.3 $\text{Na}_{36}\text{O}_{72}\text{B}_{36}$ Elastic Properties.....	195
8.4.2.4 $\text{Na}_{36}\text{O}_{72}\text{B}_{36}$ Density of States	196
8.4.2.5 $\text{Na}_{36}\text{O}_{72}\text{B}_{36}$ RDF.....	198
8.4.3 $\text{B}_7\text{Na}_3\text{O}_{12}$ Crystal.....	199
8.4.3.1 $\text{B}_7\text{Na}_3\text{O}_{12}$ Polyhedra	200
8.4.3.2 $\text{B}_7\text{Na}_3\text{O}_{12}$ Density of States	201
8.4.3.3 $\text{B}_7\text{Na}_3\text{O}_{12}$ Elastic Properties	202
8.5 CHAPTER CONCLUSIONS	203
9 Conclusion and Future Work	205
10 Bibliography	209

LIST OF TABLES

Table 1 - Zachariasen's Rules (34–36).....	42
Table 2 - Cell parameter comparison obtained from experimental data and through this computational investigation of both A1 and B1 systems.	93
Table 3 - Heating conditions and rates used within this research	95
Table 4 - Two Body Potential used in the simulation with the variables.	99
Table 5 - Additional three-body terms added to the Potential	100
Table 7 - RMSD from Crystal to Glass Phase.....	106
Table 8 – Polyhedra representation of the pure crystalline B ₂ O ₃ system together with a table containing volumetric and coordination number data.	110
Table 10 - Breakdown of the total energy for the equilibrated B ₂ O ₃ system.....	120
Table 11 – Image showing 10-membered ring structure distance and angular values with the corresponding reference image	128
Table 12 - B1 and C1 system computational information	140
Table 13 - Comparison of structural information on calculated D1 and Caesium Crystals.....	168
Table 14 – Calculated polyhedron comparison of atoms within the caesium- containing crystal.....	171
Table 16 - Polyhedra data for the Na ₄ B ₈ O ₁₄ crystal.....	178
Table 17 - Boroxol ring found within Na ₄ B ₈ O ₁₄ and corresponding structure data. .	179
Table 18 - Four-Membered ring information found within the Na ₄ B ₈ O ₁₄ system.	183

Table 19 - Table showing both the calculated High frequency and Static Tensors of the $\text{Na}_4\text{B}_8\text{O}_{14}$.	185
Table 20 - Elastic Constants expressed in GPa for the $\text{Na}_4\text{B}_8\text{O}_{14}$ system.	186
Table 21 - Average bonding within the $\text{Na}_{36}\text{O}_{72}\text{B}_{36}$.	192
Table 22 - Data for four-membered rings in $\text{Na}_{36}\text{O}_{72}\text{B}_{36}$.	194
Table 23 - Polyhedra data with respect to the Monosodium crystal.	195
Table 24 - Elastic Constant Calculations for $\text{Na}_{36}\text{O}_{72}\text{B}_{36}$.	195
Table 25 - Polyhedra data for $\text{B}_7\text{Na}_3\text{O}_{12}$.	200
Table 26 – Calculated elastic constants (in GPa) calculated in the Voigt notation for $\text{B}_7\text{Na}_3\text{O}_{12}$.	202
Table 27 - The B-O bond distances for each of the crystal structures investigated in this reasearch, indicating crystal ratio and configuration. Where X specifies the Alkali Oxide investigated.	203

LIST OF FIGURES

FIGURE 1 - INITIAL RAILROAD LANTERNS WHICH USED SODA-LIME GLASS. ⁽⁸⁾	30
FIGURE 2 - GLASS MADE WITH MANGANESE DIOXIDE UNDER A BLACKLIGHT. ⁽¹⁵⁾	33
FIGURE 3 - GLASS MANUFACTURING PROCESS.....	34
FIGURE 4 -SCHEMATIC SHOWING GLASS-CERAMICS. HIGHLIGHTING THE CONVENTIONAL AND INCORPORATION METHOD.....	36
FIGURE 5 - NEW METHOD FOR FLAT GLASS PRODUCTION WITH ATTEMPTS TO REDUCE HIGH ENERGY RECOVERY POTENTIAL. ⁽²²⁾	37
FIGURE 6 - GRAPH HIGHLIGHTING THE GLASS TRANSITION TEMPERATURE.	39
FIGURE 7 - CRYSTAL VS GLASS NETWORKS SHOWING THE MORE DEFINED, PERIODIC CRYSTAL STRUCTURE, AND THE INTERMEDIATE RANGE ORDER WITH THE GLASS NETWORK.	44
FIGURE 8 - IMAGE HIGHLIGHTING AN EXAMPLE NETWORK FORMER Si^{4+} AND MODIFIER ION, Na^+	46
FIGURE 9 - THE NATURALLY FORMED OBSIDIAN GLASS (LEFT) AND A POLISHED AND CUT VERSION OF THE VOLCANIC MATERIAL (RIGHT). ⁽⁴⁶⁾	48
FIGURE 10 - IMAGE TO SHOW PURE SILICA NETWORK. RED SPHERES ARE OXYGEN ATOMS, WHILST THE GREY ATOMS REPRESENT THE SILICON WITH THE SURROUNDING BLUE POLYHEDRA. ⁽⁴⁹⁾	49
FIGURE 11 - AN INDUSTRIAL EXAMPLE OF NUCLEAR WASTE CONTAINMENT USING GLASS. ⁽⁶⁰⁾	52

FIGURE 12 - A TYPICAL BOROSILICATE GLASS STRUCTURE ADAPTED FROM *BOLTRES ET AL.* ⁽⁶⁵⁾55

FIGURE 13 - GLASS BEING USED WITHIN PIPE COOLANT SYSTEMS IN A MOTOR VEHICLE. ⁽⁸⁰⁾59

FIGURE 14 - IMAGE SHOWING STRESS TESTING OF CHEMICALLY STRENGTHENED GLASS TO BE USED FOR
 SCREENS IN PHONES, TABLETS, AND OTHER ELECTRONIC DEVICES ⁽⁸³⁾60

FIGURE 15 - BO_3 BUILDING BLOCK (LEFT) AND THE BOROXOL RING (RIGHT) THOUGHT TO IDENTIFY THE
 STRUCTURE OF G- B_2O_361

FIGURE 16 - 4 DIFFERENT CONFIGURATIONS OF B_2O_3 UNITS WHICH MAINTAIN THE SAME TOPOLOGY.
 DENSITY IS REDUCED BY A $\frac{1}{4}$ FROM STRUCTURE 1 TO 4. *ADAPTED FROM PYE ET AL.* ⁽⁸⁸⁾62

FIGURE 17 - SCHEMATIC OF THE MC STEPS FOR CREATING PSEUDO-CRYSTAL STRUCTURES FROM B_2O_3 -I
 CRYSTALS.65

FIGURE 18 - BORATE GLASSES DISPLAYING TYPICAL RING STRUCTURES. ⁽⁹⁵⁾66

FIGURE 19 - BLACK CIRCLES ARE BORON, GREEN CIRCLES ARE HYDROGEN AND RED ARE OXYGEN
 ATOMS. *ADAPTED FROM THE CRYSTAL LATTICE OF BORIC ACID, BO_3H_3* ⁽¹⁰¹⁾68

FIGURE 20 - IMAGE SHOWING THE SIMILARITIES OF LAYERING BETWEEN GRAPHITE AND BORON NITRIDE
⁽¹⁰⁴⁾69

FIGURE 21 - SCHEMATIC SHOWING A GENERALISED MD SIMULATION ROUTE.75

FIGURE 22 - IMAGE SHOWING EFFECTS OF PERIODIC BOUNDARY CONDITIONS.78

FIGURE 23 -LENNARD JONES POTENTIAL DEPICTING THE ATTRACTIVE AND REPULSIVE FORCES. ⁽¹⁰⁸⁾ ...81

FIGURE 24 - A VISUALISATION OF SPACE SEPARATION FOR THE EVALUATION OF THE RADIAL DISTRIBUTION FUNCTION..... 85

FIGURE 25 - TYPICAL MSD PLOT. 87

FIGURE 26 - BENCHMARKING DATA FOR DL_POLY 4 AGAINST DL POLY CLASSIC. 90

FIGURE 27- GRAPH TO SHOW ONLY THE HEATING STEPS FROM INITIAL MINIMISATION STEP TO 5000K. 94

FIGURE 28 - IMAGE SHOWING B-O BOND LENGTHS OF THE SIMULATED STRUCTURE WITHIN 8 Å OF INDEX 20..... 97

FIGURE 29 - IMAGE REPRESENTING TWO AND THREE-BODY INTERACTIONS..... 100

FIGURE 30 - GRAPHS SHOWING THE AVERAGE RDF FOR THE A) CRYSTAL, B) MELT AND C) QUENCH STAGES. THE BLACK SHOWING B-B INTERACTION, RED LINES SHOW B-O RDF'S AND GREEN FROM O-O..... 101

FIGURE 31 - RDF OF THE B₂O₃ SYSTEM USING THE THREE-BODY POTENTIAL. 102

FIGURE 32 - CALCULATED RDF PLOT OF GLASS FOR B-O AT 300K..... 104

FIGURE 33 - OXYGEN-OXYGEN RDF PLOT AT 300K DURING THE GLASSY PHASE. 105

FIGURE 34 – BALL-AND-STICK MODELS OF B₂O₃ OF CRYSTAL, MELT AND GLASS PHASES FOR THE TWO-BODY POTENTIAL, ALONGSIDE THEIR RESPECTIVE O-O RDFs. 107

FIGURE 35 – MSD PLOT FOR B AND O IN MELTED B₂O₃ USING THE TWO-BODY POTENTIAL (WITH BORON ATOMS IN BLACK AND OXYGEN IN RED). 108

FIGURE 36 - MSD PLOT B AND O IN MELTED B_2O_3 USING THE THREE-BODY POTENTIAL (WITH BORON ATOMS IN BLACK AND OXYGEN IN RED)..... 109

FIGURE 37 – B_2O_3 NON-RING SEGMENT HIGHLIGHTING THE SPECIFIC ATOMS..... 111

FIGURE 38 -THE BORON TRIOXIDE SUBUNITS; A) BO_4 , B) BO_3 AND C) BOROXOL RING. 113

FIGURE 39 – A1 SYSTEM FOR B_2O_3 THREEFOLD-COORDINATED BORON. VISUALISED USING VMD SOFTWARE 115

FIGURE 40 EVOLUTION OF THE TOTAL ENERGY OF A1 SYSTEM WITH TIME, DURING ZERO KELVIN MINIMISATION RUN. 116

FIGURE 41 - RDFs FOR MINIMISED A1 CRYSTAL WITH A ZOOMED SECTION TO HIGHLIGHT SIGNIFICANT PEAKS. 118

FIGURE 42 - BOROXOL RING LENGTH AS SUGGESTED BY MARANAS *ET AL.* ⁽¹³⁸⁾ 119

FIGURE 43 – EVOLUTION OF THE RING REFORMATION DURING B_2O_3 MELT PROCESS IN DIFFERENT STAGES. LABELS INDICATE CAPTURE AT THE CORRESPONDING TIMEFRAME WITH 1= 10ps, 2 = 250ps 3 = 500ps AND 4= 1ns. 122

FIGURE 44 - RDF OF A1 SYSTEM AT 5000K. ZOOMED SECTIONS ARE INSERTED TO HIGHLIGHT SIGNIFICANT PEAKS. 124

FIGURE 45 - IMAGE SHOWING BORIC ACID AND THE LAYERING EFFECTS. EACH COLOUR SHOWING A DIFFERENT LAYER CONNECTED THROUGH INTERMOLECULAR HYDROGEN BONDING. ⁽¹⁴⁴⁾ 125

FIGURE 46 - PIE CHARTS REVEALING COORDINATION WITHIN THE SYSTEM FOR BOTH BORON AND OXYGEN ATOMS.	126
FIGURE 47 - IMAGE SHOWING A 4-MEMBERED RING HIGHLIGHTED WITH CORRESPONDING DISTANCE AND ANGLE INFORMATION.	127
FIGURE 48 - RDF OF A1 SYSTEM AT 300K IN THE GLASSY PHASE WITH A ZOOMED SECTION TO HIGHLIGHT SIGNIFICANT PEAKS.	129
FIGURE 49 - EFFECTS ON RMSD VALUE AGAINST CHANGES IN TEMPERATURE. THE MAXIMUM TEMPERATURE AT 5000K. THE BLUE HIGHLIGHTS THE QUENCHING TEMPERATURES (ATOM AVERAGES / Å)	131
FIGURE 50 - RDF FOR BO FOR ALL TEMPERATURES INVESTIGATED. THE KEY INDICATES THE TEMPERATURE OF THE SIMULATION RUN IN KELVINS.	133
FIGURE 51 - RDFs FOR BB FOR ALL TEMPERATURES INVESTIGATED.	134
FIGURE 52 - RDFs FOR OO FOR ALL TEMPERATURES INVESTIGATED. THE KEY INDICATES THE TEMPERATURE OF THE SIMULATION RUN IN KELVINS.	135
FIGURE 53 - DIFFUSION COEFFICIENTS FOR B AND O IN A1 SYSTEM. THE Q2500 AND Q300 VALUES INDICATE THE QUENCH STEPS.	136
FIGURE 54 – POLYHEDRA GRAPHICAL REPRESENTATION OF THE B1 SYSTEM VISUALISED IN THE VESTA PROGRAMME. THE RED ARE THE OXYGEN ATOMS WITH THE GREEN INDICATING THE POLYHEDRA SURROUNDING THE BORON ATOM.....	141
FIGURE 55 – 2X2X2 B ₂ O ₃ SUPERCELL, C1.....	143

FIGURE 56 - DISTRIBUTION OF O-B-O ANGLE IN THE B1 (RED LINE) AND C1 SYSTEMS (BLACK LINE). 144

FIGURE 57- CALCULATED STRUCTURE OF CALCULATED CRYSTAL B_4O_6 165

FIGURE 58 - CALCULATED POLYHEDRAL REPRESENTATION OF THE $CS_2O(B_2O_3)_9$ CRYSTAL. CS IS IN
CENTRE OF LARGE POLYHEDRA WITH THE RED SPHERES REPRESENTING O AND B IN THE CENTRE OF
SMALL POLYHEDRA. EXPERIMENTAL DATA REPRESENTED BY (EXP.)⁽¹⁶²⁾ 167

FIGURE 59 - BOROXOL RINGS PRESENT IN THE CAESIUM CRYSTAL, WITH PINK AS THE BORON ATOMS AND
RED AS OXYGEN ATOMS. 171

FIGURE 60 – POLYHEDRA REPRESENTATION OF THE $NA_4B_8O_{14}$ SYSTEM SHOWING THE YELLOW SODIUM-
BASED POLYHEDRA AND THE GREEN BORON-BASED POLYHEDRA. RED REPRESENTS THE OXYGEN
ATOMS. 176

FIGURE 61 - POLYHEDRA IDENTIFIED WITHIN THE $NA_4B_8O_{14}$ CRYSTAL. GREEN HIGHLIGHTING THE
BORON POLYHEDRA AND YELLOW HIGHLIGHTING THE SODIUM-BASED POLYHEDRA. RED SPHERES
REPRESENT OXYGEN. 177

FIGURE 62 - DISTRIBUTION PLOTS OF INTERATOMIC DISTANCES WITHIN THE $NA_4B_8O_{14}$ STRUCTURE. 181

FIGURE 63 - THE STRUCTURAL EFFECT OF SODIUM ION ADDITION WITHIN BOROXOL RING. 182

FIGURE 64 - FOUR-MEMBERED RING STRUCTURES WITHIN THE $NA_4B_8O_{14}$ 182

FIGURE 65 – GRAPH PRESENTING PRESSURE AGAINST VOLUME TO CALCULATE THE VALUE OF THE BULK
MODULUS FOR THE $NA_4B_8O_{14}$ 188

FIGURE 66 - CHARGE DISTRIBUTION IN $\text{Na}_4\text{B}_8\text{O}_{14}$ WITH THE BLUE INDICATING SODIUM ATOMS AND THE PINK INDICATING BORON. GREEN DISPLAYS A CHARGE ISOSURFACE. 190

FIGURE 67 - $\text{Na}_{36}\text{O}_{72}\text{B}_{36}$ CRYSTAL..... 191

FIGURE 68 - $\text{Na}_{36}\text{O}_{72}\text{B}_{36}$ CRYSTAL DISPLAYING THE TWO BOROXOL RINGS PRESENT WITHIN THE SYSTEM. 192

FIGURE 69 - $\text{Na}_{36}\text{O}_{72}\text{B}_{36}$ CRYSTAL WITH THE YELLOW HIGHLIGHTING FOUR-MEMBERED RING..... 193

FIGURE 70 - DENSITY OF STATES FOR $\text{Na}_{36}\text{O}_{72}\text{B}_{36}$, A) SHOWING FULL DOS GRAPH AND B) ZOOMED IN TO INDICATE CONDUCTION BAND. 197

FIGURE 71 - RDFs FOR $\text{Na}_{36}\text{O}_{72}\text{B}_{36}$ 198

FIGURE 72 - POLYHEDRA HIGHLIGHTED FOR $\text{B}_7\text{Na}_3\text{O}_{12}$ WITH YELLOW HIGHLIGHTING THE NA-BASED POLYHEDRA AND GREEN INDICATING THE BORON-BASED POLYHEDRA. 199

FIGURE 73 - DENSITY OF STATES FOR $\text{B}_7\text{Na}_3\text{O}_{12}$ 201

FIGURE 74 - COMPARISONS OF MECHANICAL PROPERTIES FOR THE SODIUM BORATE CRYSTALS INVESTIGATED..... 207

LIST OF ABBREVIATIONS AND ACRONYMS

AGC : Asahi Glass Company Inc.	3
AIM : Atoms in Molecules Theory.....	151
B ₂ O ₃ : Boron Trioxide.....	21
B ₇ Na ₃ O ₁₂ : Sodium Triborate.....	163
BKS : van Beest, Kramer and van Santen potential	119
BO ₃ : Triangular Sub-unit of Boron Trioxide	59
BO ₄ : Tetrahedron subunit of Boron Trioxide	59
BOpp : Born-Oppenheimer	61
CaO : Calcium Oxide.....	36
DFT : Density Functional Theory	89
DOS : Density of States	150
eV: Electron Volts.....	87
GGA : Generalised Gradient Approximation.....	146

GUI : Graphic User Interface	113
HLW : High Level Nuclear Waste	43
IR : Infrared	107
LDA : Local Density Approximation.....	145
LP: Linear Programming.....	122
MC : Monte Carlo.....	53
MD : Molecular Dynamics.....	49
MgO : Magnesium Oxide	36
MSD: Mean Squared Displacement	73
Na ₂ CO ₃ : Sodium Carbonate	24
Na ₃₆ O ₇₂ B ₃₆ : Sodium Monoborate	163
Na ₄ B ₈ O ₁₄ : Sodium Diborate	163
NMR : Nuclear Magnetic Resonance	52
NPT: Isothermal-Isobaric Ensemble.....	69
NVE: Microcanonical Ensemble	69
NVT: Canonical Ensemble	69
N σ T: isothermic-isobatic ensemble.....	70

OB : Bridging Oxygen	36
ONB : Nonbridging Oxygen	36
P ₂ O ₅ : Phosphorus oxide.....	40
PBC: Periodic Boundary Conditions	65
PBE : Perdew-Burke-Ernzerhof	146
QTAIM : Quantum Theory of Atoms in Molecules	151
RA : Radioactive	43
RDF: Radial Distribution Function	71
RMSD : Root Mean Squared Deviation	100
RNT : Random Network Theory	33
SAXS : Small-Angle X-Ray Scattering.....	32
SiO ₂ : Silica/ Silica Dioxide.....	21
T _g : Glass Transition Temperature	29
T _m : Melting Temperature.....	29
VAF : Velocity Autocorrelation Function	107
VASP: 'Vienna ab initio Simulation package' program	140
VESTA : 'Visualisation for Electronic and Structural Analysis' program	87

VMD : Visualisation Molecular Dynamics Software	75
VSEPR : Valence Shell Electron Pair repulsion	151
XRD : X-ray Powder Diffraction	50

1 INTRODUCTION

1.1 Project Scope

The focus of this study is the analysis of pure Boron Trioxide, B_2O_3 , and various alkali-borate crystals, to investigate the material's network in terms of both structure and electronic properties.

B_2O_3 was selected in this research for its ability to form glass without any metal oxide addition. The motivation comes from attempting to understand the role the B_2O_3 boroxol rings and planar trigonal subunits play in the crystal to glass transformation in borosilicate materials. This is a research question that has been key in borosilicate crystal and glass exploration, as models of the network structure have varied considerably as explored later in this chapter. The structure is, of course, linked to the chemical and mechanical properties; hence the identification of structural properties can further increase our understanding of the properties of the materials. More importantly, we can understand how, as the structure changes, the network varies and how this affects the material's properties. Study of these problems is particularly suited to computational techniques, owing in part to the difficulty and expense of experiment.

There is a large focus in contemporary glass science on borosilicate glasses in which silica, SiO_2 , is the primary component. SiO_2 has many unique properties including

excellent transmission characteristics and high purity in the naturally forming material. Nevertheless, the B_2O_3 subunit is the second-largest component in the majority of these types of glasses. Moreover, B_2O_3 itself is a glass former meaning no other materials are required, which provides a suitable area to study for industry/application improvements. Therefore, the study of B_2O_3 is a key and interesting area of scientific exploration.

1.1.1 History of Glass

Glesum is the Latin term for amber which is a glossy and transparent material and glassy materials were widely used in the ancient world. The definition of glass is complex and varied. What is established is that a glass is a hard and transparent material, which exhibits great durability when exposed to natural changes such as fluctuations in temperature. It is often described as an “*inorganic product of fusion that has cooled to a rigid condition without crystallization*”.⁽¹⁾ The unique properties of glass elude a unique classification as either solid or liquid, which we will discuss later.^(2,3)

Natural volcanic glasses have been known for millennia. These glasses are exceptional substances, sparking interest even in today’s research. Although the first man-made glass dates back to 3500 BCE in Mesopotamia, glassy materials have only been studied extensively over the past 200 years, stimulated by their importance in a variety of industries and through their exceptional properties.^(4,5)

The plethora of uses come from glasses' unique properties which include thermal resistance and many optical properties. At the start of the 20th century, manufacturing signal lanterns for railroads (**Figure 1**) posed some difficulties due to the use of soda-lime glasses. The major issue with these lanterns was the fact that they were not weatherproof and had poor heat resistivity. Notably, the use of kerosene within these lamps would cause some expected thermal expansion. However, when it was then exposed to the cold weather, the lanterns would shatter. To combat this issue, American scientists - Corning researchers - thought to combine sand mixtures with Pyrex. Pyrex is the trademark name for glass containing sodium borate or borax. This newly formed glass was now ideal to use in lanterns but was later discovered to have applications in other industries such as heat resistant plates and bowls. ^{(6) (7)}



Figure 1 - Initial railroad lanterns which used soda-lime glass. ⁽⁸⁾

Modern-day research into glass has led to a variety of uses which are explored in section 1.5. What really brings scientists and manufacturers to the study of glass is simply its unique physical and chemical properties. The glassy state is one that has

long challenged researchers. One approach is to describe glass as a frozen or highly viscous liquid. This approach was suggested primarily due to the manner in which the windowpanes of European Medieval cathedrals were thicker at the bottom than at the top. This unusual behaviour encouraged the view that glass was a liquid. This model was also supported though the way in which the glass prepared (see *section 1.2*). ⁽⁹⁾

On the other hand, it was also suggested that glass was a solid that melts at an extremely slow rate giving a reason to the oddly shaped panes.

The modern approach focuses on atomic level structure defining a glass as an amorphous solid i.e., one lacking in long range periodicity – prepared by a melt quench method as discussed below, the properties can show similarities akin to both solid and liquid, which is further clarified when we consider the process in which glass is made.

1.2 Production

The first artefacts made from glass can be dated back to 3100BC in ancient Egypt. The current use of glass moulds/parison is a method that can be dated to 1500BC in Syria. The production techniques of this glass are still not well known, and it was not until 650BC that the first glass manuscript was published detailing how glasses were made. This manual was found in Assyrian king Assurbanipal's Library detailing production and mixture specifics. As the history of glass shows, the techniques with which this material is produced have been thoroughly explored and developed to provide the best possible material. Glass blowing was invented in the Babylonian era and is still a

procedure used today. The colouration of glass and creative designs were strongly influenced by the Islamic culture during 600-700 AD and led to an extensive exploration of applications. The commercial use into micro- and telescopic lenses were not developed until 1590 in the Netherlands. The topics of optics and refractive properties were thoroughly explored. ⁽¹¹⁾

Commercialised glasses usually have similar compositions, which consist of the major component, pure silica (SiO_2), sodium carbonate (soda ash, Na_2CO_3), B_2O_3 and metal oxides such as sodium and aluminium oxide. The proportion of components is specific for certain desired properties. Barium, for example, provides an increase in refractive index. Thorium oxide is used for high-quality lenses since it has a high refractive index and low dispersion values. When iron is infused in the glass, it has an ability to absorb Infrared energy and can then be utilised as a filter in movie projectors to absorb any heat and is particularly useful for architectural glass and eyewear. These are just to name a few interesting and unique additions to the composition; a variety of other components exists and are also utilised. ⁽¹²⁻¹⁴⁾

Apart from silica-based glass, there are many organic and inorganic glasses such as plastics which can form acrylic glass, phosphate, and fluoride glasses. Experiments have been performed to form coloured glass, which is obtained *via* the addition of small amounts of charged ions *via* a precipitation method of dispersion. Some examples include iron (II) oxide and manganese dioxide which are added to vary the amount of green tint, **Figure 2** ⁽¹⁵⁾



Figure 2 - Glass made with Manganese Dioxide under a blacklight. ⁽¹⁵⁾

There are two main methods to prepare glass samples, the float glass method and the glass blowing technique. Both techniques have been utilised for centuries with the former being an advancement to the preparation of this type of material. The two methods involve the same starting material but involve a procedural difference which helps create glasses of various shapes and dimensions. ^(16–18)

Glass blowing is the earliest method known to create man-made glass. For jars, vases, bulbs, and products that require a larger and more rounded shape, this technique is used. Although the steps can vary, the general process remains the same. When the raw materials are melted, they are collated to form a parison (rounded mass of glass). This is then placed within a mould by an individual or mechanically pressed in. This mould is placed within another container known as the Blow/Finishing Mould, which helps shape the glass by varying the pressure applied by compressed air “blown” in. Some methods use a ‘drawing’ phase which elongates the glass to create tubes and rods. ⁽¹⁹⁾

On the other hand, the float glass technique utilises a bed of molten metal and/or alloys which the molten raw materials are flowed over, which is particularly advantageous for creating material for industrial use since the method creates a product with uniform thickness with a level surface. In 1843, Henry Bessemer introduced the earliest form of 'Float Glass' methods. Currently, factories for large-scale production help create these glass sheets at high quality, **Figure 3**. Large furnaces adequately melt the batch products at very high temperatures and the molten material "floats" onto a bath, which is usually tin, in an inert atmosphere in order to avoid any oxidation that may take place. The motive behind using the bath is that as the molten product flows along the tin, the temperature is slightly cooled. The speed at which the molten glass is fed into the bath, helps influence the thickness of the sheets. The glass is then annealed and cut *via* automated machinery as required. The advantage of this method is that glass produced this way requires little to no polishing and edge smoothing. ⁽²⁰⁾

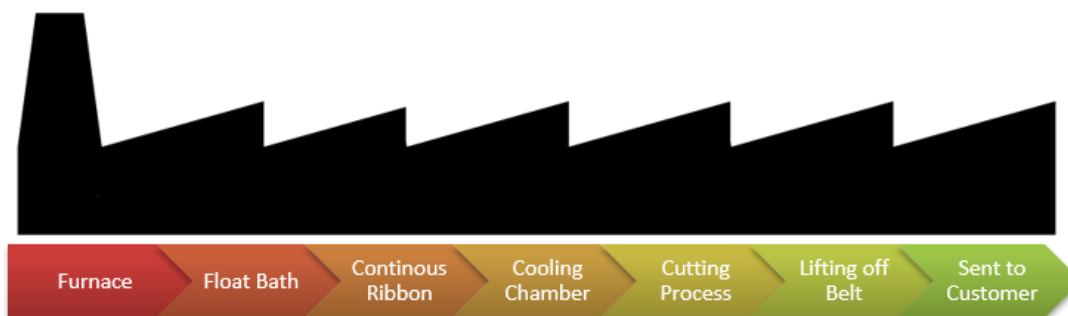


Figure 3 - Glass Manufacturing Process.

1.2.1 Conventional Method of Glass Formation

The oldest and most commonly used method involves three main steps. The first begins with combining crystals and other such material from which the user would like to create glass. Often known as the *Melt-Quench Technique*, as the name suggests, the product undergoes cycles of heating and quenching steps. The material is melted in a furnace: sometimes more than one furnace is used to heat at several temperatures and durations of time, so as the molten state is formed it is subsequently quenched at extreme rates, resulting in the solid glassy phase being formed. The quenching method sometimes varies, for example utilising condensation methods from vapour and using pressure quenching procedures. The quenched material is usually poured either into a mould or layered into thin sheets depending on industrial or commercial use. It is common to cut and polish the sample at the final stage so that material does not have sharp edges. **Figure 4** displays a schematic that shows a basic route in which conventional and incorporation routes are shown. ⁽²¹⁾

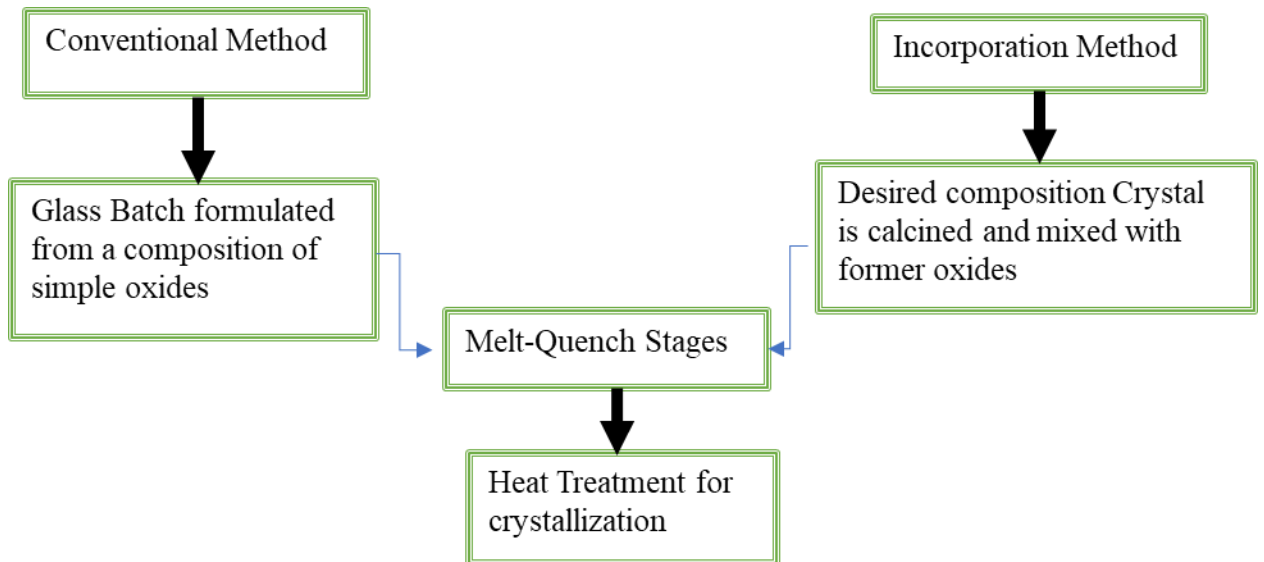


Figure 4 -Schematic showing glass-ceramics. Highlighting the conventional and incorporation method.

1.2.2 Unconventional Methods of Glass Formation

Scientific research has come a long way, developing traditional procedures into more technology-driven methods, **Figure 5** shows the complex, new procedure to form glass, with the recycling of excess heat for use in power turbines and generators.

Another example of a novel method includes bombardment by neutrons. In one example this involves phosphorus ion implantation within the glass surface and the addition of phosphorus. The silica-based glasses studied are especially effective for radiotherapy due to their biological effectiveness as they can withstand the body's internal environment. A disadvantage to this method is that when it is compared to

conventional techniques, this process is not only more complex but highly expensive.

(22,23)

For industrial use, it is sometimes required for the glass to be in the form of fibres or films. Although this is possible *via* traditional methods, research has led towards reducing costs and improving the quality of the products. Sometimes newer methods involve a combination of processes, where the float glass technique is utilised initially and then another method is carried out, so those specific requirements are met.

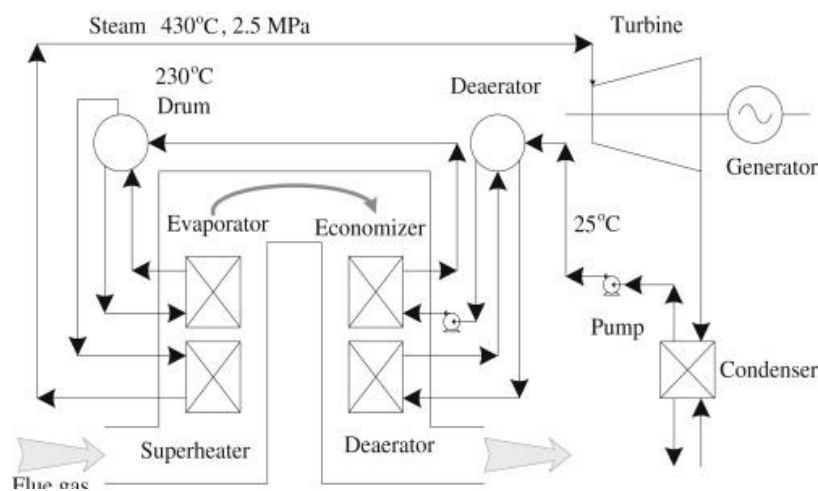


Figure 5 - New method for flat Glass production with attempts to reduce high energy recovery potential. (22)

An example of this is creating thin silica films. A method that has been devised is using an acidic solution which is spread on top of the glass which helps keep the thin form of the glass. However, techniques are still being investigated and are constantly replaced to ensure the glass production is both economically viable and of the highest quality. (24–26)

1.3 Glass Formation

1.3.1 Glass Transition State

The production of glasses gives a broad indication of how they are formed, but the details reveal unique changes in both the physical and chemical characteristics, which help to create a greater understanding of how exactly glass as a material is created at an atomistic level.

To form a glassy material the process involves heating a crystalline material to very high temperatures and a rapid cooling stage. During these stages, there are a few transitional steps which are unique to amorphous material/glass. These steps allow for a better understanding of the state of matter pertaining to glasses and how they differ from the original crystal counterparts. ⁽²⁷⁾

The first structural change from the crystal to the molten phase is particularly interesting. Melting occurs as the crystal structure loses its rigid and periodic structure. There is a discontinuity between the crystal to liquid phases. The T_m is clearly defined by a sharp change in volume and enthalpy. This is a first-order transition as shown in **Figure 6**. ^(28,29) After melting, cooling below T_m^{first} results in a supercooled liquid. There is a region referred to as the 'Glass Transition Temperature' or T_g , where the liquid "freezes" into the glassy state; it is unique to amorphous material and not to be confused with a melting temperature, T_m . ⁽²⁸⁾

Of course, both T_g and T_m vary depending on the system investigated as well as the size and purity of the material studied. Other factors affecting the T_g are the cross-

linking and steric effects of groups within the system. Furthermore, the mass and distribution of molecular units give rise to a range of glassy transition states, which is why it is recommended to consider a temperature range for T_g . However, it is debated as to whether the T_g is a phase transition or not.

Amorphous materials, like liquids, show absence of the long-range order observed in crystals. They do, however, hold some form of intermediate-range order which is greater than that usually found in liquids. ^(28,30)

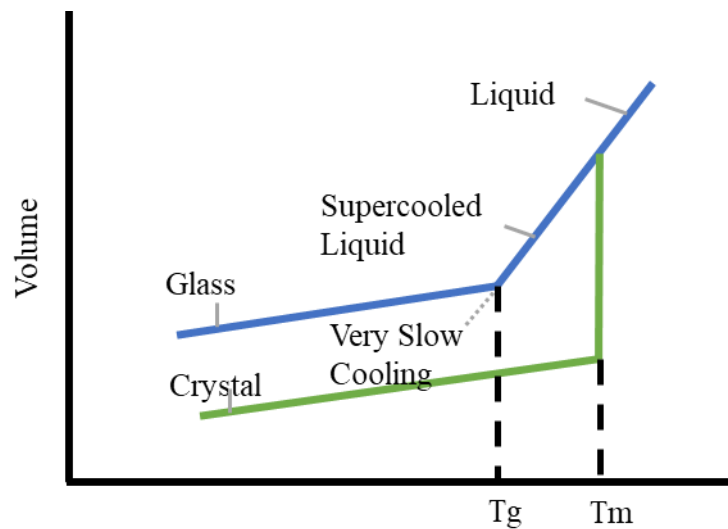


Figure 6 - Graph highlighting the Glass Transition temperature.

To graphically observe how the glassy state differs from its original crystal we can observe the relation of volume against the temperature, **Figure 6**. When the material is undergoing the quenching stage, it is important to prevent recrystallisation. The production process carefully avoids this by a continuous stiffening of the liquid rather than a slow cooling which would cause the product to surpass the glassy phase.

1.3.2 Zachariasen's Rules

Early approaches to the structure of glassy materials thought of them as built up of nanocrystals. However, research carried out by Maes *et al.*, indicated that the measured densities did not correspond with that of nanocrystals. The density of glass material differed by almost 10%. Furthermore, studies carried out using *Small-angle X-Ray Scattering* (SAXS), showed no observable diffraction pattern. ⁽³¹⁾

As a crystallographer, Zachariasen compared both crystals and glasses and found similarities. They both shared a cationic polyhedral structure with very similar elastic moduli and other such mechanical properties. On the other hand, there were many noticeable differences between the two systems. ⁽³²⁾

Crystals are identified through the very structured and ordered assembly of atoms. This ordered structure provides crystals with a comparatively smaller volume (hence a greater density) and lower energy than glasses. Due to this ordered style of packing, crystals have differing properties to those of glass. As noted, crystals exhibit a periodic, long-range order and are usually the thermodynamically stable phase. ^(32,33)

Conversely, glasses do not possess long-range order, which in turn causes a greater volume and a lower density. Moreover, glasses will have higher energies when compared to crystals. The atoms of the same material may be able to rearrange (recrystallise) if more time is given alongside thermal energy. The aperiodic 3D network in glass has no symmetry and is also isotropic, which means the average packing in all three dimensions across the system is the same. ^(32,33)

Zacharaisen established in a 1932 publication, "*The Atomic Arrangement in Glass*", that some of the structural interaction rules for crystals were also valid for glasses as seen in figure 7. His glass formation rules are still applied. The rules are currently associated with the Random Network Theory (RNT). The rules, as shown in **Table 1** highlight the conditions in which a glass can be formed from its corresponding oxides. In order to form a three-dimensional continuous structure, with no long-range order, the oxide must match these rules. Therefore, these rules are not only allied solely with glass, but it provides a description of any network structure. ^(32,34,35.36)

Table 1 -Zachariasen's Rules ^(34–36)

Zachariasen's Rules

- 1) Oxygen atoms in the glass system may not be bonded to more than two cations
- 2) The cations within the system must a coordination of either 3 or 4 (low coordination number)
- 3) For the oxygen Polyhedra, there must be a minimum of 3 corners shared. (To form a 3D Network)
- 4) There must be no faces or edges shared amongst the oxygen polyhedral as this adds restriction within the system and the glass requires a certain degree of freedom

Additional Rules for more complex oxides and corresponding glasses

- 5) Cations must be surrounded with oxygen tetrahedra/triangles at a prominent level.
- 6) The tetrahedra/triangles must only share their corners with each other
- 7) A few oxygens that are connected to two cations within the network, do not link with any other cations

Once a random network is established, there must be some consideration of the effects of the inherent difference between values related to the bonding. Due to their random nature, structures such as glass have a varied bond angle distribution alongside the length and rotational data. In addition to Zachariasen's proposed model,

several other factors help to characterise the glass structure, particularly, regarding the glass network. ⁽³²⁾

1.3.3 Glass Network

The glass network references the structural connectivity within the glass. The Greaves model (1985) describes how each atom plays a different role to form this “network”.⁽³⁷⁾

One key concept is the distinction between bridging and non-bridging bonds. These types of bonds either join, or add breaks between, different groups in a structure. Bridging and non-bridging bonds play a vital role in forming a network through linkage of moieties within the glass. However, they are not the only subgroups to affect the glass network. Moreover, the additional oxide ions introduced by the metal cations and forming the non-bridging oxygen species coordinate to cations and are a considerable influence upon the glass network. Before going into further detail, we must mention the concept of intermediate-range order.^(37,38)

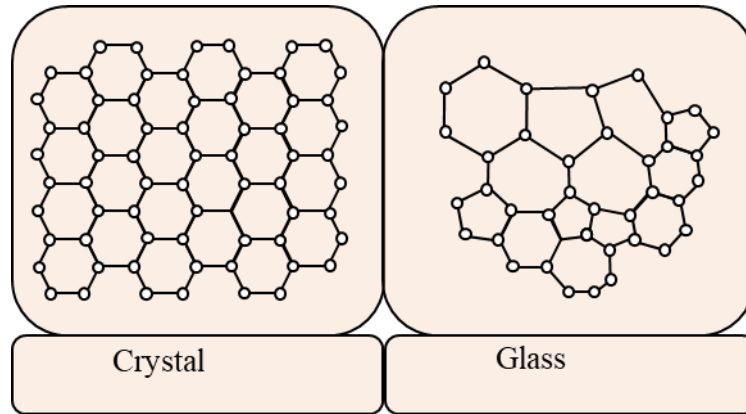


Figure 7 - Crystal vs Glass networks showing the more defined, periodic crystal structure, and the intermediate range order with the glass network.

Most glasses show some definition in the short-range, where the atom and its nearest neighbour have relatively similar distances or order to those in crystals.

In addition to this local order (usually within the range of 0.5-1nm), the intricacy of the network creates the intermediate-range order ^(33,39) as illustrated in **Figure 7**.

A variety of structures have been studied but none as much as the silica crystal. Silica-based glass has become the leading class of material in developing concepts of glass structure. Further discussion of these concepts now follows.

1.3.3.1 Network Former

A network former is a compound that can form a network from the cation it possesses. The structure typically contains mixed ionic and covalent bonds and provides a solid, strong matrix for ions to be added. As mentioned in Section 1.4.2, the main elements that form inorganic glass are silica, boron, and phosphorus. However, there are many other elements that can form glass. ⁽⁴⁰⁾

The p-block elements are usually network formers as they can make strong bonds with oxygen. Moreover, they are elements that have a tendency to form tetrahedral coordination with distinct bond lengths. To understand the connectivity the 'Q_n Distribution' is used, which helps to describe the oxygen bonding within the network. Firstly, we must understand the two bonding categories of oxygen as the network structure is very dependent on the role of these oxygens. ^(41,42)

Typically, there is a varying concentration of both nonbridging oxygen (ONB) and bridging oxygen (OB) for every tetrahedron found. The Q_n distribution identifies the amount of OB forming part of the main tetrahedron units by a subscript value identifying the quantity. Therefore, Q₄ represents 4 bridging oxygen atoms bonded to the network forming cation. Q₃ represents 3 OBs and so on. However, this notation does not work for all complexes as seen for some glass such as phosphorus oxide-based structures form chain-like networks as there is a presence of a double bond. ⁽⁴¹⁾

1.3.3.2 Modifiers and Intermediates

Modifiers are cations that affect the glass network in some form. As the name suggests, the addition of modifiers changes the way the atoms are linked together, **Figure 8**. The modifiers break up or weaken the network and form "channel-like" sections; however, the modifiers impart additional characteristics. Examples include oxides such as CaO and MgO. Here, the configuration is now more complex and usually avoids rearrangement during the quench stages of glass production. The difference between network formers and modifiers is that modifiers are unable to create glass structures on their own.

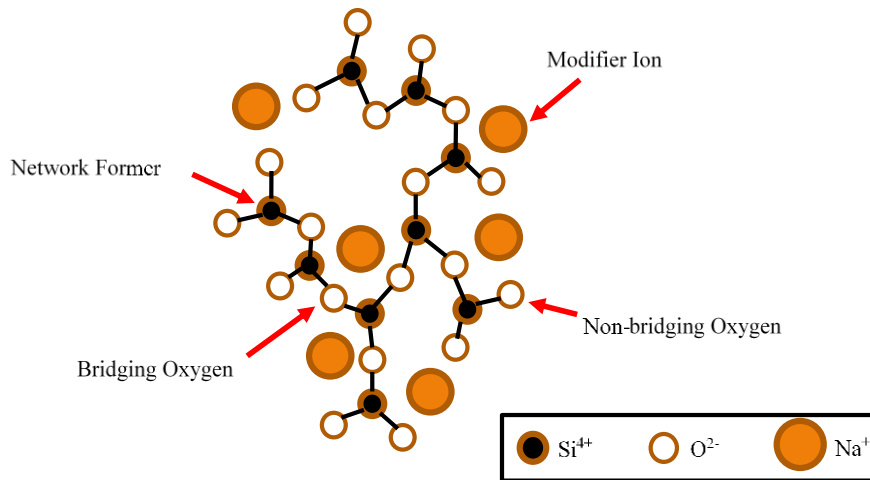


Figure 8 - Image highlighting an example network former Si^{4+} and modifier ion, Na^+ .

It is common to find modifiers to have a small charge but large radius, such as sodium ions, Na^+ . They also generally have large coordination numbers with the oxygen atoms within these oxides. However, this is not always the case; some ions have a small radius and therefore do not necessarily disrupt the glass network as most modifiers do. These ions are known as intermediates. ^(43,44)

Intermediates usually form strong coordination with oxygen. In fact, it is usually found that they have a coordination number of 4 as observed with silica. Examples include aluminium and titanium oxides. These oxides help to avoid any alkali ion additions interrupting the glass network, which is carried out by countering the charges brought by the cations into the system. However, this is not always beneficial. During melt stages, aluminium oxides can increase viscosity which creates difficulty when producing a homogenised system. ⁽⁴⁵⁾

1.3.3.3 Other Constituents

Within most glasses, there are other elements that make up the full structure. These can be defects, impurities, or other minor constituents. Although not a major component compared to the network formers or modifiers and intermediates, these elements can ultimately transform properties. Such alterations to the system include increasing or decreasing the melting temperature which can determine a more economically and commercially viable product. They can also cause other problems within the production course as their reactivity to other materials can be detrimental to the equipment used and can also create unwanted by-products. ^(33,36)

1.4 Types of Glass

There are numerous types of glasses⁽⁴⁶⁾ both synthetic and natural and some of the main typed will now be reviewed.

1.4.1 Natural Glass

Obsidian, **Figure 9**, is an extrusive igneous rock/volcanic glass and the most abundant naturally occurring glass. It is created through the actions of lava eruptions, followed by rapid cooling with minimal crystal formation. Specimens can be found in assorted colours, but they occur more commonly in the black and brown forms. The formation of obsidian glass is very unstable and samples are usually found re-crystalising. This re-crystalising occurs at various rates within the rock itself and can be cut out and separated. These are known as snowflake obsidian/cristobalite crystals. ^(32,46)

Another naturally occurring glass is fulgurites. Their development is through the process of lightning striking and the subsequent melting of sand. Physically, fulgurites are grey in colour, tubular and can be found branching and descending beneath the sand. ⁽⁴⁷⁾



Figure 9 - The naturally formed Obsidian Glass (left) and a polished and cut version of the volcanic material (right). ⁽⁴⁶⁾

However, through various techniques, we can create and form glass from their crystal counterparts through heat and quenching processes.

In the subsequent sections we will consider synthetic glasses.

1.4.2 Inorganic Glass

There are a variety of inorganic glasses which are of great interest commercially, of which there are three main types. Within each of these glasses, there is usually one major component that helps distinguish each glass from one another.

The first and most commonly used glass is silica, SiO_2 ; silica based glasses show great thermal resistance, **Figure 10**, which can cause problems for the production process – with temperatures as high as 2000-5000 K being required - but for use in chemical laboratories or within nuclear waste, high thermal resistance is essential. Silica is also exploited extensively to make optimal lenses. SiO_2 not only has malleability, but more importantly, has a high refractive index which allows light to pass through easily. ⁽⁴⁸⁾

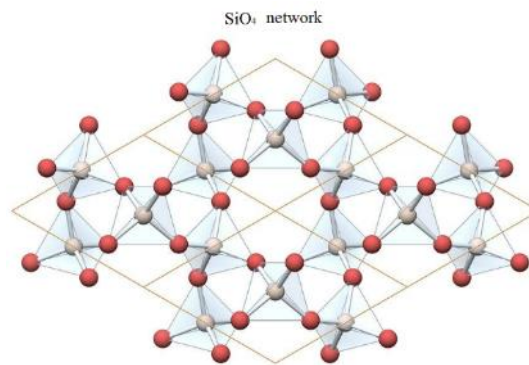


Figure 10 - Image to show Pure Silica Network. Red spheres are oxygen atoms, whilst the grey atoms represent the silicon with the surrounding blue polyhedra. ⁽⁴⁹⁾

Next is boron oxide, B_2O_3 , which will be discussed in greater detail in **Chapter 4**. In common with SiO_2 , these oxides form glasses with a low thermal expansion coefficient (between $30 - 60 \times 10^{-7} \text{ }^\circ\text{C}^{-1}$), which is beneficial for glass. Moreover, the chemical durability properties increase, which helps avoid a chemical attack. Consequently, this property is used by industries such as the cooking, automobile, and bio/chemical laboratories. However, the disadvantage to its production is that they require elevated temperatures to form the glassy material and hence entail high costs. ^(49,50)

The third large inorganic glass member is the Phosphorus oxide, P_2O_5 . Phosphorus-based glasses are primarily used in optics and are widely used as a replacement for

silicate glass. These types of inorganic glass have great resistance to hydrofluoric acid and are also particularly used for radioactive waste. However, it is properties such as glass water solubility and biocompatibility which deems it suitable for use within the human body. There is currently very extensive interest in bio-glasses with phosphorus-based glass being at the forefront, in particular, for cases involving bone scaffold and biodegradable tissue. ^(51–55)

Each of the mentioned oxides above are network formers which will be detailed later and are the three largest and most fundamental inorganic glasses available. For the purpose of this project, B₂O₃ based glasses will be observed and analysed from crystalline structures to the glassy phase.

1.5 Glass Application

The variety of applications of glassy materials is due to the unique chemical and physical properties that these materials possess. Modern glass has applications across a variety of fields due to properties mentioned throughout this chapter. Some of the industries that utilise these unique set of characteristics will also be outlined within this section.

Unsurprisingly, glass has become an essential material through technological advances and has thousands of applications. In science, we have used glass as a key container for reactions but also apparatus for various functions. These functions include measuring, preparation, and storage of chemicals. It is almost impossible to enter a laboratory without finding glass equipment. This is understandable as the

chemical reactions carried out require a safe and stable environment, particularly when elevated temperatures are being utilised. In fact, in both *biological and chemical laboratories*, borosilicate glasses are used the majority of the time. Once known as the “Chemically Inert Glassware”, borosilicate-based apparatus helped biologists with the study of DNA/RNA and recombinant protein through the use of glass bead milling. As the equipment operated with borosilicate-based glass, it allowed for safer and more user-friendly use as the glass requires extremely high temperatures before shattering.

(56)

Areas in which glass is essential and profitable include the *construction, architectural and motor industries*. Windows are created from glass for use within buildings, but it is also used for vehicles and other physical structures. The requirements of clients and therefore products differ vastly. It is important to be able to work with a material that can be modified cost-effectively, and without increased time consumption. To study heat transfer in windows and effects of atmospheric carbon dioxide levels, an investigation carried out by Quynh *et al.* observed the thermal resistance of niobium-doped tin oxide glass film. The study observed the Infrared transmittance, and comparisons were drawn again with Corning glass. The results indicated that the transmittance decreased as the levels of dopant is increased. (57)

More in-depth use of glasses' chemical durability is the *containment of waste substances such as radioactive, mixed toxic waste, asbestos, electronic and waste from clinical environments*, **Figure 11**. Borosilicate glasses are used and deposited within deep geological repositories. The flexibility of the material provides for both high and low level of chemical waste, which makes this an ideal depository vessel as it can then

be incorporated with the waste and placed underground. It must, therefore, be predicted to be safe for thousands of years. This is one of the reasons why analysis of the glasses has headed towards the computational route, as it is safer, less expensive, and more tractable than physical experimentation. More importantly, adequate predictions can be made, and also further improvements to the borosilicate glass can help to reduce the possibility of chemical leakage. ^(58,59)

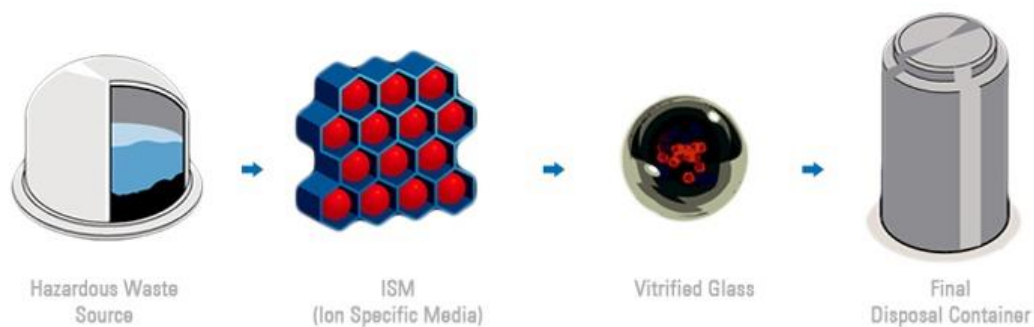


Figure 11 - An industrial example of nuclear waste containment using Glass. ⁽⁶⁰⁾

When managing prominent levels of radioactive (RA) and non-radioactive material, it is important to immobilise them. The choice of the container depends on features including flexibility and integrity. Glass has been considered by scientists across the globe due to many factors:

- I. Glass structures can accommodate many kinds of radionuclides within RA nuclear waste. ⁽⁶¹⁾
- II. Glass possesses a good processing ability. To vitrify RA material, glass networks can be changed. This must occur under volatile and unpredictable conditions that are tolerated by the glass. ⁽⁶¹⁾

- III. A key factor includes chemical and corrosion resistance. When dealing with such material, conditions are very variable and hence the selection of container is vital. ⁽⁶¹⁾

In the vitrification of nuclear waste, the waste material can be easily combined into the glass mixture. The areas of improvement come from searching for the most durable glass and, due to the unwieldy nature of the RA waste, computational research plays a vital role. The use of borosilicate glass for immobilisation of high-level nuclear waste (HLW) has occurred for more than 50 years within Europe, Japan, and the USA. There are two methods in which nuclear waste is removed. Firstly, the glassy material can be incorporated into the HLW and taken to repository sites which encloses the nuclear waste safely. The second method involves encapsulation, enclosing material to avoid reaction with external factors. ⁽⁵⁹⁻⁶¹⁾

1.6 Research Area

1.6.1 Borosilicate Glass

As we have seen, there are a variety of different types of glasses, with remarkable progress from soda-lime to borosilicates which are now at the forefront of applications. These borosilicates are important to study as they are being developed at an expanding rate in the industry, yet structurally there are still several unanswered questions which can help further improve quality and properties.

Borosilicate glass, which is one of the most commonly utilised glasses in the world, comprises two of the major glass formers, SiO_2 and B_2O_3 .

SiO_2 is the major component in borosilicate glass, and it accounts for approximately 70-80% of the total structure, **Figure 12**. The rest of the glass is usually built up of a particular type of boric oxide, B_2O_3 , (5-20% of most borosilicates) which provides interesting structural connectivity. **Figure 12** outlines a general schematic of the typical borosilicate glass. What distinguishes the different types of glasses is not only the variation in concentrations of these two major components, but also a small number of alkali atoms and compounds which are usually added to highlight certain properties such as higher refractive index: examples include sodium, potassium, or aluminium oxide. ⁽⁶²⁻⁶⁴⁾

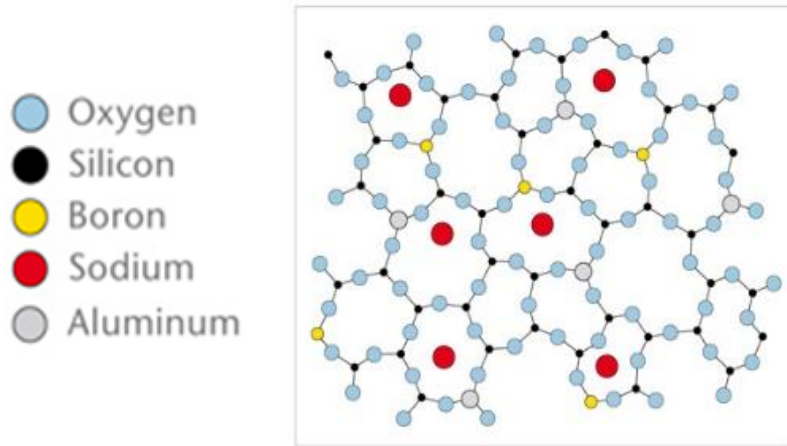


Figure 12 - A typical Borosilicate glass structure adapted from Boltres *et al.* ⁽⁶⁵⁾

Although silica is a vital compound, it is the bridging and non-bridging oxygen atoms found in B_2O_3 that are assumed to alter the glass structure and properties. It has been found that for harder and more durable glass, a higher proportion of bridging oxygen atoms is needed. However, creating a more robust glass engenders greater heat resistive properties and although this is a valuable characteristic, it leads to extreme temperature requirements for melting the crystalline form. ^(62–65)

Molecular Dynamics (MD) simulations - a computational technique explained further in Chapter 2 - allows for safe and time-effective analysis of the microstructure of borosilicate glass systems.

There have been several previous computational studies of borosilicate glasses. Kilymis *et al.* using MD techniques demonstrated that as the boron coordination number decreased with an increase in the non-bridging oxygens, the hardness of the glassy material decreased. This is because the system attained greater entropy and is thereby more disordered, which added greater system fluidity. ^(67,68)

Borosilicate glasses have also been studied computationally by replacing the sodium ions with caesium for nuclear waste containment. Not only did the results of the research show a decrease in the boron-oxygen bond distance but also an increase in the oxygen-boron-oxygen angle. It was also observed that glass density increased. ⁽⁶⁹⁾

The problem of density variation with temperature has also been addressed for silica glass, which has very interesting anomalous features, one of which is its unusually high maximum density at around 1900 K. MD research, carried out by Takada *et al.*, has indicated a density maximum of 2400 K, an improvement from the previous MD calculations, which gave the maximum above 4500 K. However, this is still far off the 1900 K experimental average. Interestingly, the calculations show an increase in the density due to the rearrangement in the rings between the Si-O bonds. ^(70,71)

New methods have been implemented, by the Takada research group to understand internal interactions within glassy material. ⁽⁷²⁾

An important aspect of the behaviour of glassy materials is their *resistance to thermal shock*, which is an abrupt fluctuation in temperature causing stress in a material due to the varying expansion at different points. This eventually leads to breakages and is usually identified for brittle material such as glass and ceramics, which is a key concern for glass and ceramic production. Furthermore, as many borosilicate glasses are used in laboratory apparatus, they experience extreme temperatures and hence are required to be resilient to these temperature changes. To study the thermal-mechanical properties, Infrared and Raman Spectroscopy are commonly used

techniques to help investigate the thermal history and its relation to the glass composition. ⁽⁷³⁾

Research carried out by Shao *et al.* examined the preparation of glass with a diverse range of coatings to investigate how resistant the glasses were to thermal shock alongside levels of emissivity radiation, which is the ratio of the surface thermal radiation compared to the radiation from what is known as an ideal black surface. The technique involved used thermal cycling from room temperature to 1673K, 15 times. The researched showed that when the glass was M40-coated (40% mass per cent of MoSi₂) the weight loss was only 2.84% without any cracking even at a micro-level. In comparison to 11.32 and 8.62% for the M60 and M80 coatings (60 and 80% mass per cent of MoSi₂ respectively), which showed that integrative insulation can help create glass with a great thermal resistant property. ⁽⁷³⁾

Doping B₂O₃ glass is quite common, an example of which is with P₂O₅ which can lead to a negative expansion rate within the lower ranges of temperature (from 100°C to 300°C). ⁽⁷⁴⁾ Another example of exploring thermal shock properties of glass was carried out on barium phosphate glass with B₂O₃ addition. Takebe *et al.* observed that with the inclusion of B₂O₃, we can see a huge improvement in the physical strength of these types of glasses due to the decrease in the thermal expansion coefficient. The addition allowed for crosslinking between phosphate and diborate groups. The newly formed PO₄-BO₄ groups increase the glass transition temperature. ⁽⁷⁵⁾

The thermal shock properties are utilised for laboratory glassware. During standard laboratory experiments, the flask and the glass containers used require not only

thermal shock properties but also chemical resistivity. This property allows for withstanding the chemical and/or solvent reactivity. ^(18,74)

The thermal expansion properties resulted in the use of borosilicate glass within the medical field. Investigations have created and improved dental core ceramics. Veneers were coated with Si_3N_4 specimens to create a glossy and smooth finish to replicate human teeth. The process of creating these teeth involves a mixture of pressure and temperature changes. Hence it is vital for the material to be able to withstand these fluxes. Borosilicate glass has a low thermal expansion, which means that at high temperatures the structural response to the temperature remains minimal and therefore eases the production of dental and medical material. ⁽⁵³⁾

Borosilicate glasses have also been considered for creating lighting and optical equipment. One of the benefits is that with the addition of alkali metals, these glasses have the ability to resist any decolouration after being exposed to gamma radiation. When the network structure has high levels of NBOs (Non-Bridging Oxygens), the network becomes weaker which decreases the density, which in turn, has a major effect on the density of the material. ^(33,77,78)

The ability for borosilicate glass to withstand elevated temperatures allows use within pipe-coolants, **Figure 13**.

Throughout the mid-twentieth century, a variety of electronic equipment used borosilicate-based glasses. With advances in manufacturing processes, the tubular form of the glass permits an even more flexible use within the industry. ⁽⁸⁰⁾



Figure 13 - Glass being used within Pipe coolant systems in a motor vehicle. ⁽⁸⁰⁾

Borosilicate glasses are often utilised alongside a silicon wafer (thinly sliced material used in circuits and solar cells), which gives an increase in semiconducting ability. The electronics industry frequently uses this material as it results in a high-quality product with high mechanical strength which also helps combat issues of unintentional bonding by silicon to the rest of the structure. ^(81,82)

Arguably one of the biggest and ever-developing areas of glass use is within the electronics industry for large, flat panel displays and screens. As technology progresses, the requirements of materials for products also change correspondingly. Mobile phones, TV screens and advertisement displays are just a few areas in which thinner and transparent glasses are required, **Figure 14.** ⁽⁸³⁾

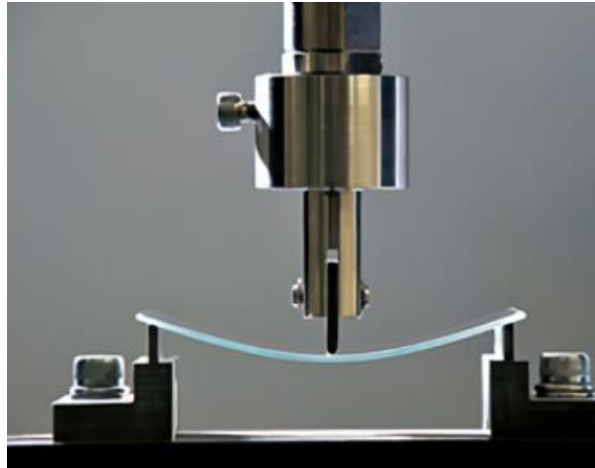


Figure 14 - Image showing stress testing of chemically strengthened glass to be used for screens in phones, tablets, and other electronic devices ⁽⁸³⁾

Several experimental structural studies of the binary and ternary structure of glassy material have been reported utilising Powder Diffraction (PD) methods. It is common to see that the XRD patterns exhibit no continuous or discrete peaks; they also have no long-range atomic arrangement. They do possess a broad peak around 25-30° usually due to Oxygen and Oxygen interactions, which is very common for amorphous materials.^(84,85)

1.6.1.1 Boron Trioxide Structure

A component in borosilicate glass is B_2O_3 , one of the three oxides of boron. B_2O_3 is primarily found in two forms: the first being a crystalline, hygroscopic, white solid, and the second being more commonly found is an amorphous, vitreous form. B_2O_3 possesses many challenges when attempting to crystallise it. In fact, it is commonly considered one of the hardest known compounds to crystallise. ^(86,87)

The structure of glassy B_2O_3 is widely debated. The fundamental building block has been recognised as a BO_3 group: a trigonal planar molecule which is then connected to repeat units to create the full structure. The links between these BO_3 groups is not fully understood, however, several models have been proposed. Included is the theory that a random network is created by these BO_3 triangles which are continuous and bear no regular format. A widely accepted model is that glassy boron trioxide (g- B_2O_3) is constructed of boroxol rings, 6-membered rings with alternating B and O atoms (**Figure 15**). The B-O bond is partially covalent but interestingly, the bond allows for the coordination of boron to change depending on the environment it is in. It is known that that B can coordinate to both 3 and 4 O atoms. The existence of boroxol rings helps to preserve the liquid-like density, and also maintain a low-energy structure.⁽⁸⁹⁾

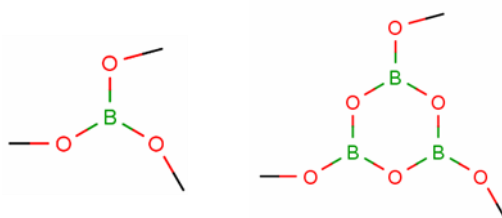


Figure 15 - BO_3 building block (left) and the boroxol ring (right) thought to identify the structure of g- B_2O_3 .

In borates, these boroxol rings are very important as they can lead to the introduction of further larger rings and hence the density of these structures is dramatically changed. **Figure 16** illustrates four arrangements having the same topology, whose densities, however, all differ. It is noted that if the boroxol ring is replaced with the

BO_3 elementary groups, the density is reduced by $\frac{3}{8}$ of its original value in a 3D configuration. ⁽⁹⁰⁾

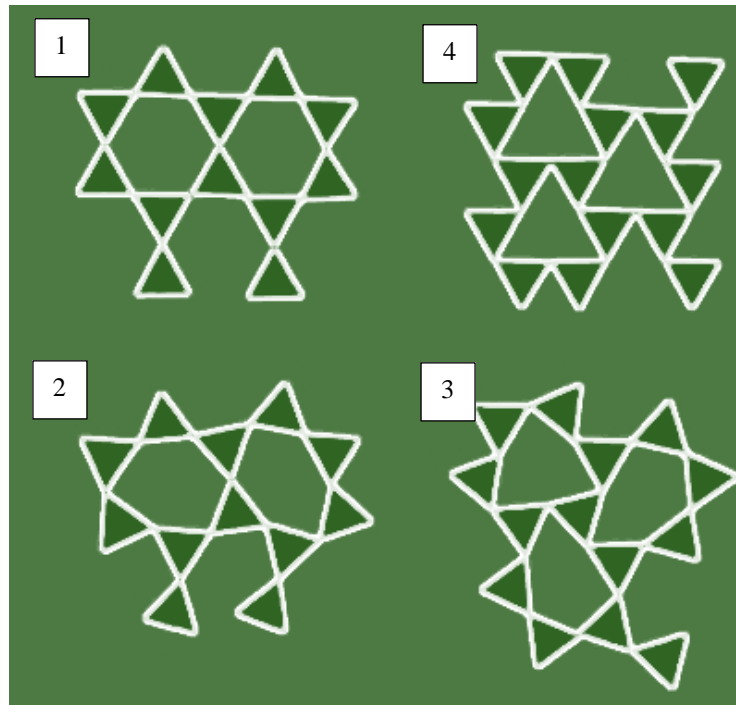


Figure 16 - 4 different configurations of B_2O_3 units which maintain the same topology. Density is reduced by a $\frac{1}{4}$ from structure 1 to 4. Adapted from Pye et al. ⁽⁸⁸⁾

Raman studies have been used to classify the boroxol rings. ⁽⁹¹⁾ However, the biggest obstacle in understanding the structure of the material based on ring model is in identifying the proportions or fractions (f), of these rings within the structure. Evidence has been contradictory as low f values (0—30%) and high f values (60-85%) have both been suggested. The Raman data reveals a peak at $\sim 800\text{cm}^{-1}$, which is thought to correspond with the oxygen movement in the boroxol rings. However, f values still remain unclear due to the unknown Raman intensity modulations. ⁽⁹¹⁾

Nuclear Magnetic Resonance (NMR) is currently used to determine a reliable f value which is the fraction of borons in boroxol rings. ⁽⁹¹⁾

MD simulations have also been employed and suggest the structure to be boroxol-poor (BP), which does not correspond well with experimental data. It was found that it is necessary for a polarised potential or 3-body interactions, to be used to form boroxol rings. The polarised potential offers a realistic set of particle interactions, and also provides chemical flexibility. This, in turn, will allow for the representation of B_2O_3 glass behaviour in terms of formation and relaxation *via* computer simulations. Umari *et al.* were the first to carry out full *ab initio* MD simulations of the boron oxide. They were able to determine a value of f to be $\sim 75\%$ in alignment with Raman and ^{11}B NMR data. ⁽⁹¹⁾

The studies of borosilicate glass have in general seen MD simulations primarily give lower f values in comparison to experimental data. The reason behind this has been debated. One rationale may be due to the fast-quenching rates used. Computer simulations investigate these rates to the accuracy of about 10^{11} K/s (with a time step set to 1 picosecond and temperature at $10^\circ C$). However, this is comparatively very high to actual experimental figures which approximate around 100 K/s.⁽⁷⁷⁾

Another issue with modelling B_2O_3 is the complexity of the B-O bond which is also key in the slow development of the glass network. Combinations of MD and Monte Carlo (MC) techniques have been exploited. The use of MC-like methods is due to the fact that one can help create random structures which vary in the B-O ring sizes. It then helps to select the most stable structure. MD is incorporated such that a structure can be relaxed. To this end, a method has been developed named 'Computer Synthesis' which can be employed to observe real crystal structures being modified to create

new ones. It has been seen to have reproduced the high f values and glass density as observed in experimental research. ^(78,92)

However, the computer synthesis method is problematic as these structures are pseudo-crystals. This is because the intermediate and long-range orders do not have the natural “random” amorphous conformation. These attempts have been made from these pseudo-crystal structures which were attained from actual high-pressure polymorphs, B_2O_3 -I crystals. These structures however only had ~50% f values of boron atoms in the boroxol rings. **Figure 17** shows an outline of the first steps involved in creating these structures. The MC method, although very simplistic, varies the size of the boroxol rings. ⁽⁷¹⁾

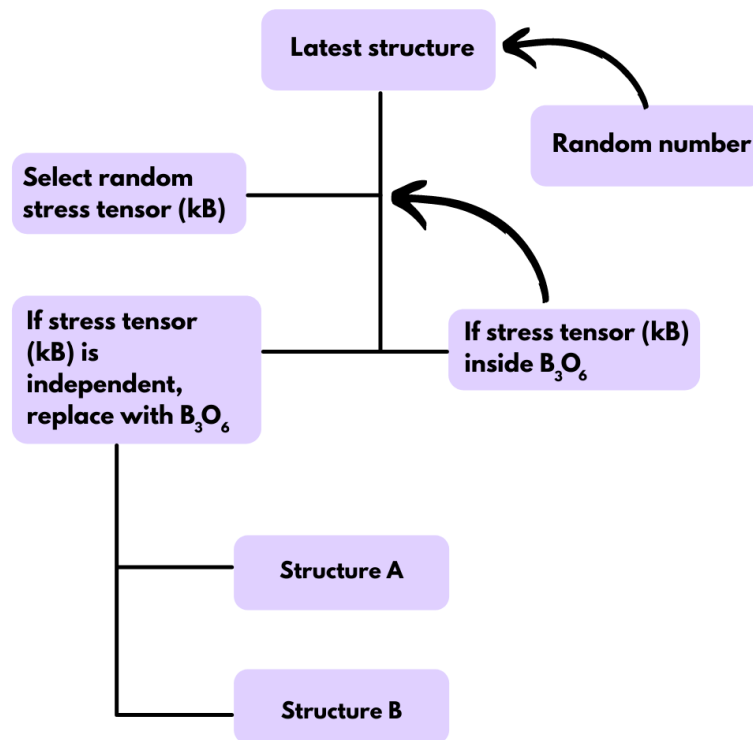


Figure 17 - Schematic of the MC steps for creating pseudo-crystal structures from B_2O_3 -I crystals.

The two structures, a, and b in **Figure 17**, then have their B-O bond lengths constrained in the MD step, which is in order to avoid any possible bond breakages in the heating steps. The systems are heated up to 500 K for 1 ps. In the next step, the constraints are removed, and the structures are then annealed to 0.1 K very slowly over the same period of time. Analysis is then performed on the lattice energies of both structures and is subsequently compared. It must be noted that the energy barrier between the two structures is neglected, and also the use of constraints would discount some of the entropy effects of the system. ⁽⁷¹⁾

1.6.1.2 Borate Systems

In comparison to borosilicate, borate glasses have a higher concentration of alkali ions. As we have noted, boron is a network former that tends to bond in a triangular 3 coordinated fashion with oxygen, although tetrahedral coordination is also formed (**Figure 18**). Where this type of glass differs from the high silica glasses, is that when further alkali ions are added they tend to give an opposite effect; the thermal expansion properties decrease but borate glasses can also exhibit an increase in viscosity, which is known as the ‘boron oxide anomaly’.⁽⁹⁴⁾

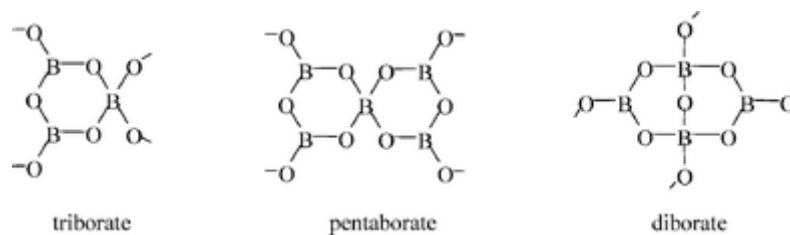


Figure 18 - Borate Glasses displaying typical ring structures.⁽⁹⁵⁾

These types of glasses have been under investigation to understand specific properties by doping with heavy metal ions. Current research sees lead being used to create glasses that are doubly doped. One such study compared these lead doped glasses and glasses co-doped with lanthanide ions. The results indicated that the energy transfer in these glass systems was a non-radiative process.⁽⁹⁶⁾ Materials such as barium borate glasses have also been investigated while doped with vanadium at varying concentrations. UV/Vis methods were used to identify the effects on the optical energy gap which allows for the identification of heat dissipation rates.⁽⁹⁷⁾

For common electronic devices, borate glass has gained interest due to its ionic conductivity. Researchers are looking at the possibility not only to use the glass as an electrode but also as the electrolyte, due to its good ionic conductivity. One such example is silver borate glasses which are able to be utilised as solid electrodes, owing to its high ion conductivity properties. ^(70,98–100)

The interest in borate glasses and crystals has pushed research to employ computational approaches as these can serve as guides for experimental and industrial uses. Some glasses used in nuclear waste encapsulation exhibit some irradiation after exposure, therefore borate glasses - in their irradiated and pure form - were observed to study the hardness of the material. The aim was to compare both experimental data with predictions from the MD experiments. The “pure” form was observed to have a disordered structure that contained more 3- and 4- membered rings in comparison to excessive multi-carbon rings. Kilymis *et al.* also witnessed that after some nanoindentation, the structure seemed to undergo a conformational change where smaller rings became more prevalent than larger ones. ⁽⁶⁹⁾

1.6.1.3 Previous Structural Research

As mentioned, the structure of B_2O_3 poses many challenges. Understanding the structure is therefore one of the key aims of this project.

Naturally, B_2O_3 systems are found with a coating of oxide which is dependent on variables including the temperature and the humidity. This forms boric acid and there has been much computational and spectroscopic research. Boric acid, $B(OH)_3$ has also

been extensively utilised as a catalyst, for example in the decomposition of N-nitrosohydroxylamine-N-sulfonate anions. The use in this way, comes from the fact that boric acid is highly efficient and reusable, hence used in further developments in green organic chemistry. ^(99,100)

The molecular and crystal structure of boric acid has already been identified. The oxygen atoms around the Boron are seen to form a trigonal planar geometry. The bonding has also been identified through spectroscopic data, revealing that the O-O distances showed the greatest distances which were above 2.35 Å. ⁽¹⁰¹⁾ As seen in **Figure 19**, the alignment in boric acid is controlled by hydrogen bonding

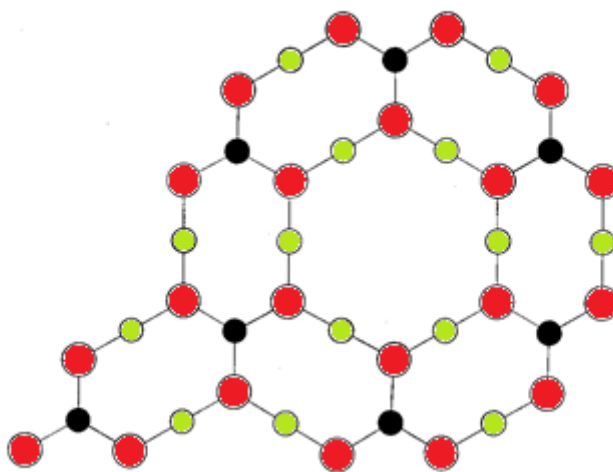


Figure 19 - Black circles are Boron, Green circles are hydrogen and Red are Oxygen atoms. *Adapted from The Crystal Lattice of Boric Acid, BO_3H_3* ⁽¹⁰¹⁾

They connect the BO_3 subunits so as to form a hexagonal arrangement between groups. The hydrogen bonding in these types of systems imposes a uniform hexagonal

structure. Yet without hydrogen, there still appears to be a tendency to form hexagonal units.

The planar structure of these molecules forms layers which are separated by a distance of 3.18 Å, held together by van der Waals forces. Raman spectroscopic data suggest that the hydrogen bonds are placed in an unsymmetrical, disordered distribution and these bonds averaged at 1.03 Å. ⁽¹⁰²⁾

There are several investigations of doped and analogous systems; for example, graphite-like structures can be generated where carbon atoms are replaced with nitrogen and boron alternating. This can be seen in **Figure 20**, which shows the formation of layers as seen with graphite. ⁽¹⁰³⁾

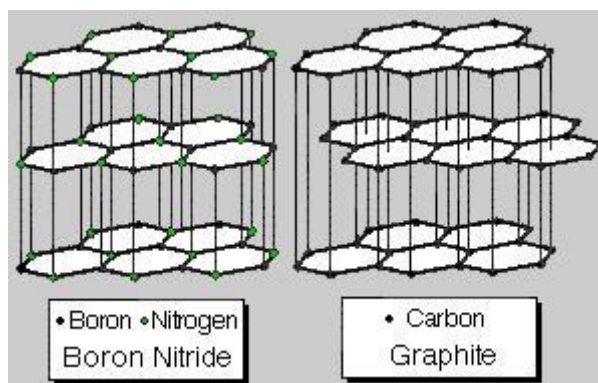


Figure 20 - Image showing the similarities of layering between Graphite and Boron Nitride ⁽¹⁰⁴⁾

Boron trioxide crystal and glass structures remain controversial due to the difficulty of determining the dihedral angles around the coupled polyhedra. ⁽¹⁰⁵⁾ It is also intriguing to understand what the effects of doping into the system are. In this research, we will explore the effects of certain alkali metal ions in the borosilicate systems.

1.6.1.4 Specific Project Objectives

Most applications of glass within a variety of fields including medical, architecture and technology utilise the borosilicate glass type. As previously mentioned, the substructures within these glass networks remain unconfirmed by previous research. B_2O_3 is complex in the structural arrangement and is thought involve BO_3 , BO_4 and boroxol ring substructures. The importance of the boroxol rings is, however, still undetermined and debated.

The purpose of the first section of this thesis was to investigate, *via* the use of MD simulations, the structural transition from B_2O_3 crystals to its molten state and then to the amorphous glassy phase. This was carried out to understand structural relationships within the pure B_2O_3 at each of these stages. The work involved selecting and comparing force fields to understand which more accurately depicts and describes B_2O_3 . The work also involved an expansion of simulation system sizes, which previously had been limited to smaller cells. The frequency of certain groups was recorded and thus further expanding our understanding of these systems.

Study of related crystalline materials also gives valuable insight. Through DFT simulations, a variety of sodium oxide and caesium oxide borates were investigated, in order to examine what influence these metal oxide additions have on the B_2O_3 network.

1.6.1.5 Thesis Layout

Within this research, two methodologies were used. The calculated simulations are separated into two sections. Firstly, we examine the structure of pure B_2O_3 through molecular dynamic (MD) methods. The MD methods are explained and investigated in chapters 2 to 5, whilst the second half (chapters 6 – 8) investigates alkali borates using density functional theory (DFT).

PART I

The following chapters contain the methodology, results and discussions concerning the MD simulations of B_2O_3 within the scope of this project.

2 METHODOLOGY: MOLECULAR DYNAMICS

Molecular dynamics (MD) methods simulate the evolution of a molecular system over a period of time, by solving Newtonian equations of motion numerically. Such simulations enable thermodynamic and other bulk properties of systems to be related to the microscopic movement of atoms. Condensed systems, either crystalline or amorphous can usually be simulated by implementing appropriate periodic boundary conditions.

The dynamic behaviour of a system can change significantly with varying temperature, and, by analysing MD results from different temperature, important information about structure and chemical bonding can be gained and related to experimental observations.

Computational simulations can thus give insight into atomic-scale processes and serve as a guide and predictive tool for experimental research. MD simulations are utilised in biology, engineering, chemistry and beyond. ^(106, 107)

2.1 Equations of Motion

Firstly, it must be noted that in classical MD simulation, quantum effects are not accounted for. Classical MD studies the physical movement of atoms but does not take

into account any time-dependent changes in electron distribution. The atoms interact with each other via the operation of classical potentials, with the output of the simulation being the trajectory which describes the evolution of the atomic position. The trajectories are determined by solving the Newtonian Laws of motion, **equation 1** and **equation 2**, particularly the second law which links the force (F) to the potential energy and velocity.

$$\mathbf{F} = -\nabla V(\mathbf{r}) \quad (1)$$

$$m_i \frac{d^2 r_i}{dt^2} = f_i = -\frac{dU(\mathbf{r}^N)}{dr_i} \quad (2)$$

The mass (m_i), force (f_i) and positions (r_i) are denoted in this equation. The potential energy function is given by V in eqn. 1 and by U in eqn 2. with t being time. From these laws, the force exerted on the atom is given by the negative gradient of the potential. The calculated forces are hence found as a derivative of the energy, calculated from the force field potentials. The values of the force vectors are important as they determine the magnitude and direction of acceleration of the atoms (Eqn. 3).

$$\vec{F}_i = -\vec{\nabla}_i U(\vec{r}_1, \vec{r}_2, \vec{r}_3 \dots \vec{r}_N) \quad (3)$$

Once the initial coordinates are determined, the equations of motion can be solved, resulting in the position and velocities as a function of time. With each step within an MD simulation, every atom's acceleration is calculated and then moved accordingly. A general MD simulation scheme is outlined in **figure 21**.

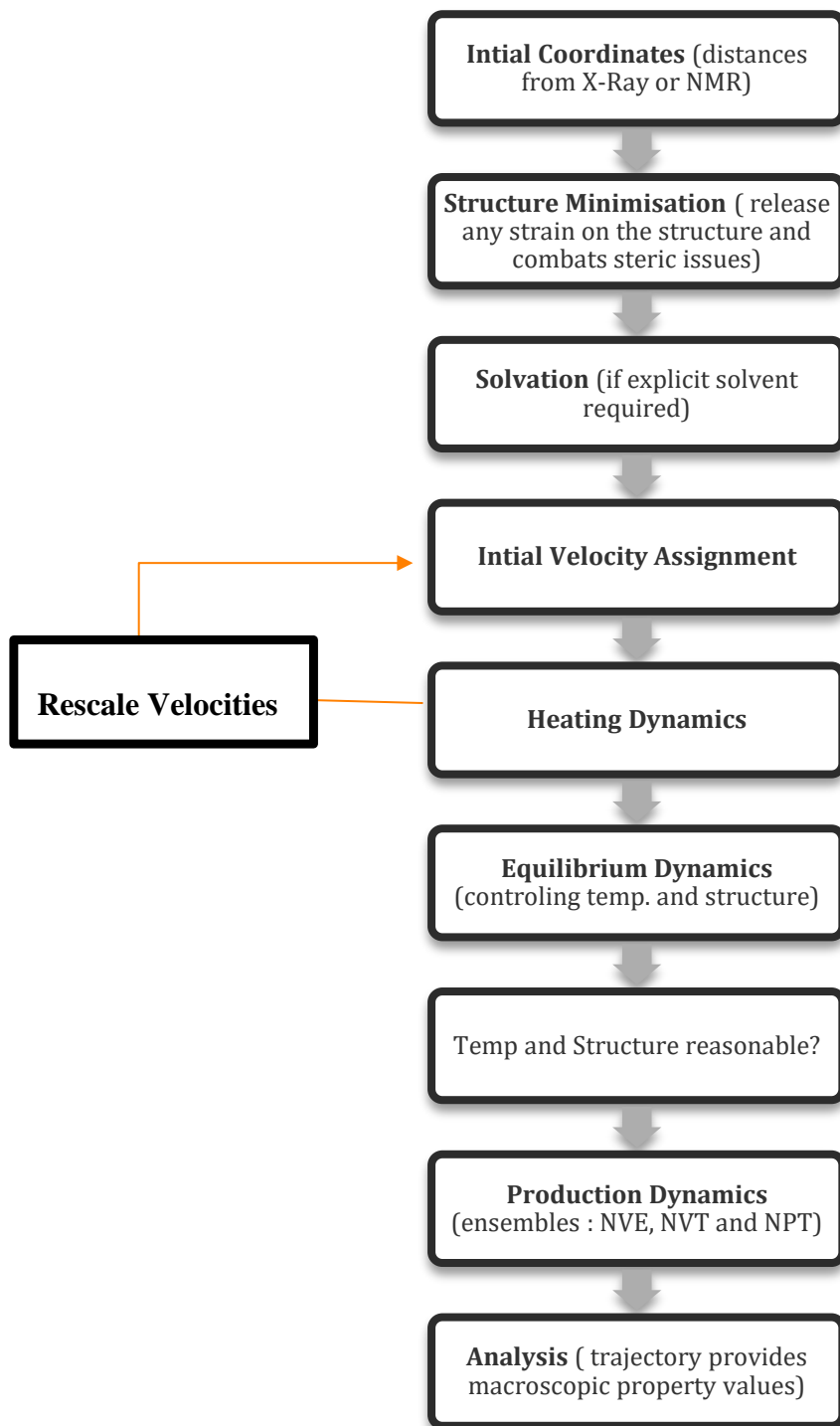


Figure 21 - Schematic showing a generalised MD simulation route.

2.1.1 Finite Difference Methods

For practical purposes, a finite timestep needs to be used in the simulation in order to generate new atomic positions, which can then be used to recalculate the forces and hence velocities of each atom. Finite Difference Methods are hence employed with an appropriate time step in order to achieve realistic simulations. The MD simulations within this thesis used the Velocity Verlet algorithm, which essentially uses two third-order Taylor expansions. The Velocity Verlet algorithm is an easy, accurate and time-reversible algorithm. This algorithm works through a two-step process. Initially, the positions (r), velocity (v), and force (f) are required at a time t . The next stage moves half a time-step by calculating the velocity again from the forces at the original time, to obtain an average velocity over the time step (Eqn. 4).

$$v\left(t + \frac{1}{2}\Delta t\right) = v(t) + \frac{\Delta t f(t)}{2m} \quad (4)$$

where m is the mass of the atom. This velocity is then used to generate the atomic positions at time $(t + \Delta t)$. From the new positions, the forces are recalculated using the interatomic potentials. In the second stage, using these new forces, the next half-step velocities are produced (Eqn. 5).

$$v(t + \Delta t) = v\left(t + \frac{1}{2}\Delta t\right) + \frac{\Delta t f(t+\Delta t)}{2m} \quad (5)$$

2.2 Time Step

It is very important to select the correct time step when undertaking any MD simulations. There is a compromise between selecting a time step that allows for an

adequate search of phase space and one that is not unnecessarily short and computationally expensive. Perhaps the main consideration for the timestep is to have one that is sufficiently shorter than a characteristic time e.g., usually the period of molecular vibration.

2.3 Velocities

As the simulations run, the velocities are calculated at each step. However, an initial velocity must be allocated at the start of the simulations. When using the DL_POLY program (explained further in **section 2.8.1.1**), there is a random assignment of velocities. The programme does this in compliance with a Maxwell-Boltzmann distribution. The equation helps relate the movement of atoms such that the momenta of the atoms collectively is zero. **Equation 6** is used to sum all the atoms' kinetic energy given the temperature of the system T .

$$f_v(v_x) = \sqrt{\frac{m}{2\pi kT}} \exp\left[\frac{-mv_x^2}{2kT}\right] \quad (6)$$

Where x is a specific atom with mass m being considered, with the force f acting on this atom. The Boltzmann constant is represented by k and t is the temperature.

2.4 Periodic Boundary Conditions

Periodic boundary conditions (PBC) are important. To conduct accurate simulations, simply drawing a box of any size to simulate can provide inaccurate results. The system may interact with an image of itself or miss out key network data if the cell size is too small. When an atom exits the simulation box it returns on the other side. Therefore, the edge effects of a finite system and cut-off range must be considered.

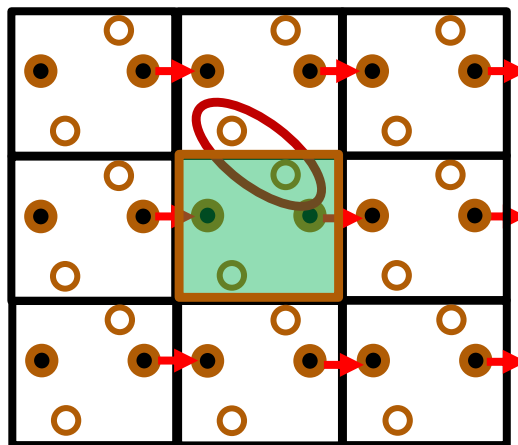


Figure 22 - Image showing effects of periodic boundary conditions.

As shown **Figure 22** selecting the correct short-range cut off in tandem with the boundary conditions. is very important as otherwise a self-interacting error can arise, as shown by the highlighted white molecules. As time progresses, the motion of the black atoms are shown by the arrows, towards the right of the cell. For the white atoms, however, if the motion of these atoms is downwards there will be some unwanted interactions, as two images of the same white atom interact with the same third atom. This is not a correct description of their interactions. The Minimum Image

Convention is utilised to choose an adequate cut off range. This basic rule stipulates that the cut-off is equal or less than half the simulation box length.

When studying systems through simulations, the accuracy of the study is increased as the number of atoms within the system increases. However, selecting this number is a task in itself, as having too many atoms can be computationally expensive.

There were two potentials utilised in the simulations run within this thesis: potentials containing both two and three-body terms. Each of these terms is fully described in the next chapter of this thesis.

2.5 Force Fields/Potentials

The MD simulations carried out in this thesis used interatomic potentials. The choice of interatomic potentials or force field to be used is a critical decision. These force fields provide a description of the bond lengths, angles, and dihedrals and also include parameters defining the van der Waals (vdW) and electrostatic interactions between atoms.

The interactions between atoms look at force fields which looks at bonding but also contains parameters that represent their strength. The bonded interactions can be separated in to bonded (harmonic vibration) and nonbonded pairwise/repulsive interactions but also angular and torsional terms. Most MD atoms are represented as single point masses inside vdW potentials.

$$U(\mathbf{r}) = U_{\text{bonded}}(\mathbf{r}) + U_{\text{non-bonded}}(\mathbf{r}) + U_{\text{other}}(\mathbf{r}) \quad (7)$$

The non-bonded term, $U_{\text{non-bonded}}$, within **Equation 7** can be broken down further to highlight and separate the vdW and the electrostatic interactions. The Lennard Jones (LJ) model describes these vdW interactions which arise from the attractive and repulsive forces between two atoms. The attraction between two atoms originates from the varied strength of the induced dipoles with the range of distances. Conversely, the repulsive forces occur as the electronic clouds overlap.

The repulsive forces are one of many short-range interactions within the system. As electrons come closer together, and the negative electron clouds overlap, there is a repulsion between the atoms in question. The equation below, known as the Buckingham potential, helps clarify this interaction. The expressions, A, B and C are three parameterised constants.

$$E_{ij}(r_{ij}) = A_{ij}e^{-B_{ij}r_{ij}} - \frac{C}{r_{ij}^6} \quad (8)$$

The Lennard Jones is the most widely used potential but not the only term to describe these interactions. Some studies use the Buckingham potential which provides a less “harsh” repulsive term.

The LJ model accounts for the longer ranged attractive forces and the short-range, repulsive forces. The following LJ equation is used in simulations:

$$V(r_{ij}) = 4\epsilon \left[\left(\frac{\sigma}{r_{ij}} \right)^{12} - \left(\frac{\sigma}{r_{ij}} \right)^6 \right] \quad (9)$$

Where V is the intermolecular potential between the molecules i and j . The attractive forces are represented by and the van der Waals radius is represented by. The model suggests that as the two molecules in question increase their separation, V decreases below zero until the equilibrium distance. However, V starts to increase positively after this suggesting an attractive force.

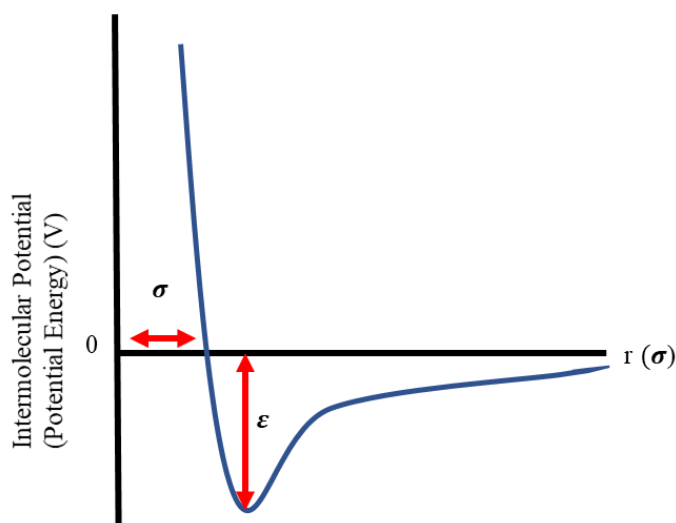


Figure 23 -Lennard Jones Potential depicting the attractive and repulsive forces.⁽¹⁰⁸⁾

This increase to infinity just below zero is representative for a stabilizing force until an external force is exerted onto the system. A schematic of the LJ model is provided in **figure 23.**⁽¹⁰⁸⁾

Electrostatic interactions between atom partial charges are governed by the Coulombic term. Second-order perturbation theory governs these forces. The partial charges for each nucleus in the system and each of their contributions are combined by the coulombic term to achieve the total energy.

$$U_{non-bonded}(r) = \sum_{Atom\ Pairs} \left(\frac{C_{12}}{r^{12}} - \frac{C_6}{r^6} \right) + \sum_{Atom\ Pairs} \frac{q_i q_j}{4\pi\epsilon_0\epsilon_1 r} \quad (10)$$

Once again, r , represents the atomic distance and the energy between the two non-bonded atoms are signified by the constant, $4\pi\epsilon_0$. The dielectric permittivity, ϵ , is a parameter that measures the way in which an electric field acts within a specific material.

2.6 Ensembles

Statistical mechanical ensembles provide a probability of all the microstates accessible to a system. These ensembles include the properties that are kept constant throughout a simulation run. The Microcanonical (NVE) ensemble is the most commonly used as the conservation of the total energy and entropy of the system creates an “ideal” MD simulation. The acronym identifies what is kept constant, in this case, the number of atoms (N), the volume (V) and the energy (E). There are also other ensembles that can be used, such as, the Canonical (NVT) and Isothermal-Isobaric (NPT) with temperature (T) and pressure (P) kept constant in the ensembles respectively. However, these do not represent the usual experimental conditions.⁽¹⁰⁷⁾

2.6.1 Constant Temperature

The connection between temperature and Kinetic energy, V , is given by:

$$V = \frac{3}{2} N k_b T \quad (11)$$

where N represents the number of atoms, k_b is the Boltzmann constant and T is the temperature. From this point, the kinetic energy can be related to the velocity as follows:

$$V = \frac{m}{2} \mathbf{x} v^2 \quad (12)$$

with m being mass and v being velocity. As shown in **equation 11** keeping a constant temperature requires a keeping the squared sum of all the velocities also constant.

2.6.2 Constant Pressure

When the NPT ensemble is selected, the pressure, number of atoms and temperature is kept constant. However, the volume of the cell is still free to change. These changes happen equally in all directions (isotropically). To allow anisotropy, the $N\sigma T$ (isothermic-isobaric) ensemble must be selected.

2.7 Analysis Tools

Throughout this study, there will be a variety of tools being used to identify the chemical and physical characteristics of the structures being investigated. The following section will focus on some analytical techniques used in the MD section of this project.

2.7.1.1 Radial Distribution Function

The Radial Distribution Function (RDF) is denoted by $g(r)$ and is a term that expresses the probability of finding a particular atom in relation to the neighbouring atoms. This measurement allows for recognising whether a system is a solid, liquid or gas due to their structural characteristics. It is known the transition from solid, liquid to gas sees molecules become freer to move around the system. The rigidity, periodic and compact structure of a solid would produce a denser RDF value as there will be less distance between an atom of choice and the surrounding molecules. The peaks on the graph will be sharper and more distinct. As the atom moves to a liquid or a gas, these peaks become broader, and the regular packing is lost, and this plays an influence on the readings of the RDF. Another useful measurement is achieving an idea of the average structure as the atoms are in continuous movement in these states. Experimentally, RDFs are determined through X-ray and neutron diffraction methods and a comparison can be made to computational results.

$$g(r) = n(r)/(\rho 4\pi r^2 \Delta r) \quad (13)$$

Where $g(r)$ is the correlation function and works by representing the relationship between the local density $n(r)$ and bulk density, $(\rho 4\pi r^2 \Delta r)$.

RDFs are calculated considering some fixed distances around an atom of choice **figure 24**. It creates various “shells”. Once a simulation has run, the average number of atoms

in each shell, $n(r)$, is counted along with the shell width, and average density. The equation below outlines the formula.

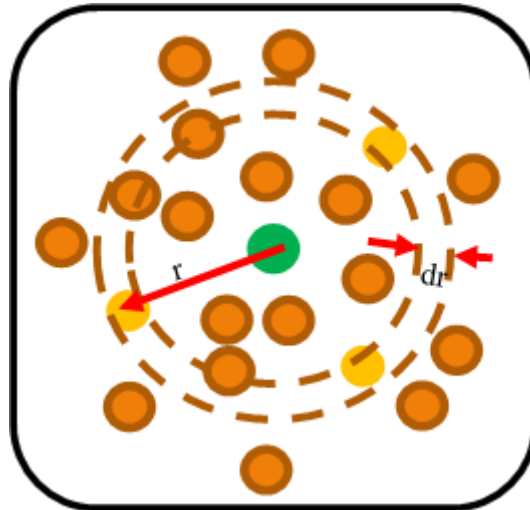


Figure 24 - A visualisation of space separation for the evaluation of the radial distribution function.

The typical RDF will have some indicative features. Firstly, there will be a separation at the start where RDF is zero, which represents the width of the atom. Certainly, the neighbours are unable to be any closer to the other atom within this distance. Following this will be peaks which represent the ordering and packing. In crystalline material, it is witnessed that the peaks are sharp and at long ranges as this indicates the fixed positions and high level of order. Whereas in a molten material or where high temperatures are being observed the motions of the atom create broader peaks.

(109)

2.7.1.2 Mean Squared Displacement

When a system undergoes a temperature change, atoms can be displaced further than their “average positions”. The Mean Squared Displacement (MSD) is a valuable tool to identify the movement of an atom from its average positions but can also identify if the atom is being transported (for biochemical analysis) or even bound and held in specific positions. Some atoms may be prone to diffusing faster than another.

$$MSD_{\alpha}(t) = MSD_{\alpha}(0) + 6D_{\alpha}t \quad (4)$$

Equation 14 identifies the diffusion coefficient with respect to time, D , alongside the MSD intercept, is represented by $MSD_{\alpha}(0)$.

Graphically, as shown in **figure 25**, a straight line indicates diffusion with the gradient or slope identifying the rate at which this occurs, the diffusion coefficient. A curve would imply that there is not a “free” displacement and that the molecule is impacted by collision or other matter. If the rate of diffusion is faster than the linear proportion then it is possible that the molecule is being transported. This is very interesting to analyse and identify how far an atom travels during a fixed period of time and is useful for understanding the effects on the glass network. The Mean Square Displacement (MSD) is a tool that records the deviation of atoms from a reference structure. MSD results in the average distances of individual atoms. ⁽¹¹⁰⁾

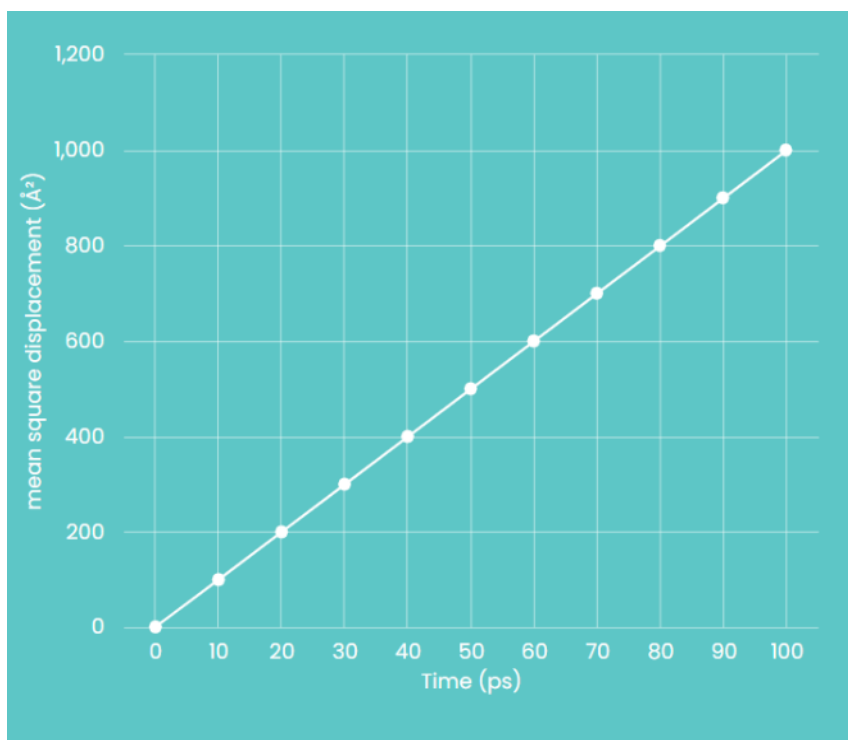


Figure 25 - Typical MSD Plot.

To understand what the graphical data shows, we must consider an atom that is able to travel within a system without interacting with another. If this is the case, the MSD would increase further with t . This is due to the distance travelled being proportional to the time measured, t . In other words, the distance would be equivalent to the velocity multiplied by the time measured. When the system observed is more cluttered, the probability of interaction increases. Hence this quadratic region would be minuscule in comparison to a one atom system. Next, we would see a linear increase in MSD as time goes on. The gradient would depend on the degree of collisions suffered by the specified molecule. The greater the density, the greater the time is taken for an atom to diffuse due to the other atoms being likely to interrupt its diffusion. ^(111,112)

The diffusion coefficient for species i can be calculated directly from the previous equation. The MSD, in summary, is a function of the distance between the initial and final coordinates of an atom. However, to ascertain a greater understanding of the phase changes, the diffusion coefficient considers the vibration at each stage whether solid, liquid or glass. This is given within **equation 15**, where studying a solid will give a zero value to the vibration.

$$D = \frac{1}{6} \lim_{t \rightarrow \infty} \langle (\underline{r}_i(t) - \underline{r}_i(0))^2 \rangle \quad (15)$$

2.8 Computational Programs

For the MD portion of this project, the simulation code DL_POLY was utilised as this was the most suitable code. Both 'classic' and '4.07' versions were utilised testing both NPT and NVT conditions where the classic software supports up to ~30,000 atoms and the latest version of the time of this research, 4.07, allows for bigger structures ^(66,113) See page 84 for condition definition details.

Most visualisations were carried out using two tools. The first program, being the Visualisation Molecular Dynamics (VMD) which allows for analysis of volumetric alongside 3D graphical representations to help observe ring structure and other subunits present within the simulations cells. ⁽¹¹⁴⁾

The second tool utilised for any visualising was the VESTA program. The visualisation software allows for volumetric data to be displayed as well as crystal morphologies. In the context of this research, it has been used extensively to model the polyhedra.⁽¹¹⁵⁾

The following section highlights a benchmarking process in which we used to determine the best version of DL_POLY to use.

2.8.1.1 DL_POLY

To perform the work presented in Chapters 3, 4 and 5 the DL_POLY code was used. This is a software developed by the Daresbury Laboratory and there are two versions tested for suitability for the system in question. DL_POLY uses classic mechanics and is used for simulating the equilibrium, heated and quenched systems for B₂O₃.⁽¹¹³⁾

The systems were tested using both NPT and NVT ensemble to see which can accurately be able to depict the systems, see **section 2.6.1** for further discussion on ensemble choice.

When the NVT ensemble was used throughout the entire simulation run, the simulation failed during the late stages of heating. This is since the pressure was too excessive for the system, the motion of atoms would prefer to expand the size of cell. Hence after the minimisation stage, the NPT ensemble was used.

2.8.1.2 Benchmarking

These MD experiments were performed on DL_POLY on the UCL Legion cluster. To ensure the best version of the software was used, a simple heating simulation was

carried out for benchmarking. The performance of which of the two versions of DL_POLY was suitable for investigation was tested *via* varying the nodes and memory used.

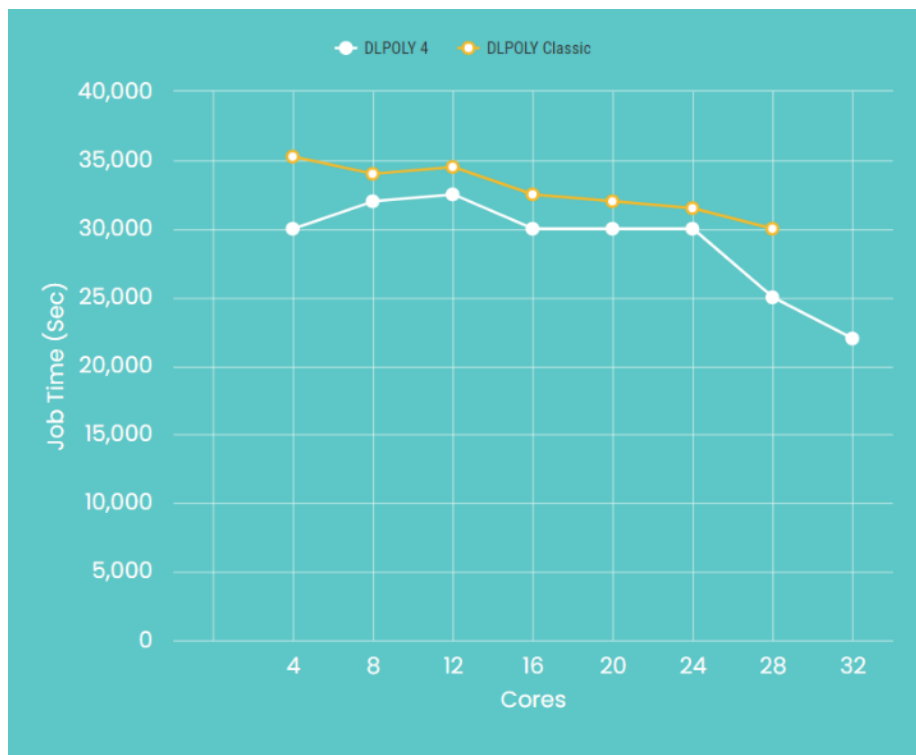


Figure 26 - Benchmarking data for DL_POLY 4 against DL POLY classic.

As we can see from the job time in **Figure 26**, DL_POLY 4 proves to be better on all cores available and was selected for the remainder of this project. We tested both DL_POLY Classic and DL_POLY 4 to observe which allows for the best (through simulation time and core number) simulations. Through this benchmarking process, we can see that DL_POLY 4 with 32 cores seems to have the ability to have the quickest simulation runs and hence was used throughout the MD portion of this research.

3 FORCE FIELD INVESTIGATION

3.1 Abstract

Several investigations have been conducted on borosilicate glasses with various force fields. The complexities arise from the examination of glasses containing varying proportions of network former oxides (SiO_2 , P_2O_5 and of course B_2O_3).⁽⁷¹⁾ In this section, we observed the two and three body potential to simulate the B_2O_3 complex. The simulations in this research are unique in that pure B_2O_3 was investigated as the primary and only network former. Calculated results indicated that an adequate depiction of the glassy phase was possible only with the three body potential utilised in this research. Using varying heating rates, this research shows that a combination of both two and three body potential can reproduce all three phases of pure B_2O_3 : crystalline, molten, and amorphous (glassy) states. The verification of each of the B_2O_3 states was through the structural analysis using RDF calculations which were indicative of the corresponding state of the material researched (sharper, defined peaks for crystalline state, broader for molten state etc). This was also validated by the RMSD value, which showed the effects of using two- and three-body potentials. In the instance of the crystal melting, the difference in mean atomic displacement between the two potentials is 21.83%, with the two-body potential not being able to replicate the amorphous form of B_2O_3 and simulations needing the three body terms for full glass formation.

3.2 Aims and Introduction

Force fields (**Section 2.5**) play a critical role in accurately describing atomic interactions. Forcefields, or interatomic potentials, define the energy with respect to the atomic positions within a system, usually through a mathematical formula. Importantly, the force field must be able to predict and reproduce experimental behaviour. A high quality forcefield is necessary for accurate modelling of atomic mobility.

In the present chapter, two potentials are benchmarked to test their ability to model the formation of a glassy material form of B_2O_3 . In particular, we present a comparison of the two and three-body potentials and the effects of these potentials at each of the stages - from crystal to glass formation of the B_2O_3 structure. A second aim is to identify a suitable potential to generate the bonding geometries correctly. The feasibility of reproducing results for a larger and more complex system will be investigated in **Chapter 5**.

However, it is generally known that the B_2O_3 glassy phase transition, in particular, is difficult to replicate. Indeed values of the density of the glass have not to be replicated in any other simulation work.⁽¹¹⁶⁾

3.3 Computational Details

As explained previously, the process of glass forming involves three main phases: the crystalline, the molten and the amorphous. The transitions between these phases were investigated using both the two and three-body potentials as discussed below.

The experimental lattice parameters for the crystalline phase are noted in Table 2 and are from the X-ray crystallographic data of Takada *et al.* ⁽⁷¹⁾ From these we construct larger supercells for use in our simulations: the first (known as A1 system), contains 480 atoms whilst the expanded system (denoted B1). Is much larger, containing 30,260 atoms. Larger simulation cells allow us to obtain more detailed information and minimise the constraints of periodicity in modelling an aperiodic system, but, of course, at computational cost.

Table 2 - Cell parameter comparison obtained from experimental data and through this computational investigation of both A1 and B1 systems.

Cell Parameter	Experimental	A1 System	B1 System
a, b, c (Å)	8.34	18.20	72.80
Volume, V_o (Å ³)	135.77	6028.9	385853.75

We will consider how simulation size affects the ability to model glassy boron trioxide, but the first aim of this chapter is to compare and investigate the different behaviour obtained using two and three-body potentials basing our models on the earlier work of Takada *et al.* ⁽⁷¹⁾

To test the potentials, we performed a series of calculations using the B1 system which underwent a series of simulations, all under the same conditions. Each simulation run utilised the NPT ensemble, discussed in **Chapter 2**.

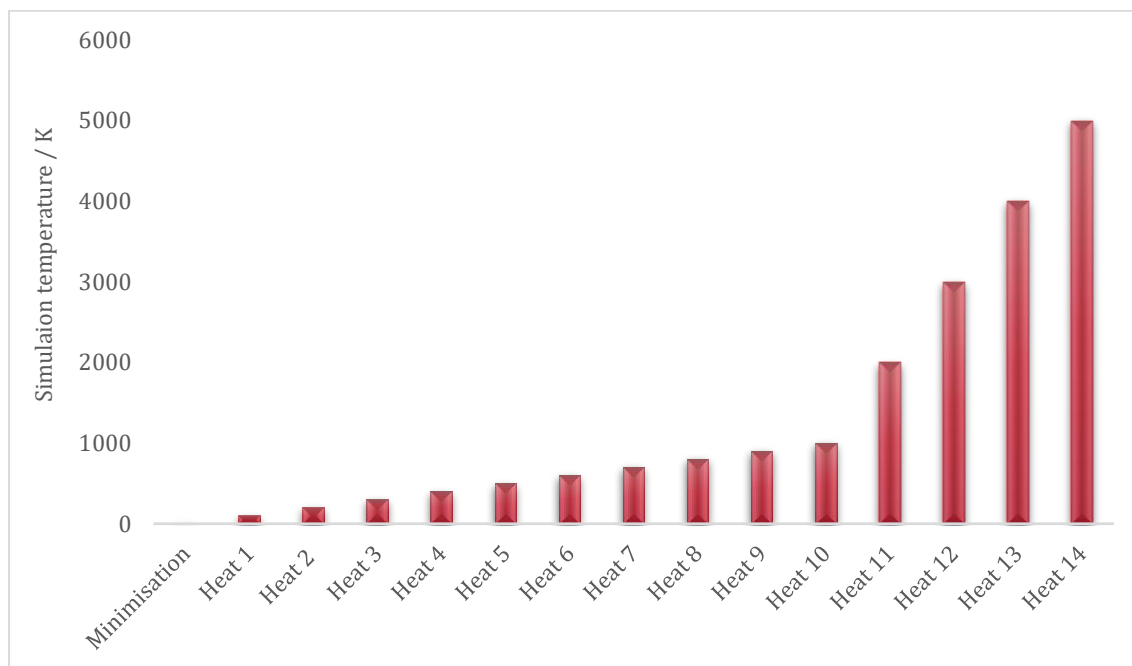


Figure 27- Graph to show only the heating steps from initial minimisation step to 5000K.

Figure 27 shows the temperature increments from minimisation step (10K) up until 5000K. At the end of each interval, the final frame (final configurational data including atomic positions and dynamic data) was carried over for the next simulation where temperature increased by 100K. This was continued up until 5000K. Quenching of B_2O_3 is outlined in the next chapter.

We also investigated a range of heating time-steps. As mentioned the traditional route to form glass from crystal occurs *via* a melt-quench route. The purpose was to identify the best possible steps to witness any changes within the structure of B₂O₃. The time duration for the simulations was in the range of 2-3 ns. Another important parameter is the heating rate **Table 3** summarises the simulations that were performed exploring different potential models (two- and three-body, denoted as “2” and “3”), heating rates and time steps. The results allow us to identify the potentials and simulation parameters needed to form models of amorphous boron oxide.

Table 3 - Heating conditions and rates used within this research

Simulation unit cell	Potential Used	Maximum Temperature (K)	Simulation Time(ns)	Heating rate x 10 ¹² (K/s)
B1	3	5000	3	1.67
B1	2	5000	2	2.50
B1	3	5000	2	2.50

Analysis using both structural snapshots, and MSD data allow us to gain insight into the structures modelled.

3.5: Results and Discussion

3.3 Interatomic Potential Models

Previous potentials used for modelling borosilicate crystals and glass include the van Beest, Kramer and van Santen (BKS) potential, which are both silica potentials but have been adapted to include borosilicate materials from x-ray data obtained from hydrated crystals of B_2O_3 .⁽¹⁰⁸⁾ This type of potential has been employed for the majority of simulations in the glass research field, as it is able to model the low-pressure structures of silica-based glass. Essentially, the BKS force field is a rigid ion model which is parameterised based on *ab initio* calculations. It also models with acceptable accuracy the experimental properties of quartz.⁽¹¹⁸⁾

Another force field used for the stable and metastable silica structures is the Sanders Potential.⁽¹¹⁰⁾, obtained by empirical fitting to properties of crystalline quartz, Although the Sanders potential has been proven to be effective for simulations of highly complex inorganic materials, it includes a shell model description of polarizability which makes its implementation in molecular dynamics more difficult. Both BKS and Sanders, although silica potentials, have been adapted and studied for borosilicate materials.^(119, 122)

The potentials used within this thesis are based on the interatomic potentials parametrized by Takada *et al.* which has previously been shown to accurately model the two polymorphs of B_2O_3 . The potentials were parametrized against crystallographic data.^(70,71)

The parameters of each of these potentials against the ones used in this simulation will be compared later in this section.

In considering potentials for B_2O_3 , we must note that the B-O bond shows both ionic and covalent character. Moreover, the structures are complex with varying bond lengths and angles as illustrated by **Figure 28**, which shows a portion of the structure of the B_2O_3 cell with the equilibrated bond lengths using the modelling techniques applied in this thesis. The image shows the atoms found within 8 Å of a central atom. The variation in bond length is apparent with the average comparable to the experimental average B-O distance of 1.47 Å by Zachariasen in his 1963 paper. ^(18,33)

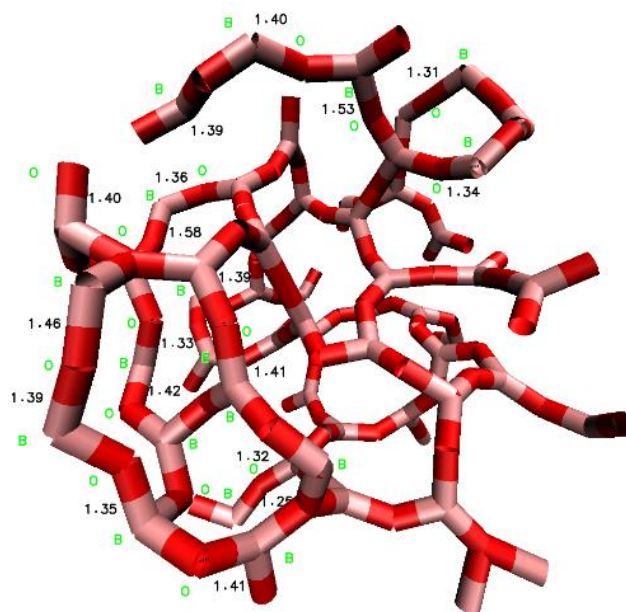


Figure 28 - Image showing B-O bond lengths of the simulated structure within 8 Å of index 20.

3.3.1: Forcefield definition

Forcefields can be expressed by the following general form. The assumption made here ignores the 4- or higher body terms as generally higher-order terms become less important.

$$E = \sum_i V_1(\mathbf{r}_i) + \sum_{i<j} V_2(\mathbf{r}_i, \mathbf{r}_j) + \sum_{i<j<k} V_3(\mathbf{r}_i, \mathbf{r}_j, \mathbf{r}_k) + \dots \quad (16)$$

The one body potential contains information on the forces from external sources, which may be ignored when considering only the interatomic forces within the system.

The 2-body or pair potential has been extensively used since it is able to model many structures simply with parameters that have physical meaning, and it is less computationally expensive than more complex potentials. However, the 2-body potential may not accurately capture the covalent bonding found within more complex systems. The 3-body potential does capture this information, as it accounts for angular effects.

3.3.2 The Two-Body Potential

Two body potentials consist of both long-range Coulomb interactions and short range repulsive and attractive terms. The former are handled by standard summation procedures which for periodic systems commonly employ the Ewald technique ⁽¹⁰⁷⁾. Short range interactions are described by a number of analytical forms of which for ionic and semi-ionic materials, a common one is the Buckingham potential:

$$\Phi_{12}(r) = A \exp(-Br) - \frac{C}{r^6} \quad (17)$$

Takada derived potential parameters for boron oxide by fitting to ab-initio data . Parameters are reported in **Table 4**, with the Buckingham potential used for B-B and O-O interactions.

Table 4 - Two Body Potential used in the simulation with the variables.

Bond	Potential	Charge, $q(e^-)$	A(eV)	$\rho(\text{\AA})$	C ($eV \text{\AA}^6$)
O-O	Buckingham	-0.8	1990.8	0.30	0.0
B-B	Buckingham	+1.2	323.1	0.30	0.0

For the B-O interaction, the Morse Potential was used as it accurately depicts the bond stretching interactions:

$$E_{morse}(\Delta R) = D(1 - e^{\alpha \Delta R})^2 \quad (18)$$

$$\alpha = \sqrt{\frac{k}{2D}} \quad (5)$$

D is the dissociation energy; the force constant is represented by α , and the bond length (R) are all included in this equation.

3.3.1 The Three-Body Potential

Next, we consider the three-body potential. Three-body terms are an addition made to a force field to consider the effects of covalency. Silicate and diamond structures have been simulated more accurately (in terms of bond length and coordination numbers) when using three-body potentials as they model the covalent directional bonding. ⁽¹²¹⁾

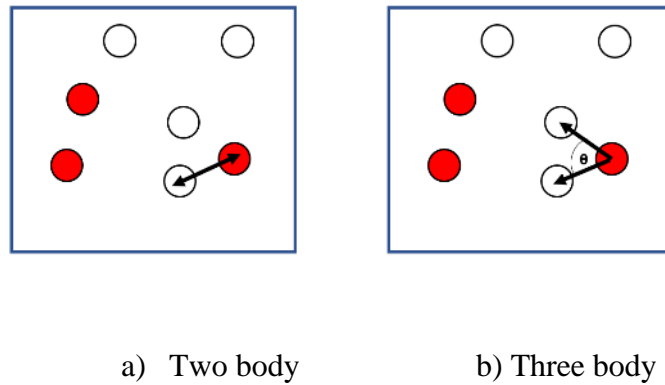


Figure 29 - Image representing two and three-body interactions.

Figure 29 illustrates diagrammatically the nature of both two and three-body interactions. The additional terms added to the force field are shown in **Table 5**. They represent the B-O-B and O-B-O bonds.

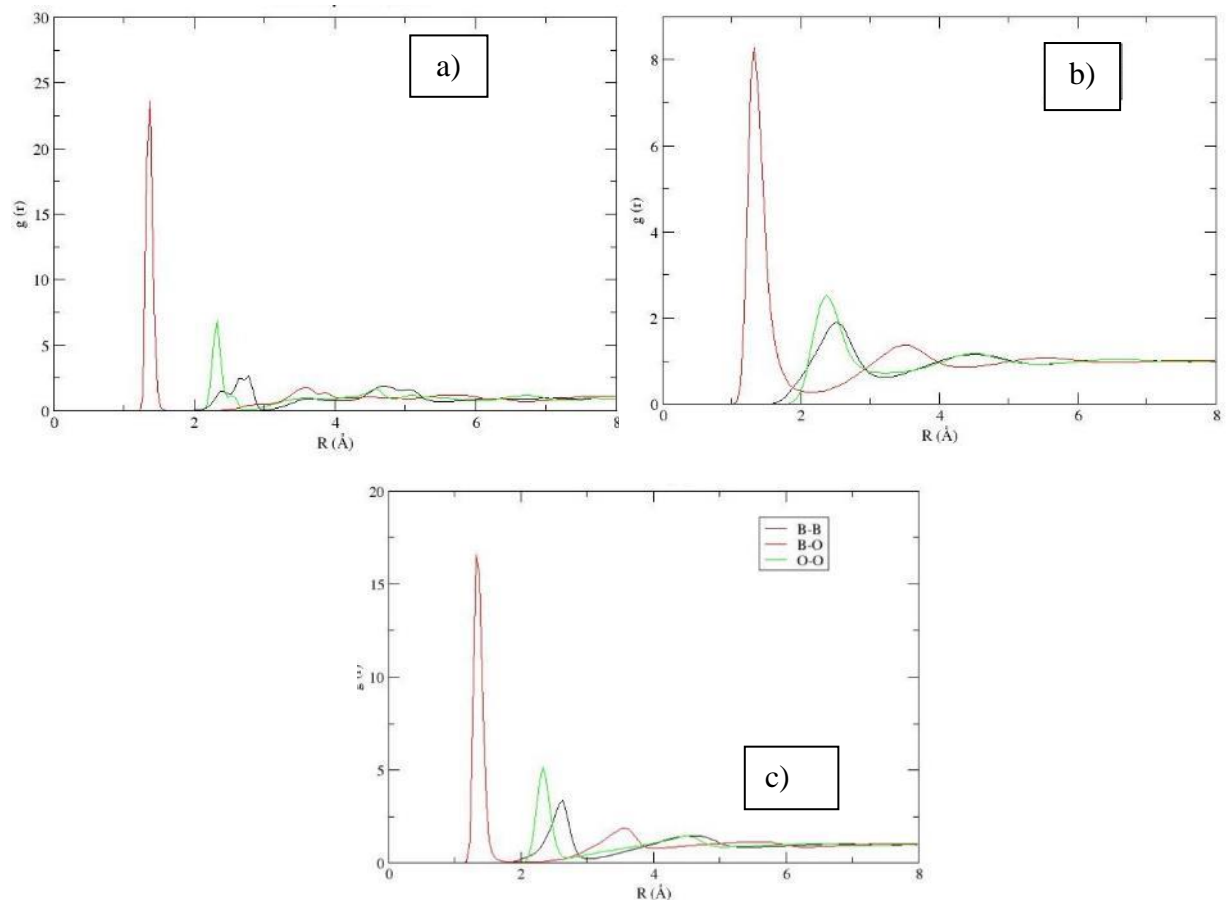
Table 5 - Additional three-body terms added to the Potential

Bond	Potential	Parameters			
O - B - O	Screen Harmonic	0.0	120.0	100000	1000
B - O - B	Screen Harmonic	1.6	131.0	100000	1000

3.5.RDF Data

The RDF (discussed in detail in **section 4.5.1**) gives valuable information on the short-range structure of a material or a liquid. This is seen from the graphs in **Figure 30** derived from two body potential simulations, which present RDFs for crystalline, molten, and quenched structures obtained using the procedure described in section 3.3 and with the 2-body potential. The crystal was firstly heated up to 5000K, at a heating rate of $2.50 \times 10^{12} \text{ Ks}^{-1}$. to ensure the structure was in the molten phase and

Figure 30 - Graphs showing the average RDF for the a) Crystal, b) Melt and c) Quench stages. The black showing B-B interaction, red lines show B-O RDF's and green from O-O.



then quenched down to 300K to the material's glassy phase.

The peaks in the crystal phase are, as expected, the sharpest and are indicative of a solid crystalline system.

The RDFs in **Figure 30** is analysed as an average across the simulations cycles through the systems crystal at minimisation step (a), melt at 5000 K (b) and quench returning to 300 K (c) phases. These data allow us to discuss the average B-O interatomic distances and it can be seen that as the system melts the peaks broaden as the atoms have more freedom of movement and exhibit a greater distance from its neighbouring atom. This can also be seen in the shift in the peak positions, from 1.32 to 1.42 Å. When quenched, the atoms regain considerable order and again, the peaks are less broad but not as sharp as seen with the crystal phases, at 1.35 Å. The RDF shown here is that derived from the use of the two-body potential.

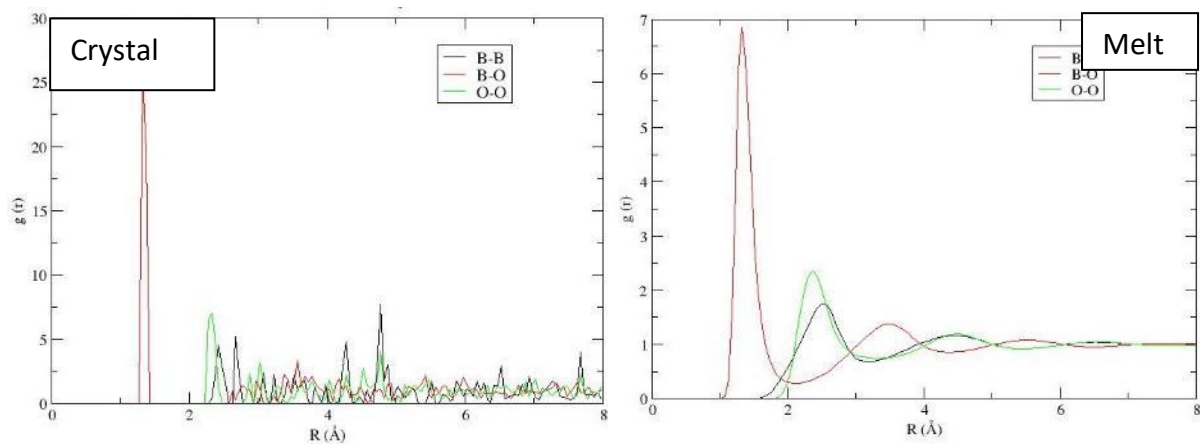


Figure 31 - RDF of the B_2O_3 system using the three-body potential.

On Including three-body terms different results are obtained. The RDF for the optimised structure in **Figure 31**, shows the effect of applying a three-body potential to the crystal structure. The crystalline phase now displays more and narrower peaks,

due to the additional restraints imposed by the bond bending term. When melted the system gave a similar RDF to the two-body counterpart with more broad peaks. The final RDF for the glass formation showed a sharpening of the first peak, but there is far less structure at the RDF at larger distances than found for the quenched structure for the two-body potential, shown in **Figure 30**.

Figure 32 is the B-O RDF in the quenched phase, at 300K. The initial large peak indicates the strong coordination of the first shell of oxygen atoms surrounding the boron. The RDF shows little pronounced structure beyond the first shell indicating little additional short-range order in the structure.

The experimental RDF from X-ray and Neutron diffractive methods - carried out by Hannon *et al.* and Ohno *et al.* respectively are comparable to the simulated results. We see that there is a peak at around 2.3 Å which is indicative of the O-O peak. As we move to the melt phase this peak broadens as expected. ^(97,127)

The calculated RDF also shows a series of blurred peaks at 2.70 Å which correlates to the interatomic B-B interaction. These peaks are associated with the various B-O-B bond angles. The crystal form has B-O-B triplets in the triangular subunits rather than rings.

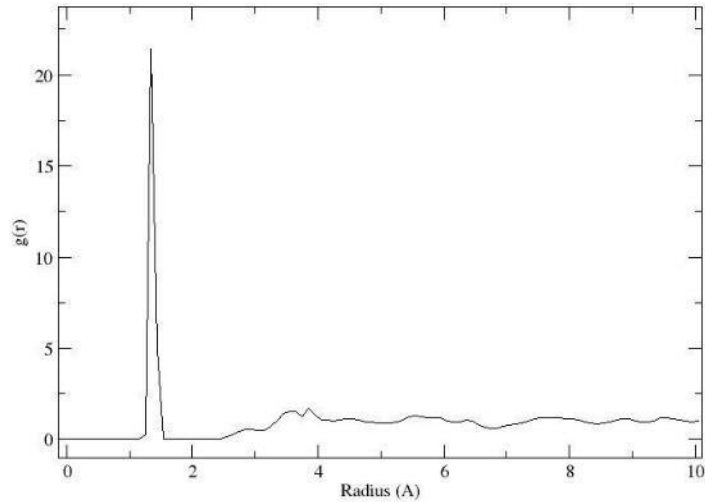


Figure 32 - Calculated RDF plot of glass for B-O at 300K.

Figure 33 shows the O-O RDF in the quenched amorphous system. Unlike the B-O plot, this shows a slight variation in comparison with the 2-body potential. There is one major peak that is distinguishable but little structure in the rest of the plot. However, the initial peak is still found 2.24 Å. There is another peak at 4.35 Å which is a shifted peak that was previously seen around 3.87 Å in the crystalline phase. Overall, we are again seeing an amorphous structure with little, short-range order beyond the first coordination shell.

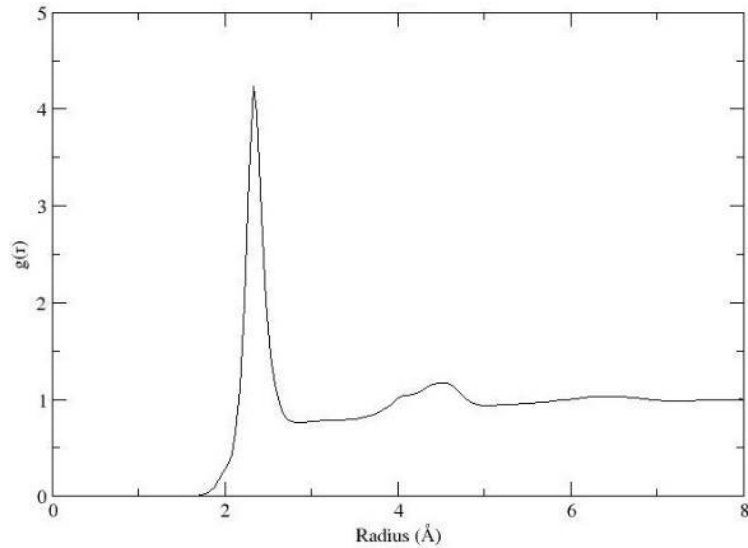


Figure 33 - Oxygen-Oxygen RDF plot at 300K during the glassy phase.

3.3.1.1 Atomic Diffusion

Initially, the B_2O_3 crystal, using the same system size, 480 atoms, used by Takada *et al.* was investigated. The crystal was heated up to 5000K, at a heating rate of $2.50 \times 10^{12} \text{ K s}^{-1}$ to ensure the structure was in the molten phase and then quenched down to 300K to the material's glassy phase.

Each system was then compared to the structural geometry exhibited in the minimised crystal stage in **Table 6**. The frames captured in this analysis were the final frames of each of the phases, i.e., the single average minimised crystal frame at the end of each simulation phase, at 10K, 5000K and the quench phase of 300K. The displacement of atomic positions was compared to determine each phase.

Table 6 - RMSD from Crystal to Glass Phase

Structure Phase	RMSD (Å)	
	Two Body	Three-Body
Crystal	-	-
Melted Phase (5000K)	38.505	47.9429
Quenched Phase (300K)	12.354	48.0459

The RMSD values shown in **Table 6** signify large displacements on melting regardless of which potential was used. However, when the three-body potential was used, there is a more notable change in the average structural arrangement in this portion of the simulation. The percentage difference can be calculated according to the equations below. The N integers looks at spatial atomic positions from the start and end of a simulation, looking at an overall system movement to understand the displacement of atoms. So, if we are able to see a huge percentage change, we can then help determine the system phases, as molten states will show greater movement.

$$\text{Percentage Difference} = \frac{|N_1 - N_2|}{\frac{(N_1 + N_2)}{2}} \times 100 \quad (20)$$

$$\text{Percentage Change} = \frac{(N_2 - N_1)}{|N_1|} \times 100 \quad (21)$$

Where N_1 and N_2 are integers and $N_2 > N_1$.

In the case of the crystal to melt, between the two potentials, the value equates to 21.83%, showcasing a 19.69% decrease. This value indicates the movement of the coordinates from the original crystal structure frame and the final frame of our simulation at 5000 K.

We note that the cycle from crystal to quench, encompasses two phase changes and the structural changes are likely to be more drastic than the single change to the molten phase. Yet, we see that the two-body potential fails to capture this feature, hence signifying a drawback of application of two-body potentials for this system. The visualisation of B_2O_3 at these stages provides answers to why this is the case.

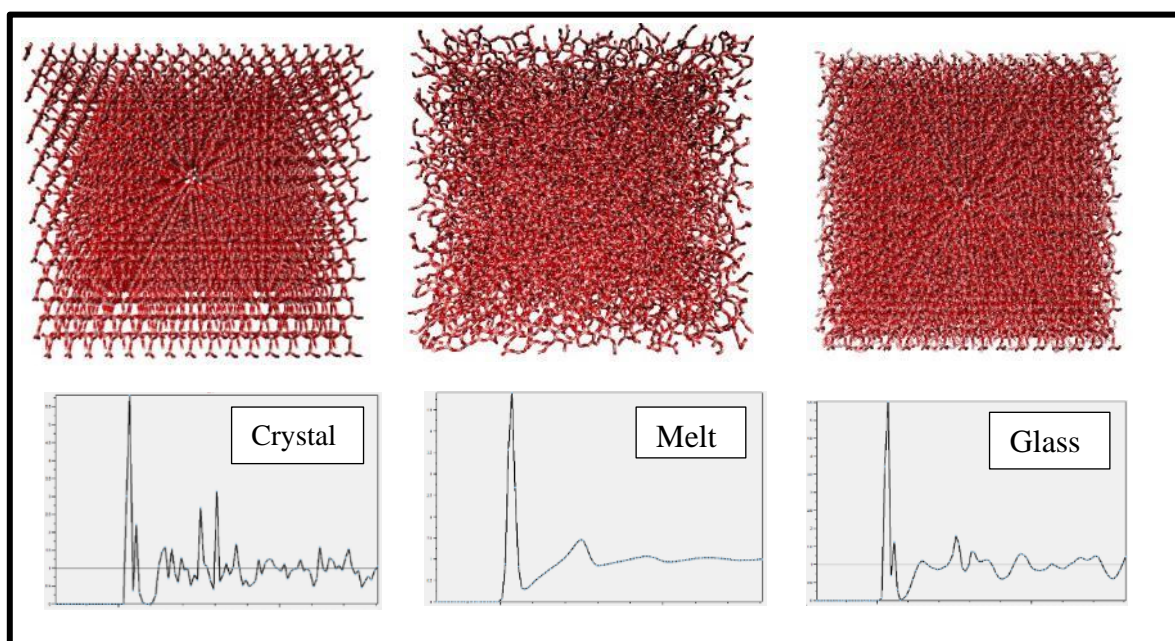


Figure 34 – Ball-and-stick models of B_2O_3 of Crystal, Melt and Glass Phases for the Two-Body Potential, alongside their respective O-O RDFs.

Figure 34 illustrates the structure calculated with the two-body potential, by taking snap shots from the simulations. It also displays an RDF of the O-O bond to outline the changes in peak distribution and profile. We see that the quenched phase displays a structure that is very similar to the crystal phase. To avoid this “*recrystallisation*” seen with the two-body potential the three-body potential were utilised for the simulations post molten state. The quench stages which are experimentally rapid were required

to run for a minimum of 2.5-3 ns before the glassy-B₂O₃ could be formed which corresponds to a cooling rate of $12 \times 10^{11} \text{ K s}^{-1}$.

3.3.1.2 Atomic Diffusion

MSD Plots provide information on atomic diffusion as discussed previously. The MSD for the melt stage for 1ns using this two-body potential can be seen in **Figure 35**. The plot shows that both B(black) and O (red) have a similar diffusion behaviour.

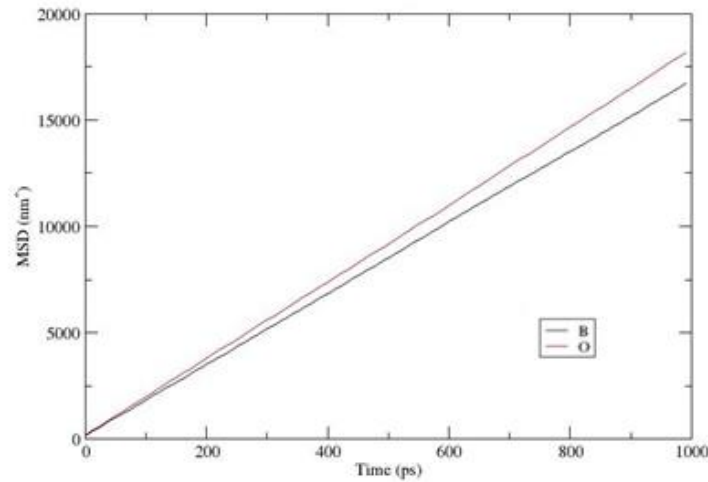


Figure 35 – MSD plot for B and O in melted B₂O₃ using the two-body potential (with Boron atoms in black and Oxygen in red).

MSDs were also calculated for the simulations with the three-body force field utilised, **Figure 36**. Comparing to the two-body potential, the gradient is less steep indicating slower diffusion. The plots are both linear, indicating Fickian diffusion behaviour. ⁽¹²⁸⁾

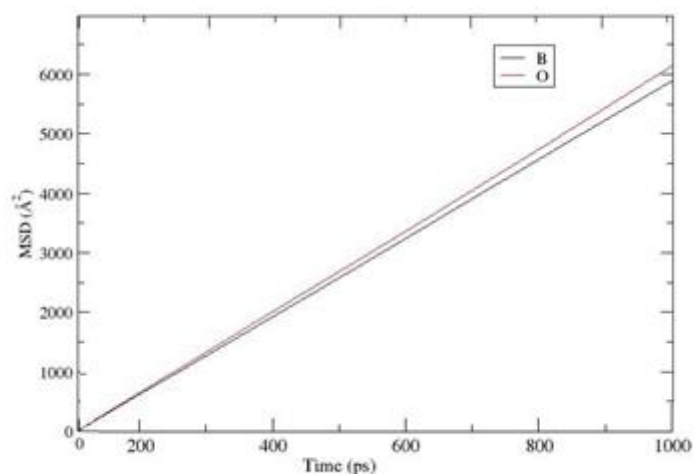


Figure 36 - MSD plot B and O in melted B_2O_3 using the three-body potential (with boron atoms in black and oxygen in red).

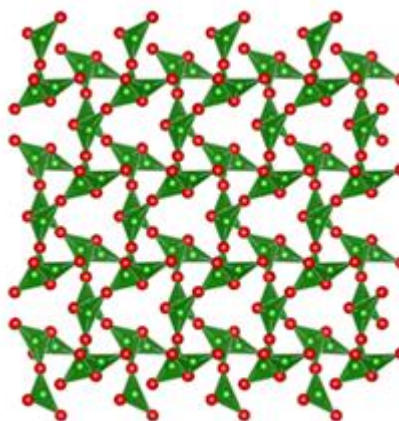
3.3.2 Comparison of Force Field Performance for B_2O_3 Crystal, Melt and Quench structures

In the case of the A1 crystal, **Table 7** shows a distortion index which was calculated as 0.0143 Å. The distortion index looks at the structure in terms of ideal values of structure within certain groups. If a group is in a trigonal planar group the atoms will be expected to be angled at 120° , the distortion index would observe the distance it varies from the ideal. The trigonal planar polyhedra were found throughout the system. When moving to the final quenched phase using the three-body potential it was witnessed that the average coordination number of boron was closer to 4 than previously seen with the melt and crystal counterparts providing values of

approximately 3. The distortion index in the melt phase was now 0.297 Å indicating that the polyhedra are less uniform.

Table 7 – Polyhedra representation of the pure crystalline B₂O₃ system together with a table containing volumetric and coordination number data.

B-O	Average Length (Å)	Effective Coordination Number
Crystal	1.38	2.97
Melt	1.34	2.99(87)
Quench	1.45	3.86



The coordination numbers were seen in the crystalline and molten phases to approximate to 3. This is in agreement with the averaged observed coordination number (AOCN) of a B³⁺ cation to Oxygen as noted by Brown *et al.* with a value of 3.5.⁽¹³¹⁾

As we move to the quenched structure using the three-body potential the effective coordination within the polyhedra increases to 3.86, which would indicate a change in the trigonal planar groups and is suggestive of the boroxol ring's structure which would give a coordination number of 4. The B anions are thought to have a bonding strength of 0.33 valence units which is large in comparison to other anions, such as P and N which have a strength of 0.25 and 0.11 valence units. ⁽¹³¹⁾

3.4 Summary and Conclusions

This chapter shows that for the crystalline phase both the two and three-body potential produce experimental result well. For the molten phase, diffusion is faster when the two-body potential is used, but nevertheless, a molten structure is simulated. Only the three-body potential can adequately generate a glassy structure via the melt quench procedure, showing that the angle dependent terms in the potential arising from the directional nature of the bonding are vital for stabilising the amorphous structure and preventing recrystallisation.

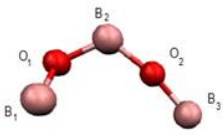
<i>Atom</i>	<i>X</i>	<i>Y</i>	<i>Z</i>		<i>Bond</i>	<i>Angle (°)</i>
<i>B1</i>	7.485	12.177	22.665		<i>B1-O1-B2</i>	121.46
<i>O1</i>	6.819	12.415	21.615		<i>O1-B2-O2</i>	114.18
<i>B2</i>	7.478	12.748	20.584		<i>B2-O2-B3</i>	167.661
<i>O2</i>	8.497	12.569	20.087		<i>B1-O1-B2-O2</i>	46.65
<i>B3</i>	9.354	11.602	19.702		<i>O1-B2-O2-B3</i>	25.46

Figure 37 – B_2O_3 non-ring segment highlighting the specific atoms.

4 MOLECULAR DYNAMICS STUDIES ON BORON TRIOXIDE

4.1 Abstract

This chapter reports MD simulations on three phases typically seen during glass production, namely the crystalline starting material, the molten state, and the final amorphous quench phase. The focus of analysis has been on the identified phases of the crystal, at the optimised step, molten state (5000K) and the amorphous structure (300K). The main focus was to investigate key moieties within this material alongside the frequency of the debated BO_3 and BO_4 groups. Where previous chapters have thoroughly investigated the use of the two- or three- body potential, this chapter will heavily focus on the structure and dynamics at each stage of glass production, building on the data obtained from the previous chapter.

Through analysis of a system of B_2O_3 containing 480 atoms, hereby known as the *A1 system*, distinct peaks pertaining to the RDF data were observed. Alongside this information, the proportions of rings could then be analysed.

Where discussions in this area of research have been the BO coordination, our investigation has led to the calculated radius ratio for our system is 0.1842. This is consistent with the type of voids found for triangular planar groups such as B_2O_3

with a coordination number of 3. Providing information which indicates some boroxol ring formation. Yet the BO_3 trigonal groups remain most dominant. The rings statistics also revealed that most of the boron and oxygen atoms were 3 and 2 coordinated. However, a smaller portion, 12.5% (B) and 8.33% (O) are 4 and 3 coordinated.

4.2 Aims and Introduction

As mentioned previously, the network structure of B_2O_3 is still a matter of debate. Although it is known as one of the best glass-forming materials, the difficulty arises from characterising the network structure including the presence and frequency of the tetrahedral subunits, BO_4 , and the planar subunits of BO_3 . These two subunits are the crux of identifying how the B_2O_3 glass network is connected. Moreover, the introduction of ring structures such as boroxol rings adds to the intricacy of the networks as seen in **figure 38**.

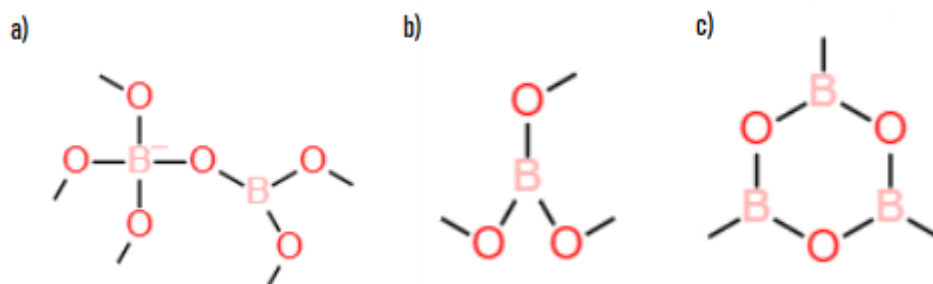


Figure 38 -The Boron Trioxide subunits; a) BO_4 , b) BO_3 and c) Boroxol ring.

The current chapter investigates the pure B_2O_3 structure *via* MD simulations, using the DL_POLY code⁽¹⁰⁴⁾ (see **chapter 2**) to undergo a series of minimisation, heating and quenching sequences. The structural property analysis provides a greater understanding of network connectivity alongside chemical data but moreover, gives insight into the structure of this network former. The main aim of this chapter is to characterise how the bonds vary throughout the structure and what their specific role is within the network and more importantly how this bonding varies within the glassy system in comparison to the crystalline structure which will be investigated at varying temperatures and pressures.

4.3 Structural Model and Computational Details

The A1 simulation cell structure, shown in **Figure 39**, was generated as a supercell, in P1 symmetry, of the crystal structure described by Johnson *et al.*⁽¹³²⁾. This crystalline polymorph of B_2O_3 , denoted B_2O_3 -I, is obtained by crystallisation at ambient pressures. It is the same crystalline phase as that studied in chapter 3, containing threefold coordinated B and twofold coordination of O. Experimentally, there is also a denser phase, B_2O_3 -II synthesised at higher pressure, but for which few physical properties have been measured, apart from the crystal structure.⁽¹³³⁾

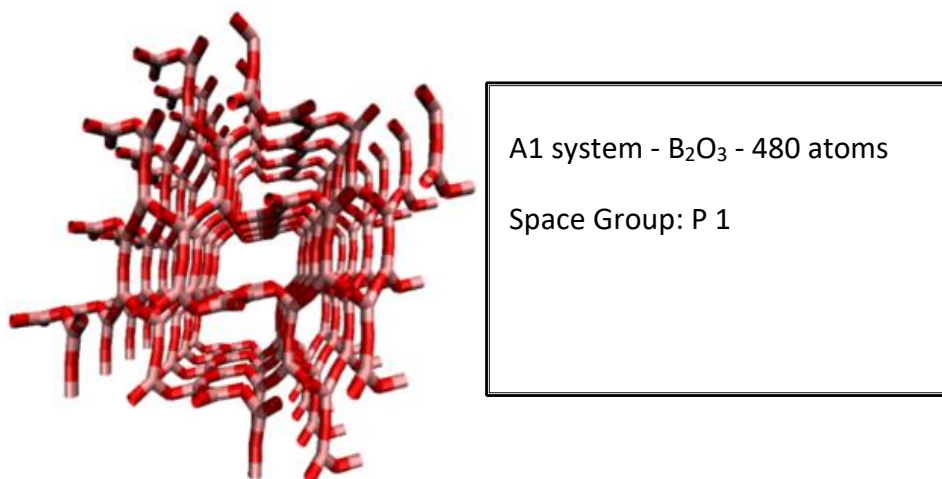


Figure 39 – A1 system for B₂O₃ threefold-coordinated boron. Visualised using VMD software

B₂O₃-I crystallises in the chiral trigonal space group P3₁21, but in the A1 simulation cell the symmetry is removed so that all atoms are symmetrically independent. The periodic A1 cell contained a total of 480 atoms, 288 oxygen and 192 boron.

To model the B₂O₃ crystal accurately, a minimisation run is initially carried out which provides a starting point for further dynamic simulations. The structure at the minimum is the most stable atomic arrangement at zero kelvin.

A zero-kelvin dynamic run carried out using DL_POLY effects the minimisation. The force field for this simulation was the two-body potential described in chapter 3 as we are primarily focussing on the crystalline and molten phases. The Ewald method which was employed to calculate the coulombic interactions between atoms.

Figure 40 shows how the energy of the system varies over the course of the minimisation run. The energy converges to around -321000 kcal/mol (7.4×10^6 eV) by about 1 ps, showing that a minimum was found.

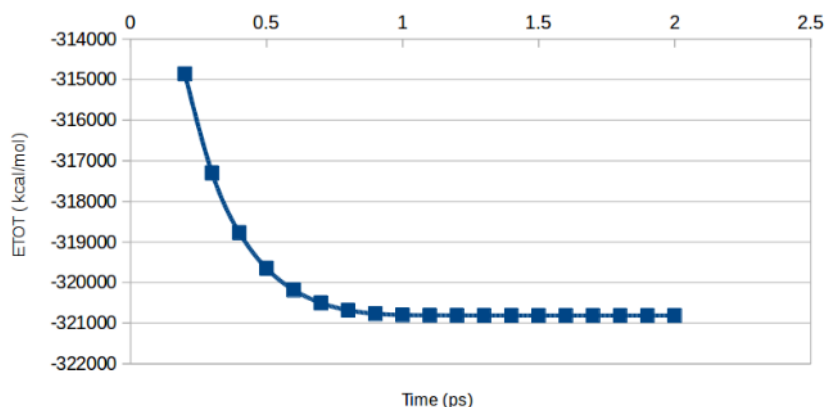


Figure 40 Evolution of the total energy of A1 system with time, during zero Kelvin minimisation run.

The next simulations were done in the Isothermal-Isobaric (NPT) ensemble. The NPT method was adopted to avoid any unrealistic constraints to the simulation box and also to aid in the possible generation of fourfold boron coordination, which is associated with higher density systems. The system was run at a series of temperatures and with various durations to create the molten phase of the B_2O_3 ,

During glass manufacture, the materials undergo a slow heating and rapid quench. In order to approximate to this process, the MD simulations involved a continuous heating stage from 0 K to a maximum temperature of 5000 K over a simulation period of 1 ns, followed by quenching to 300 K. The MD timestep for all simulations was 1 fs.

The quenching of the systems was broken down into two sub-steps. Initially, the system was cooled down by 100 K intervals. Each of these increments was for 3000 timesteps. Once the temperature reached 300 K, the system temperature was kept

constant for 10,000 timesteps. The temperature of 5000 K was chosen to ensure melting of the crystalline phase. Although data is sparse, experimental studies indicate a melting temperature for crystalline B_2O_3 of about 730 K. However without defects present in the model to initiate bond-breaking, MD simulations are known to have a tendency to significantly overestimate the melting points of crystalline solids. ^(134,135)

4.4 Results and Discussion

4.4.1.1 Radial Distribution Functions

Figure 41 shows the RDFs calculated for the minimised A1 system, which provide information on short and medium-range order. The plots are characterized by sharp and well-defined peaks, which is expected considering this system is a supercell of a crystalline material. The B-O RDF shows by far its strongest peak 1.401Å, indicating a narrow distribution of B-O bond lengths found in the crystalline system. Experimental values for this system vary between 1.34 and 1.41 Å, with this range being characteristic of trigonal BO_3 units. The sharp peak seen here acts as a fingerprint indicating the overwhelming majority of the boron is present in BO_3 .

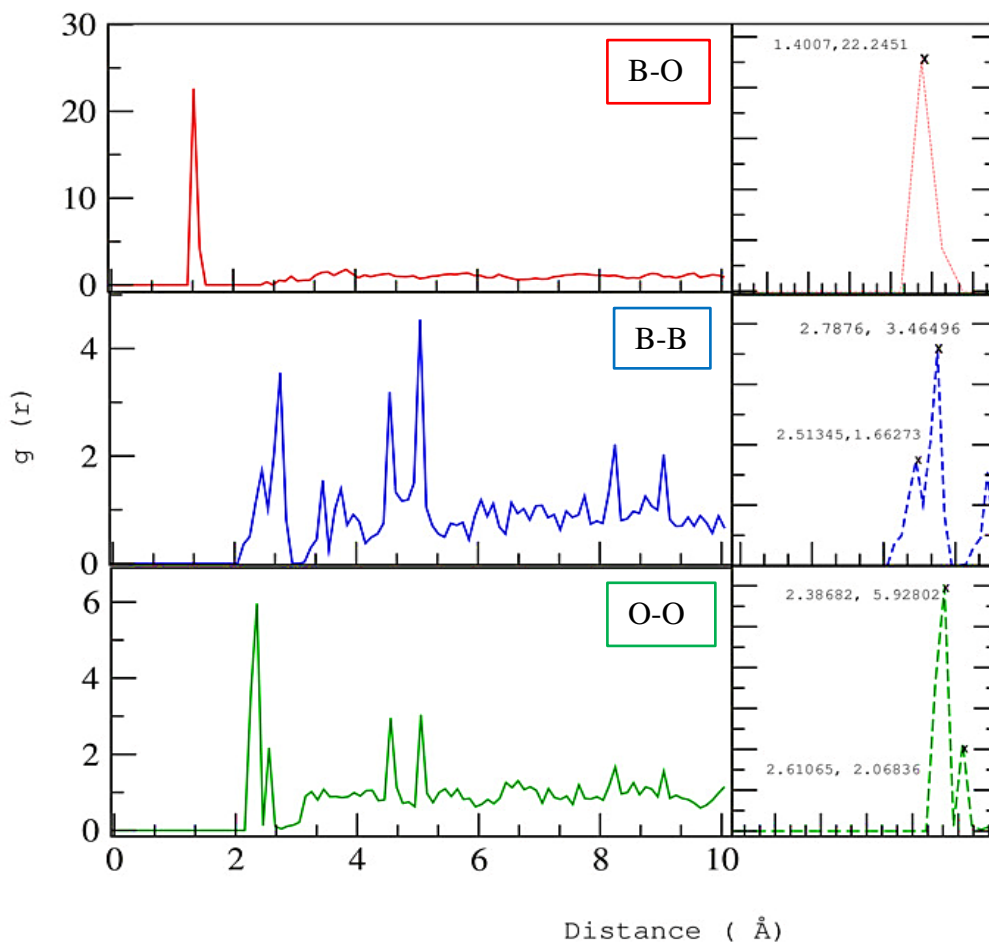


Figure 41 - RDFs for minimised A1 crystal with a zoomed section to highlight significant peaks.

As expected, there is no peak in the region 2.60-2.70 Å, which would indicate the presence of boroxyl rings. Instead, there is a small peak centered at 2.85 Å, which corresponds to the closest non-bonded B-O distance observed in B₂O₃-I.

The B-B RDF plot shows a host of sharp peaks out to relatively high r values, as expected for a highly ordered crystalline material. There are two prominent peaks at 2.51 and 2.79 Å. The peak at 2.79 Å has a greater $g(r)$ value and would indicate a linear,

or near-linear, B-O-B linear subunit. The 2.51 Å peak represents a B-O-B group with a bond angle of around 120°

For O-O there are two significant peaks at 2.39 and 2.61 Å with the former corresponding to O-O distances within BO₃ subunits and the latter indicating an O-O distance in a ring structure, or between two adjacent BO₃ units, though the distances are slightly lower than those reported previously. ⁽¹³⁸⁾

As seen in **figure 42**, the bond length of the oxygen enclosed by the two boron atoms in the ring, with the oxygen outside the potential boroxol ring should be 4.10 Å. Whilst the same internal oxygen is expected to have a distance of 2.73 Å towards the boron opposite it.

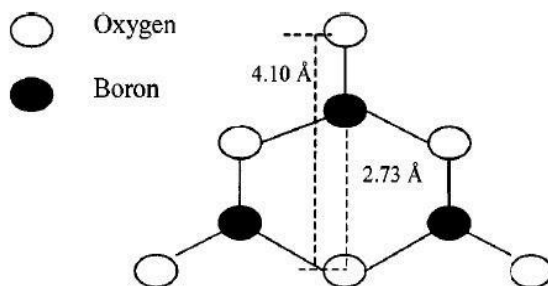


Figure 42 - Boroxol ring length as suggested by Maranas *et al.* ⁽¹³⁸⁾

The values seen for the ring present in this project at this stage for the inter-ring distance of boron to oxygen is 2.57 Å. This is close to what has been seen with research on boroxol ring distances, **figure 42**, as seen in Maranas *et al.*, of 2.73 Å. However, the difference is still -0.164 Å. For the bond distance between the oxygen within the ring and the one outside the ring, is smaller than expected, producing a value of 3.87 Å. ⁽¹³⁸⁾

4.4.1.2 Density and Enthalpy

In the minimized state, analysis of the equilibrated thermodynamic properties of the pure B_2O_3 system can be conducted. **Table 8** shows a few of these properties.

Table 8 - Breakdown of the total energy for the equilibrated B_2O_3 system.

Quantity	Final Average Values (eV)
Total Energy	-4516.4
Volume (\AA^3)	6029.0
Enthalpy	-4880.1
Configurational Energy	Final Average Value (eV)
Van der Waals	-1137.4
Electrostatic	-3436.1

The enthalpy value is related to the lattice energy and is solely dependent on the interatomic potential that is used. Another factor dependent on the potential is the energy partition between the van der Waals (vdW) and electrostatic values. This will be compared between the phases. VdW energy arises from the short range potentials used, whereas electrostatic is dependent on the partial atomic charges present and is influenced by density as well as by local interatomic distances. ⁽¹³⁹⁾

Alongside vdW forces, the electrostatic interactions can also affect the network structure. The value is -3436.1 eV in this system. Finally, the valence angles, seen in **Table 8** are essentially an angle/vector that aids the representation of a bond through the linkage of ions in an electric field. The bond bending terms are described here for the system as a whole. Pure B_2O_3 valence angle has a value of 57.095 eV and is connected to three-body terms in the interatomic potential discussed in the previous chapter.

After the equilibration step and reaching an equilibrium state, the simulation was taken to the next stage of heating the system. At this point, the volume is 6029 Å³ and is an important quantity due to the use of NPT ensemble. An NVT ensemble would keep the volume constant. More importantly, the volume is a key value for comparison to the molten and glassy phases of the crystal as it directly influences the density of the glass.

Using the volume, the density of the unit cell can be derived - using the formula below

$$\frac{Z \times M}{a^3 \times N_A} \quad (22)$$

where Z is the number of atoms per unit cell, M is the molar mass, a is the cell edge length and finally, N_A is the Avogadro constant. Therefore, the final value for unit cell density equates to 2.543 g/cm³.

4.4.2 Molten B₂O₃ System

The work of Krogh-Moe on alkali-borate glass studies predicted that the B₂O₃ network contained a mixture of boroxol rings and trigonal planar triangles as discussed previously. ⁽¹⁶³⁾ Their research results were based on many experimental techniques including NMR and X-ray diffraction. However, the debate concerning the presence of rings and more importantly their frequency is still in question. ⁽³³⁾

The A1 crystal was heated up to 5000K to ensure the structure was fully in the molten state. Subsequently, the network was observed again to see if there were any changes within the structure. Here we present the data for the molten B₂O₃ structure at 5000K averaged over 1 ns.

Running the melt stage for 1ns, the presence of boroxol rings can be observed. However, as the temperature is increased to a maximum of 5000K, these rings dissipate very quickly. In fact, the appearance and disappearance of rings is a feature of the melt simulation at this temperature. For example, **figure 43** illustrates a case where a boroxyl ring breaks up and then reforms over the course of the MD simulation.

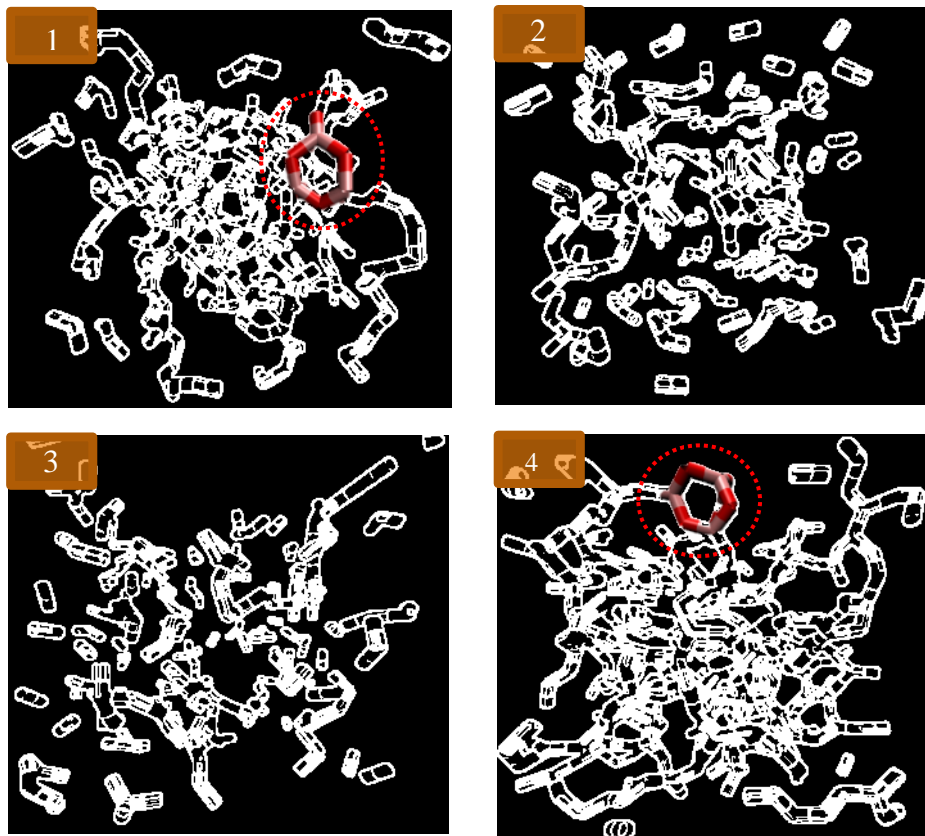


Figure 43 – Evolution of the ring reformation during B_2O_3 Melt process in different stages. Labels indicate capture at the corresponding timeframe with 1= 10ps, 2 = 250ps 3 = 500ps and 4= 1ns.

On inspection of **figure 43**, there is not an abundance of ring units present in the **A1** structure after melting and, correlates with the pure B_2O_3 crystal which produced RDF data with small indication of the BO_4 subunits. The plots display smoother curves for

all distances, which is due to a reduced-order within the system alongside simulations being time-averaged. When the temperature is increased, bond breaking, and reformation occurs. The once regular structure of the crystal is fragmented and the molten B_2O_3 now has a structure that has lost long-range order. These figures also show that there is a reduced intensity of peaks and indicates a liquid-like structure. The initial peaks have now moved to smaller values for each of the interactions with the values for the initial peaks now being 1.351, 2.464 and 2.387 Å respectively as compared to the crystalline values of 1.401 Å for B-O, 2.513 / 2.788 Å for B-B and 2.387 / 2.611 Å for B-O.

The data presented in **Figure 44** match experimental data by Miyake *et al.* for molten B_2O_3 for the B-O RDF, where this experimental data showed a maximum for the first peak to be 1.36-1.37 Å. ⁽¹³³⁾ The value corresponds to the planar BO_3 triangles which imply that the molten system is largely consistent with BO_3 triangles. For BO_4 tetrahedron structures to be present a peak would have to appear roughly 1.47 Å according to this experimental analysis by Miyake *et al.* ⁽¹⁴³⁾

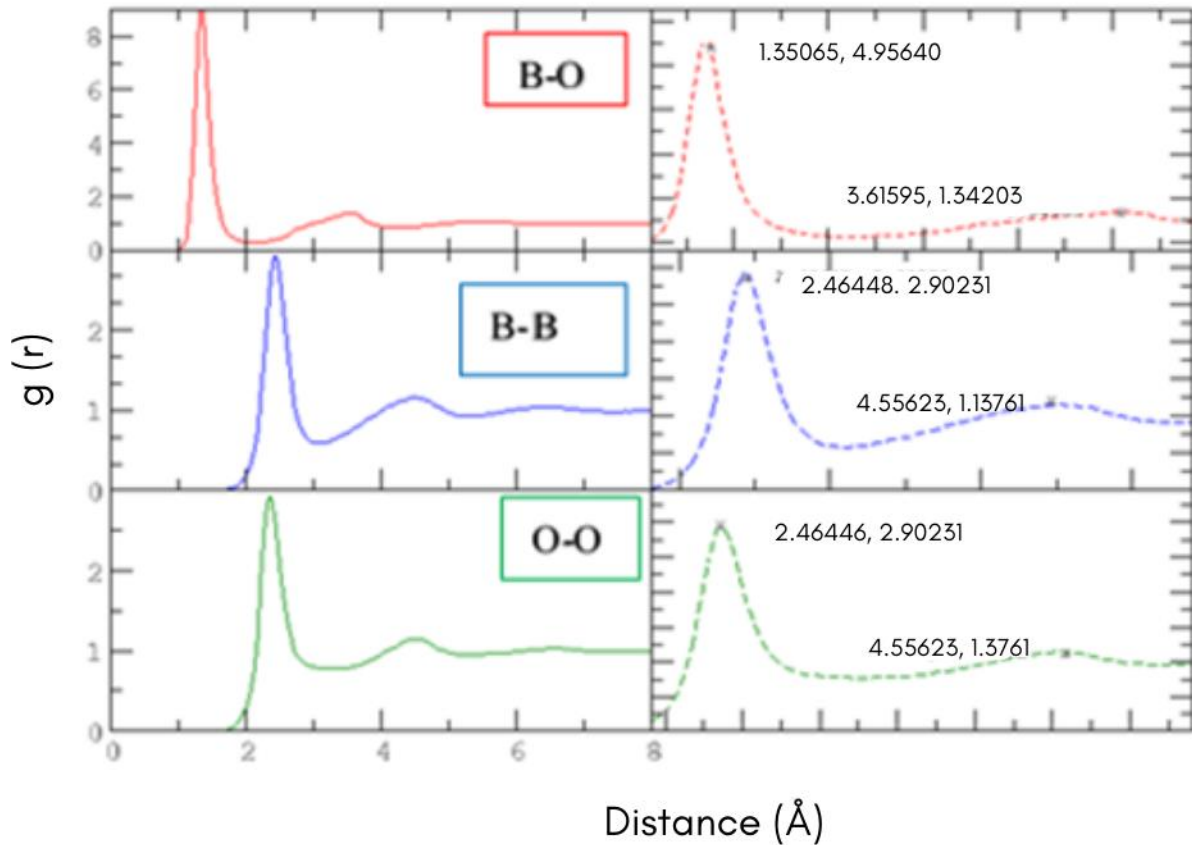


Figure 44 - RDF of A1 system at 5000K. Zoomed sections are inserted to highlight significant peaks.

The experimental peaks for B-B and O-O were found superimposed with their maxima of 2.38 \AA . The values from the results in this study were 2.464 and 2.387 \AA respectively, providing data that indicates a greater B-B distance yet being close to the experimental value. These peaks are characteristics of regular BO_3 units. In both the B-B and B-O cases there are a few peaks that follow, at 4.56 and 4.58 \AA , respectively. The peaks form due to the layering within the system. The distances of atoms above and below the ones in the plane in question. Whether there are boroxol or triangle units present, there will be oxygen and boron in close vicinity of the atoms in question - not only sequentially but between layers. **Figure 45**, although not the structure being researched in this project, displays an example of the inter-planar distances.

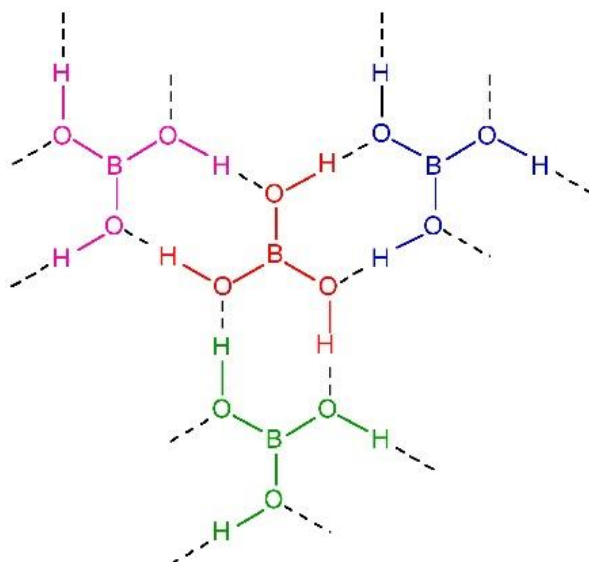


Figure 45 - Image showing boric acid and the layering effects. Each colour showing a different layer connected through intermolecular hydrogen bonding. ⁽¹⁴⁴⁾

4.4.2.1 Molten B_2O_3 Substructure Analysis

The data obtained from the simulations indicate that there are a variety of distinct and recurring structural units within all three phases of the B_2O_3 structure. The molten phase specifically, provides enough energy for bond breakage and reformation. Hence in this phase, there may be a larger frequency of different groups.

To investigate the groups that occur within the simulation cell for this molten B_2O_3 structure, substructure analysis can provide information on network connectivity, and evolution of the molten and vitreous structures. To calculate the frequency and occurrence of specific rings, the R.I.N.G.S code was utilised. ⁽¹⁴⁵⁾

The data revealed that the configurations of boron atoms within molten B_2O_3 had 87.5% ($n=4536$) of atoms in the three-fold coordination, with the remaining 12.5% ($n=648$) having a coordination number of 4. The oxygen atoms had a larger portion of atoms with coordination of 2, 91.67% ($n=7128$). The 8.33% ($n=647$) remaining were in the coordination of three. In this structure, there were 648 tetrahedra, 216 (80%) being corner-sharing and 432 (20%) being edge-sharing, **figure 46**.

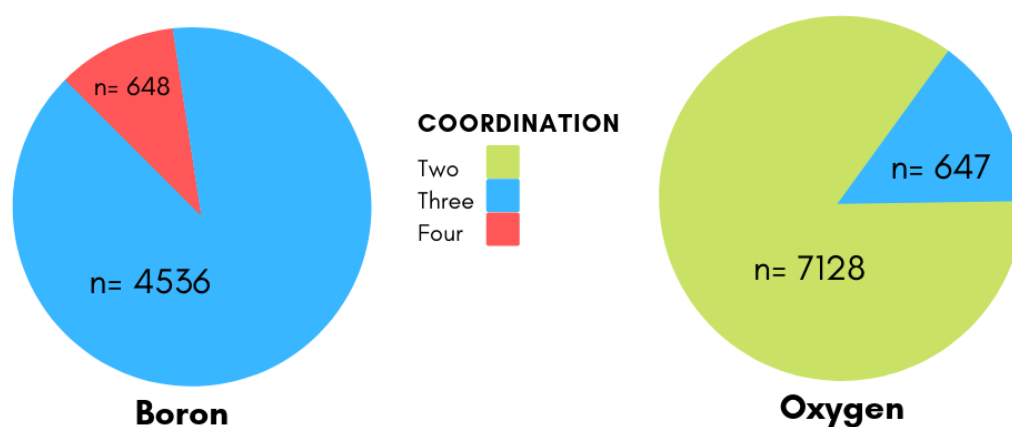
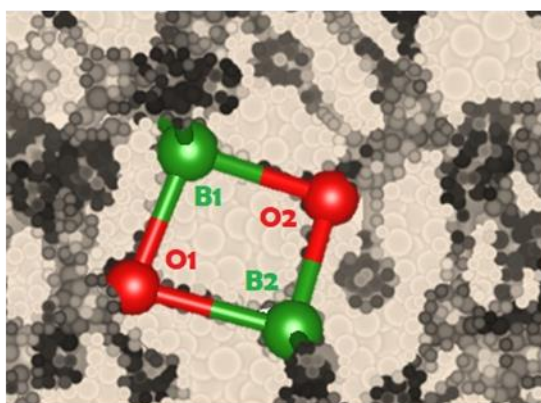


Figure 46 - Pie Charts revealing coordination within the system for both boron and oxygen atoms.

The most common structural sub-units in the structure were the BO_3 groups and in all three phases (crystal, melt and quench), there were far more trigonal planar groups than any other.

It is expected the once uniform structure, dissipates to a more convoluted/disorder network of atoms. At higher temperatures, extensive reorganisation can occur. As mentioned above, the boroxol ring is present in the molten structure but there are also multi-membered ring structures, some of which are prevalent throughout the different phase configurations, and some were unique.

One such ring was the 4-membered ring seen in **figure 47**. This group adjoins two of the three-membered triangular structures. The distances and angles of this ring structure were calculated and displayed in **figure 47**. The bond distances show that the O1-B2 bond is significantly larger than the rest of the bonds within the four-membered ring.



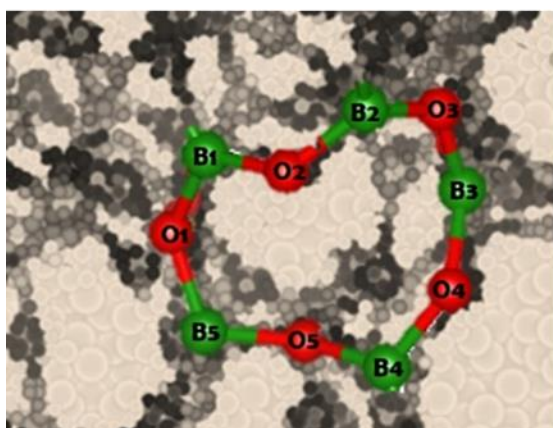
Bond	Distance (Å)
B1 - O1	1.54
B1 - O2	1.59
O1 - B2	1.73
B2 - O2	1.48
Bond	Angle (°)
O1 - B1 - O2	94.55
B1 - O2 - B2	90.04
O2 - B2 - O1	91.42
B2 - O1 - B1	82.89

Figure 47 - Image showing a 4-membered ring highlighted with corresponding distance and angle information.

From this table, we can see that the average distance of the B-O is 1.59 Å, with all B-O bonds longer than the 1.40 Å found in the crystalline phase. If comparing this to the triangle subunits or boroxol rings, these 4-membered rings require smaller bond angles which creates strain. It should also be noted that the boron atoms were still 3 coordinated. However, we can see from the angles noted that this ring structure would be very strained, due to the angles being around 90° and less. Therefore, this structure would not be stable and perhaps an intermediate structure found by the simulation runs. They also would not be found as commonly as other structural units.

Rings analysis showed that in this A1 structure of pure molten B_2O_3 , a 10-membered ring occurs, **table 9**. This showed a greater range of B-O-B angles, though with lower B-O distances commensurate with 3-coordinate B found in B_2O_3 -I. 10-membered rings can also be found within amorphous SiO_2 structures, where the most common ring sizes are 6 and 10.^(146,147)

Table 9 – Image showing 10-membered ring structure distance and angular values with the corresponding reference image



Bond	Distance (Å)
B1 - O2	1.40
O2 - B2	1.37
B2 - O3	1.38
O3 - B3	1.37
B3 - O4	1.42
O4 - B4	1.43
B4 - O5	1.38
O5 - B5	1.37
B5 - O1	1.37
Bond	Angle /Dihedral (o)
O1 - B1 - O2	119.44
B2 - O3 - B3	126.21
B3 - O4 - B4	132.55
B4 - O5 - B5	133.07
O1 - B1 - O2 - B2	141.19
O2 - B2 - O3 - B3	28.66
B2 - O3 - B3 - O4	33.52
O4 - B4 - O5 - B5	104.16

4.4.3 Quenching the System

To form glass, (**section 1.2.1**), liquids undergo rapid quenching. Therefore, to replicate this stage as accurately as possible, it is important to cool the molten structure at suitable cooling rates. To this end, a series of simulations were carried out to identify the fastest rates in which the glassy-B₂O₃ can be formed. Experimentally, this can be useful for reducing costs for cooling/quench stages.

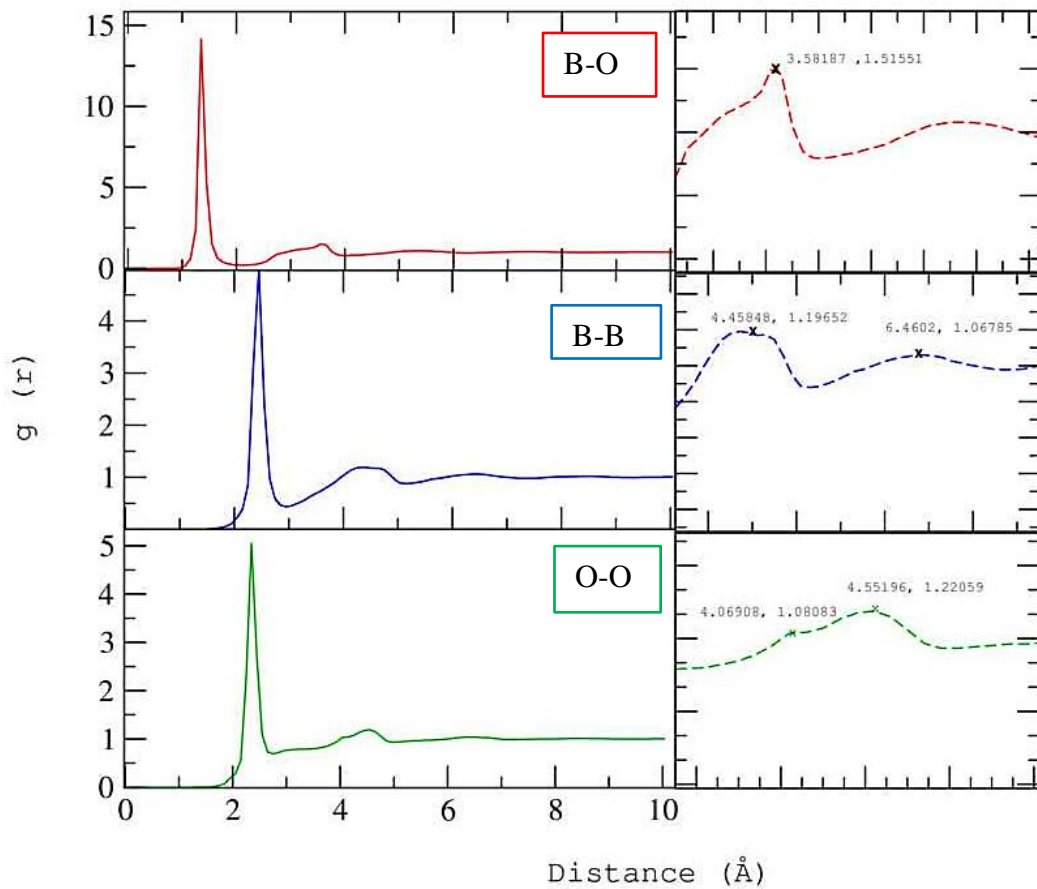


Figure 48 - RDF of A1 System at 300K in the glassy phase with a zoomed section to highlight significant peaks.

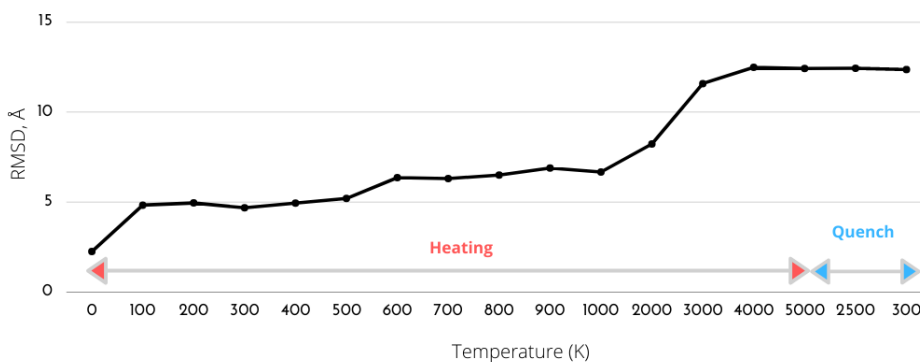
Figure 48 shows the RDFs of the glassy-A1 system. The previous RDF of the molten phase, **figure 44**, showed somewhat broader peaks which have acquired new features in the glassy phase. There are visibly sharper peaks, similar to what was seen within the crystal phase. However, unlike the crystal (**Figure 41**), the glass has a reduced number of peaks. The more distinct peaks are representative of a more ordered system which is expected of glass compared to the molten state. From the O-O RDF, a new peak which was not observed in the molten structure has appeared. After the initial dominant peak at 2.38 Å, there are two peaks at 4.069 and 4.552 Å, the latter of which was also found in the melt. These secondary peaks are associated with O-O separations from a neighbouring BO_4 tetrahedral groups and from next nearest neighbor trigonal BO_3 groups. ⁽¹⁴⁸⁾

These results indicate the possibility of a small amount of boroxol ring present in the amorphous glassy phase. This is also supported by the B_2O_3 data which showed that a very small peak is present at 1.44 Å. The R.I.N.G.S data supports this conclusion with the data shown for the percentage of BO_3 structures present as displayed in **Figure 46**. The comparison of all three phases will be discussed in the following section.

4.5 Comparison of the three B_2O_3 phases

Atomic migration within a simulation can be evaluated using the overall root mean squared deviation (RMSD) of the computed B_2O_3 system, for which the RMSD atomic positions are calculated relative to the original A1 system as reference frame. **Figure**

49 shows the RMSD within the three phases. Notably, the crystalline minimisation shows a value of 2.25 Å when recorded against the unminimized structure. The rest of the values were then compared to the minimised structure. The simulations at temperatures from 4000 - 5000K show the greatest movement with values over 12 Å. Generally, it can be observed that as the temperature increases the RMSD value changes almost linearly. The quenched temperatures also show an overall displacement of over 12 Å, representing movement from the original crystalline phase. The RMSD values, are similar but comparing values between the molten structure (5000K) and the final quenched temperature (300K), the RMSD value is 12.37 Å. This implies only a slight overall displacement of atoms upon quenching, compared to the molten phase.



Temperature	RMSD (Å)
0	2.25
100	4.83
200	4.95
300	4.68
400	4.94
500	5.20
600	6.36
700	6.31
800	6.50
900	6.89
1000	6.67
2000	8.23
3000	11.59
4000	12.49
5000	12.43
2500	12.44
300	12.37

Figure 49 - Effects on RMSD value against changes in temperature. The maximum temperature at 5000K. The blue highlights the quenching temperatures (atom averages / Å)

4.5.1 RDF comparison

Studying the bond angle distribution is one way of characterising the types of coordination within the network. Specifically, the B-O-B and O-B-O angles provide an indication to the BO_4 and BO_3 units.

The radial distribution function allows for an understanding of packing within the system. **Figures 50, 51 and 52** show the RDF of B-B, B-O and O-O respectively of the A1 system across the temperatures, which encompasses the melting and rapid quenching steps. All bonds show that during the initial rise in temperature the crystal exhibits an expected uniform, periodic structure with the presence of the sharp peak. As the temperature rises to the final 5000K, the peaks are broader, indicative of a molten state. The final rapid quench temperatures deliver a return in sharpness - demonstrating a more ordered structure.

Zarzycki *et al.* showed through experimental analysis, that there is a broadening of peaks for the B-O and O-O distribution, in vitreous phases. ^(21,33) This was seen to occur as the temperature is elevated. The results of this research show the same trend.

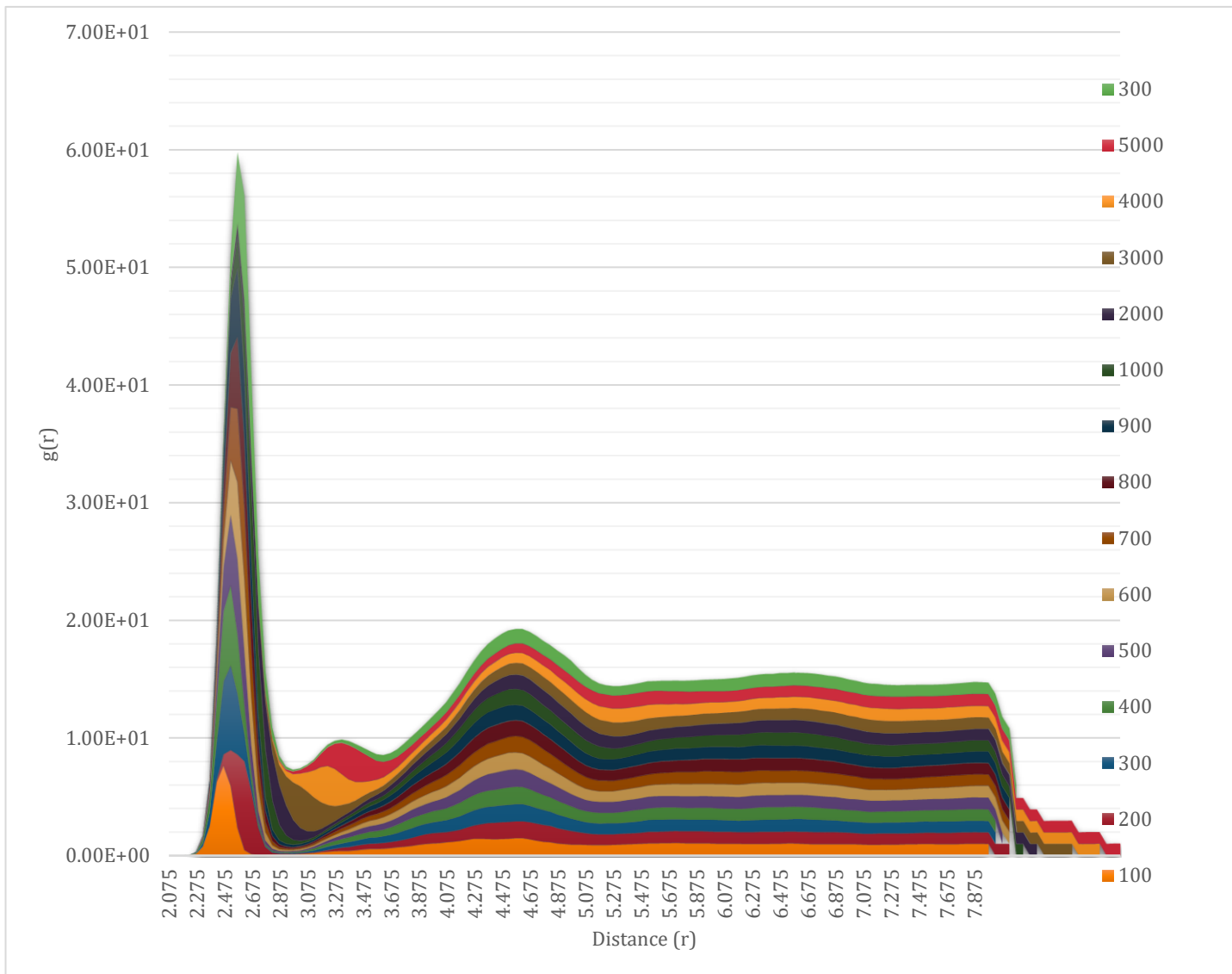


Figure 50 - RDF for BO for all temperatures investigated. The key indicates the temperature of the simulation run in Kelvins.

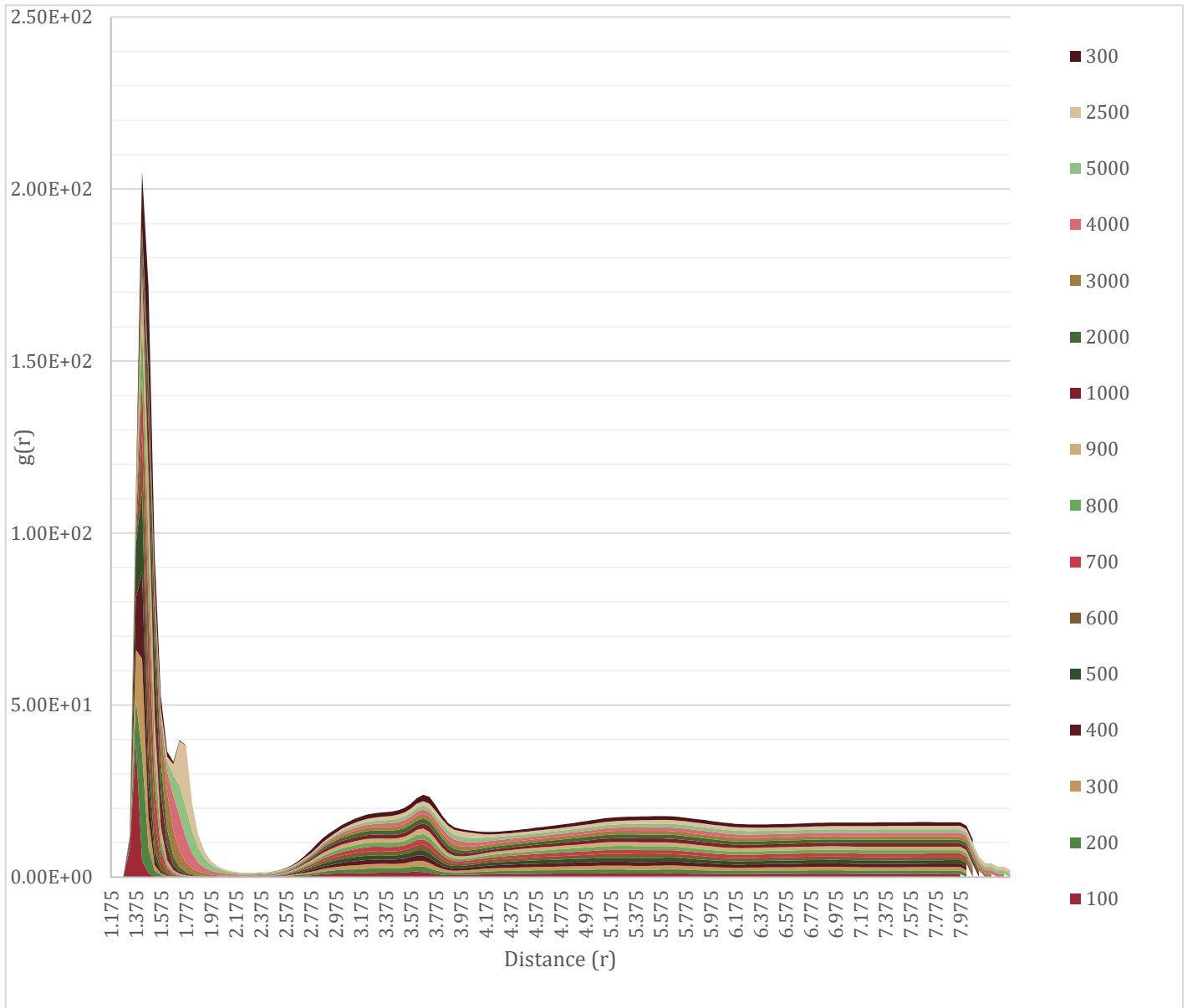


Figure 51 - RDFs for BB for all temperatures investigated.

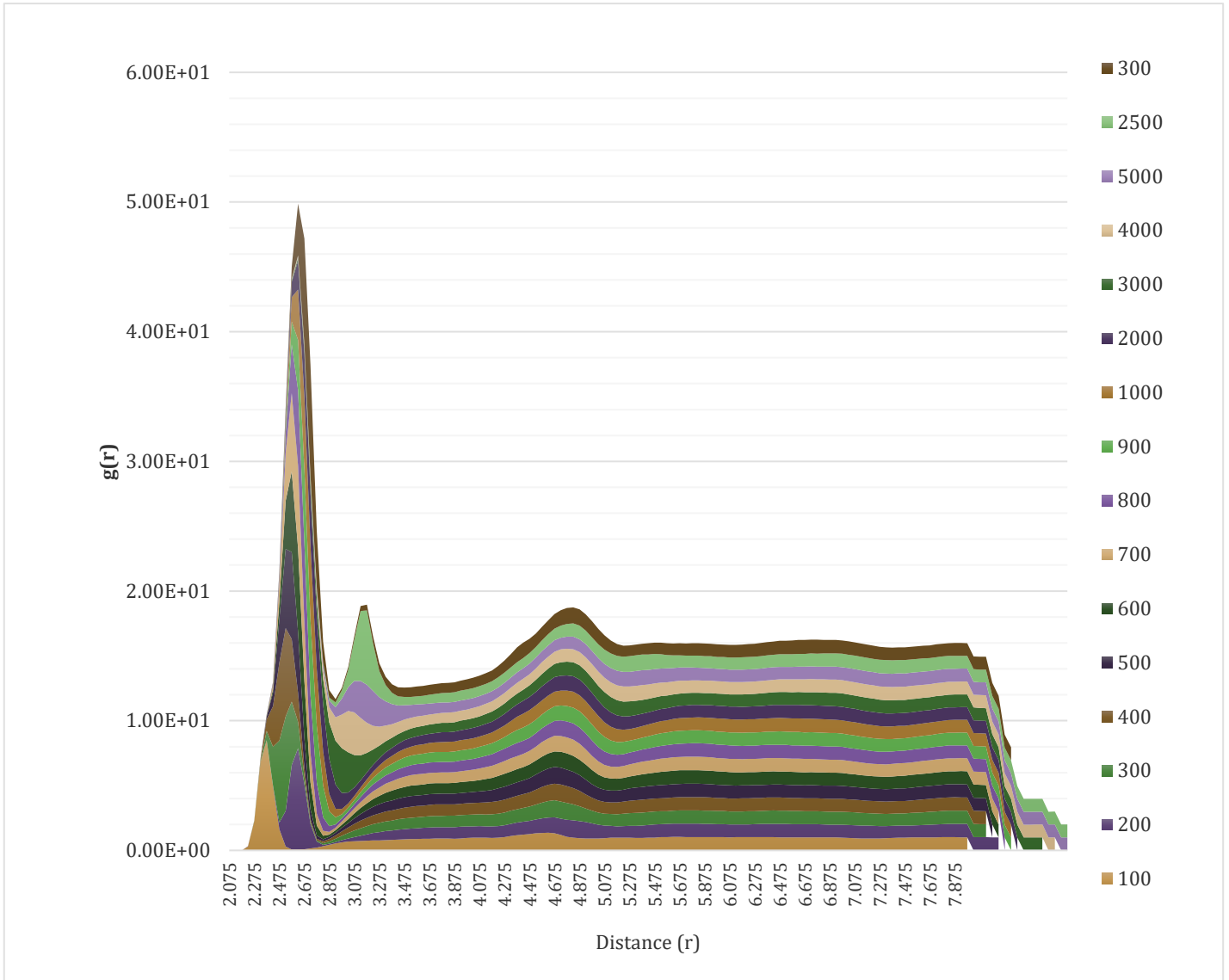


Figure 52 - RDFs for OO for all temperatures investigated. The key indicates the temperature of the simulation run in Kelvins.

4.5.2 Diffusivity analysis

Calculation of diffusivity is important in understanding how the structure and dynamics vary over a wide temperature range. This analysis identifies the rates in which a particle becomes more mobile, changing state because of external variables which in this case is the increase in temperature.

Temperature (K)	D_B ($10^{-9} \text{ m}^2/\text{s}$)	D_O ($10^{-9} \text{ m}^2/\text{s}$)
100	0.0092	0.0131
200	0.0054	0.0124
300	0.0080	0.0160
400	0.0134	0.0258
500	0.0421	0.0660
600	0.1065	0.1475
700	0.0188	0.0329
800	0.0950	0.0198
900	0.0898	0.1276
1000	0.0700	0.1161
2000	0.1319	0.1380
3000	0.2869	0.2459
4000	0.3848	0.3708
5000	0.9927	1.2059
q2500	0.1881	0.1997
q300	0.5173	0.0583

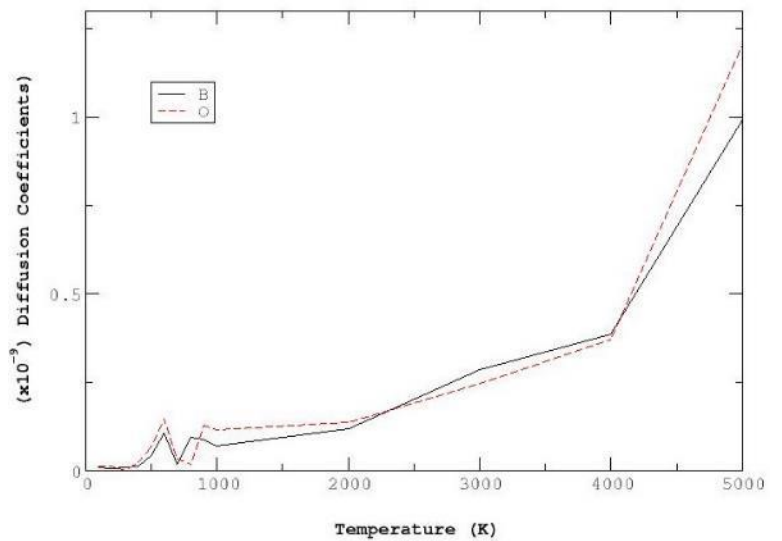


Figure 53 - Diffusion Coefficients for B and O in A1 system. The q2500 and q300 values indicate the quench steps.

As can be seen from **figure 53**, there is an overall increase in the diffusivity with temperature. The largest values being at the highest temperatures, between 4000-5000 K. The plot displays a linear relationship for the heating phases yet as the temperature decreases for the quench stages there is a shift in the trend seen in **Figure**

53. Both atoms follow the same diffusive trends. Though the oxygen atoms have a slightly greater diffusion rate than the boron.

4.6 Chapter Conclusion

Via the MD simulations carried out in this project, a stable crystalline B_2O_3 crystal has been minimised to a stable configuration at 0 K. The crystalline phase displays no boroxol rings and has extensive amounts of BO_3 subunits shown throughout the RDF analysis.

Analysis of the B_2O_3 melt phase revealed the formation of boroxyl rings at various temperatures. The RDF data also showed two distinct peaks at 4.56 and 4.58 Å not visible in the crystalline stage, indicating the increased presence of the boroxol ring. The rings statistics also revealed that the majority of the boron and oxygen atoms were 3 and 2 coordinated respectively. However, a smaller portion, 12.5% (B) and 8.33% (O) are 4 and 3 coordinated. Other rings, such as the 4 and 10-membered rings, were identified.

The quench, glass-forming stage produced similar peaks in the RDF that were seen for boroxol ring presence, 4.069 and 4.552 Å but with more discrete peaks. The RMSD values also revealed a small configuration change in comparison between the final molten temperature at 5000K to this glassy phase quenched back to 300K. The greatest structural deviation was revealed to between the crystalline and molten phase.

5 BORON TRIOXIDE : LARGER SIMULATION CELLS

5.1 Abstract

Studying larger systems provides further and more detailed information on their physical and chemical characteristics and can give a better representation of the real system. Where previous research has been only able to undertake simulations of around 500 atoms, we have now been able to expand the system size to over 30,000 atoms. This has resulted in a more accurate understanding of long-range order of the B_2O_3 . Once again as the previous chapter has shown, we will find that the boron atoms are 3-coordinated, and the oxygen atoms primarily 2-coordinated. We have also been able to show that the boroxol rings have a smaller presence within the glassy network.

In the two systems sizes chosen in this study, see **section 5.3** (B1 and C1), the proportions of boron atoms with a coordination number of 3 were 85.3% and 77.2%, respectively, with the remaining 14.7% and 22.8% having a coordination number of 4. Having a simulation with a greater number of atoms showed that the results were also more closely associated with the hypothesis of more BO_3 present in pure B_2O_3 , confirmed by the angular data also showed the smaller (12,960) and larger systems (30,720) system having average B-O-B angular value of 118° and $> 138^\circ$ respectively.

5.2 Aims and Introduction

One of the key areas of this research has been the investigation of the ring subunits, shown in Chapter 3 to be an important structural feature of the B_2O_3 system network. This chapter will draw comparisons of two systems which vary in size only and see the effects they have on the portion of the boroxol ring, which is important as it helps understand further details of the real system by capturing potentially more accurate effects in the glassy phase by comparing the short, medium and long-range order using the same conditions of temperature and ensemble.

We note that simulation box sizes are required to be larger than the correlation length of the system. Furthermore, the simulations must have a suitable simulation time to ensure all properties of interest are adequately captured, allowing a sample of the statistical properties to be obtained reliably. ⁽¹³⁹⁾

5.3 Computational Details

In the following section, the effects of the simulation box size were investigated through two different system sizes, the first being a medium-sized simulation which contains 12,960 atoms and the second system containing 30,720 atoms. This compares to the 480 atoms seen in the A1 system. For both these systems, the DL_POLY graphical user interface (GUI) programme was used to create the supercells.

Once again, the temperature limits were the same for all simulations, including the highest temperature of 5000K and the final quenching temperature at 300K, this is displayed in **Table 10**. Both systems were tested with the potentials investigated in this research. The simulations were again carried out using DL_POLY.

Table 10 - B1 and C1 system computational information

Simulation system	Potential Used	Heating Temperature (K)	Quenching Temperature (K)	Simulation Time (ns)
B1	2	5000	300	2
B1	3	5000	300	2
C1	2	5000	300	2
C1	3	5000	300	2

Comparisons of both systems examined the structural data including bond length and polyhedra data. The analysis was carried out using the R.I.N.Gs code to investigate the systems' data as the number of atoms increases. ⁽¹⁴⁵⁾ The analysis also draws comparisons to data from the A1 system in the previous chapter, to see if there are any key structures and mechanical (torsional) data found.

The difference in the energy and volume between the crystal, melted and glassy structures of B₂O₃ is an interesting topic. Varying the temperature has a direct effect on these two parameters, but an observation of this is inaccessible when using the NVT ensemble. Therefore, a series of simulations were carried out to investigate the changes to volume and energy using the NPT ensemble.

5.4 Results and Discussion

5.4.1 B1 System

The B1 system contains 12960 atoms, with 5184 boron and 7776 oxygen atoms, respectively. Our investigation led to the identification once again of key structures within the network of crystal, molten and glass phase. A comparison was also made with the smaller A1 system.

The B1 system, **Figure 54**, has been calculated to have 16227 bonds and 5193 polyhedra in this system using the VESTA programme. ⁽¹⁵⁹⁾

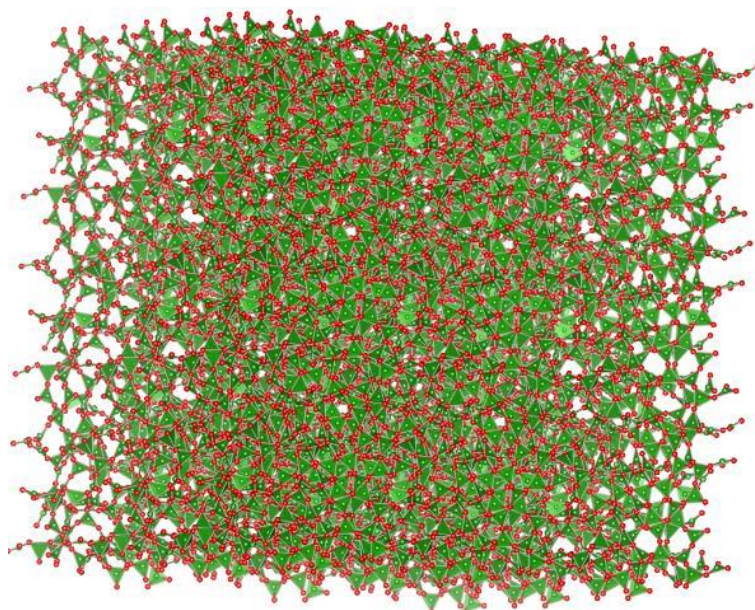


Figure 54 – Polyhedra graphical representation of the B1 system visualised in the VESTA programme. The red are the oxygen atoms with the green indicating the polyhedra surrounding the boron atom.

The polyhedra analysis provides a great insight into bond and angular information in the BO_3 subunits. The average B – O bond length in the crystalline phase is recorded

as 1.34 Å, with an indication of a distortion index of 0.014 Å. The effective coordination number is calculated to be 3 corresponding to the planar trigonal group.

5.4.2 C1 System

Using the DL_POLY GUI, a 2x2x2 supercell was created by expanding by 2 on each axis of the cell (x, y, z), increasing the total number of atoms to 30,720, the purpose of which was to examine whether the bonding observed is system size-dependent and whether this would affect the dispersion of B and O atoms within the molten and glassy phases. Previous researchers investigating pure B₂O₃ were unable to visualise the system at this scale, but as computational resources have improved, larger systems can now be simulated. The new system, denoted C1 is displayed in

Figure 55. The C1 system now has 12288 oxygens and 18432 boron atoms. As seen in

Figure 55 the crystalline structure shows a prevalence of 3-fold B as seen with A1 system.

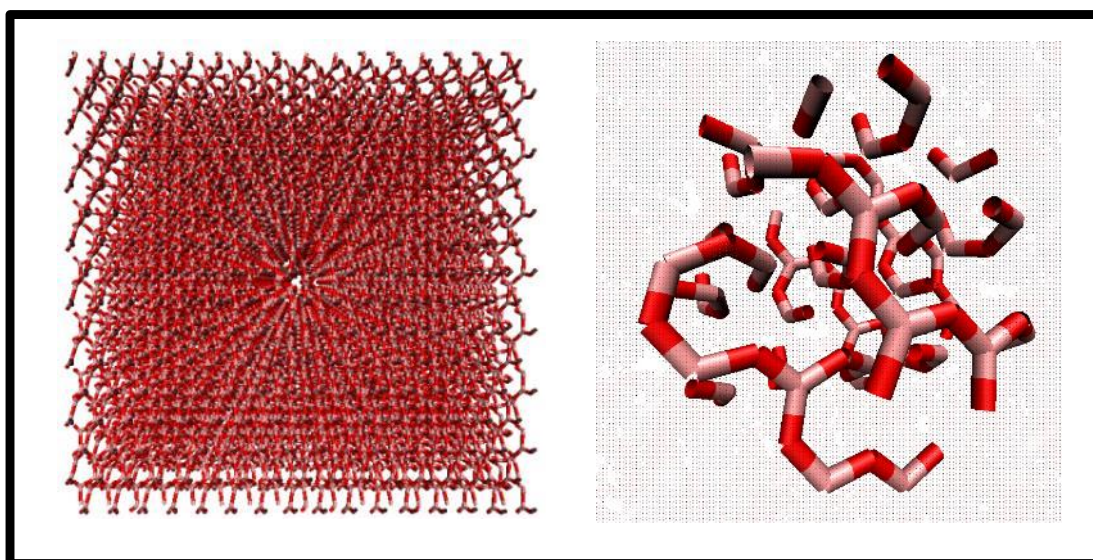


Figure 55 – 2x2x2 B₂O₃ supercell, C1.

The C1 system presented in

Figure 55 has 12288 polyhedra with 36864 bonds. The number of polyhedra in this system matches the number of boron atoms within the system. The polyhedra show that the average B-O bond is 1.50 Å with a distortion index of just 0.020 Å.

5.4.3 Bond and ring analysis

Previously, the A1 system was investigated to identify key groups and ring structures, especially BO₃ and BO₄ subunits. Moreover, the frequency of these groups is particularly important to detail the crystal structure network and its reconstruction during the phase changes.

The R.I.N.G.S code was once again utilised to identify the angle data within the system and the most prevalent structures. **Figure 56** shows the O-B-O angle which is that associated with both the trigonal planar groups and the boroxol rings.

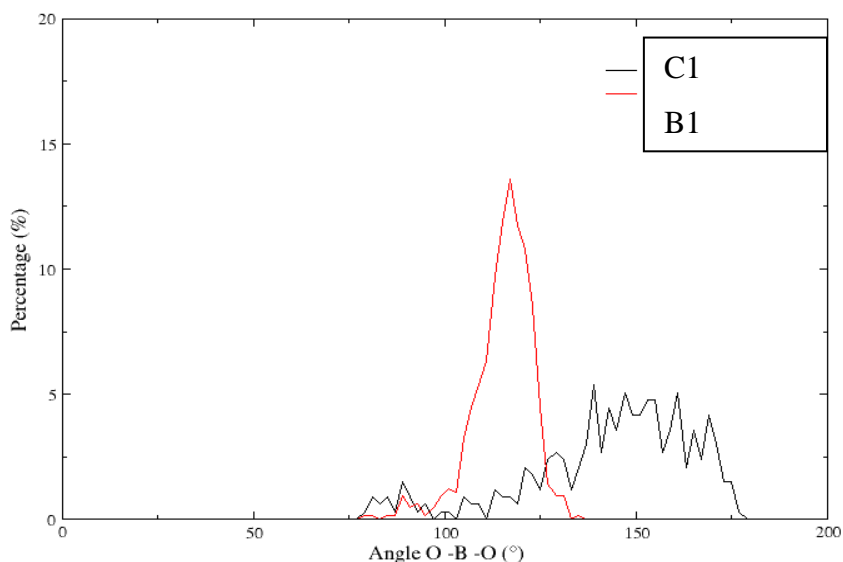


Figure 56 - Distribution of O-B-O angle in the B1 (red line) and C1 systems (black line).

In particular it shows the variation in the O-B-O angle between the two systems in question as a snapshot at the end of the simulation. We observe that for the larger system, the data become more dispersed than seen with the B1 system, which shows the importance of system size. While the B1 system gives a mode of $\sim 118^\circ$ which is a value approximating that closest with boroxol ring data.

Using the identical cut off ranges of 3.10 \AA (as seen with the A1 system) the rings data were calculated. The data for the proportions of boron atoms with coordination of 3, was 85.3% and 77.2% for the B1 and C1 systems respectively, with the remainder 14.7% and 22.8% having a coordination number of 4. The oxygen atoms had a larger

portion of atoms with a coordination of 2, 89.4% and 80.3%. The remainder were in the coordination of 3.

5.5 Chapter Conclusions

Executing the different simulation cell sizes with varying number of atoms, the data revealed a greater dispersion for bonding information in the larger cells, as compared to the smaller cell. The average B-O bond length was 1.34 Å and 1.50 Å for B1 and C1 crystalline systems, respectively. The angular data also showed the B1 system having average B-O-B angular value of 118° whereas in the C1 system a wider spread is observed, with a mode value far greater at 138°. The data is interesting and indicates that for more accurate data larger systems are preferred, particularly to simulate accurately the data for this type of system in terms of volume and energetics.

The ring analysis showed that all three systems (A1, B1 and C1) follow the same structural trend where a large majority of the boron atoms are 3-coordinated, and the oxygen atoms primarily 2-coordinated. This indicates that identifying the presence of boroxol rings is challenging, and hard to distinguish from the high concentration of BO₃ units within the system. It is essential to note that changes in system size do indeed have an impact on bond length and angles, but despite a possible indication of boroxol ring formation, these changes seem to be less significant than expected. This indicates that although there maybe complexes involving BO₄ group, the prominent moieties are BO₃.

PART II

The following chapters contain the methodology, results and discussions concerning the DFT simulations of B_2O_3 and other borate crystals within the scope of this project.

6 METHODOLOGY: ELECTRONIC STRUCTURE METHODS

6.1 Abstract

The second methodology utilised within this thesis is Density Functional Theory (DFT). This method has been incorporated within many studies as it provides a technique for modelling the electronic structure of ground states at a reasonable level of accuracy. For this portion of studies, the Vienna *ab initio* Simulation Package (VASP) was used. This package has been used extensively in the solid-state modelling community and has based on these previous studies been selected for studying the electronic structure of B₂O₃-based systems here.

The following research investigates systems of B₂O₃, both pure and that which contain other mixed alkali ions. The purpose was to consider the structural and electronic properties of these systems and draw a comparison on the effects these glass modifiers have.

6.2 Schrödinger Equation

Electronic structure calculations work by modelling the nucleus and electrons separately. The time-independent Schrödinger equation is a mathematical expression introduced by Erwin Schrödinger in 1926 allowing a specific property (such as energy) for a given system to be determined. For such a system containing M nuclei and N electrons, the interaction of $M+N$ particles is described by

$$\hat{H}\psi(\mathbf{r}, \mathbf{R}) = E\psi(\mathbf{r}, \mathbf{R}) \quad (23)$$

In this equation, the operator, \hat{H} , is the Hamiltonian. Alongside this, $\psi(\mathbf{r}, \mathbf{R})$ is the electron wavefunction and corresponding electron coordinates. Lastly, E is the total energy of the system. This equation works as the operator, when applied to the wavefunction, returns a value which is the wavenumber multiplied by the energy of the system.

To understand the Hamiltonian, we can isolate components that this operator governs.

$$\hat{H} = \hat{T}_e + \hat{T}_N + \hat{V}_{eN} + \hat{V}_{ee} + \hat{V}_{NN} \quad (24)$$

The \hat{T}_e and \hat{T}_N are values that correspond to the kinetic energy of the electron and that of the nuclei within a system. \hat{V}_{eN} is the Coulomb attraction between electrons (e) and nuclei (N), \hat{V}_{ee} the Coulomb repulsion between electrons, and \hat{V}_{NN} the Coulomb repulsion between nuclei. This gives the non-relativistic time-independent Schrödinger equation.

However, this expression is not soluble with current mathematical techniques due to it being dependent on two sets of related variables and requiring the calculation of the e-e interaction. Hence, a separation of terms based on relative masses is employed to simplify the problem.

6.2.1 Born-Oppenheimer Approximation

There is an assumption that the motion of N and e can be separated, as the 1830 times larger mass of the nuclei slows its movement to make it almost negligible in comparison to the electrons. In this case, the kinetic energy of the nuclei is zero alongside the corresponding potential energy which also insignificant. This assumption is known as the Born-Oppenheimer (hereby noted as BOpp) approximation. One assumes that the electrons are constantly in their ground state which in turn provides a potential energy surface – the potential energy of the system is a function of the atomic position. To solve the Schrödinger equation, the \hat{H} for the electrons can be defined through the wavefunction ψ_{elec} and the electronic E_{elec} .

$$\psi(e_i N_i) = \phi(e_i, \{N_i\}) \chi(N_i) \quad (25)$$

The BOpp approximation is incorporated here to describe the nuclear motion to be negligible. However, the nuclei positions, N_i , can still be determined through the electronic wavefunction, $\phi(e_i, \{N_i\})$.

The electronic wavefunction represents the number of possible electronic states available for the fixed nuclei positions. The nuclear function, $\chi(N_i)$, is added to solve

the rotational vibrational issue which occurs when the nuclei are presented with an electronic potential energy surface. ⁽¹⁷⁵⁾

As mentioned previously, the Schrödinger's equation is very difficult to solve for multi-electron systems. Therefore, approximate solutions are used to solve the equation.

⁽¹⁷⁵⁾

6.3 Density Functional Theory

DFT focusses on calculating the electron density of the system, from which molecular properties can be identified. These include; the energy, the magnetic and electric properties and even the vibrational frequencies.

The essence of DFT is relating the total energy of a system (E_{tot}) in terms of kinetic (E_{kin}), potential (E_V), Hartree (E_{har}) and exchange-correlation (E_{xc}). The interacting electrons are acting on the potential field, $v(r)$ for the nuclei.

$$\mathbf{E}_{tot} = \mathbf{E}_{kin} + \mathbf{E}_V + \mathbf{E}_{har} + \mathbf{E}_{xc} \quad (66)$$

For solid state research, DFT has been proven to be largely popular to study a large number of atoms but not large in relation to MD simulations.

The basis for the theory comes from the Hohenberg-Kohn Theorems which will be discussed later. However, with almost all solid state and quantum approached, the aim is to solve the time-independent Schrödinger equation. ⁽¹⁷⁵⁾

6.3.1 Hohenberg-Kohn Theorem

The two main theorems that are the basis of DFT are the Hohenberg-Kohn theorems.

The first theorem states that the ground state electron density, $\rho(\mathbf{r})$, of a system provides a unique solution to the Hamiltonian, and all properties of this multi-electron system and its total energy can be exactly calculated from its ground state.

The second theorem states that a universal functional $F[\rho(\mathbf{r})]$ exists such that the total energy of system ($E[\rho(\mathbf{r})]$) can be calculated from the corresponding $\rho(\mathbf{r})$. $F[\rho(\mathbf{r})]$ corresponds to the inter-electron Coulombic repulsive forces and the exchange-correlation and kinetic energy. The V_{ext} represents the electrons interacting within an external potential. The final term, $\langle \Psi | \hat{F} + V_{ext} | \Psi \rangle$, considers all the ground state wavefunctions.

$$E[\rho(\mathbf{r})] = F[\rho(\mathbf{r})] + \int \rho(\mathbf{r})V_{ext}(\mathbf{r})d\mathbf{r} = \langle \Psi | \hat{F} + V_{ext} | \Psi \rangle \quad (27)$$

To solve this equation, the variational principle is used to minimize $E[\rho(\mathbf{r})]$ to obtain the ground state energy. However, despite these efforts, it remains challenging to obtain the exact form of $F[\rho(\mathbf{r})]$ due to the solving of the Hamiltonian e-e term. A year after these theorems were presented, Kohn and Sham presented a technique by which to approximate $F[\rho(\mathbf{r})]$.

6.3.2 Kohn-Sham Theory

It is important to be able to carry out DFT calculations without forgoing accuracy in results. In this theory, a fictional system is considered containing non-interacting electrons. The fictional system has identical positions and the density to a “real” system with interacting electrons. The reasoning comes from being able to split specific energy terms that can relate to different components. Hence, providing a more solvable calculation due to the kinetic energy of non-interacting electrons being known:

$$E[\mathbf{n}(\mathbf{r})] = E_k[\mathbf{n}(\mathbf{r})] + E_v[\mathbf{n}(\mathbf{r})] + E_H[\mathbf{n}(\mathbf{r})] + E_{xc}[\mathbf{n}(\mathbf{r})] \quad (7)$$

Where the total energy is split into the following:

1. The non-interacting electrons Kohn-Sham kinetic energy of the fictional system ($E_k[\rho(\mathbf{r})]$)
2. The potential energy ($E_v[\mathbf{n}(\mathbf{r})]$)
3. The Hartree energy ($E_H[\mathbf{n}(\mathbf{r})]$) – relating to the Coulombic repulsive forces between electrons
4. The Exchange-Correlation energy ($E_{xc}[\mathbf{n}(\mathbf{r})]$) – a corrective term to the kinetic energy and non-classical inter-electron repulsion.

The $E_{xc}[\mathbf{n}(\mathbf{r})]$ relates to an attempt to correct the kinetic energy term but also collates the electronic repulsion because of exchange-correlation. Due to the consideration of a non-interacting system, the wavefunction can now be expressed through a Slater determinant. ⁽¹⁷⁵⁾

6.3.3 Exchange-Correlation

The external potential, $E_{xc}[n(\mathbf{r})]$, is the difference between the functional term, $F[\rho(\mathbf{r})]$, and the remaining energy terms. An example of the $E_{xc}[n(\mathbf{r})]$ being calculated is for uniform electron gas. In this case, through simulations using Monte Carlo, the functional has been calculated analytically. When the functional term is unknown, the exchange term will be approximated. There are numerous ways in which this approximation can be determined. These terms arise from the instantaneous coulombic repulsion force that occurs between electrons and due to the electronic wavefunctions asymmetry. Some empirical parameters can be introduced in order to improve performance.

6.3.4 Local Density Approximation

The Local Density Approximation (LDA) is a simple way in which the $E_{xc}[n(\mathbf{r})]$ can be approximated. It is carried out through attaining the density for every unit of volume of a homogenous electron gas (jellium) from the electron density. This is done at specific points, r , and therefore estimates a local value of the density.

$$E_{XC} = \int \epsilon_{xc}(\rho(\mathbf{r}))\rho(\mathbf{r})d \mathbf{r} \quad (29)$$

The $E_{xc}[n(\mathbf{r})]$ is carried out numerically on a grid. LDA for many solid-state systems, especially metals and some semiconductors, provides an adequate result.

It has proven to be accurate at calculating ground state properties. However, the approximation has limitations in calculating binding energies, van der Waals interactions and band gaps.

6.3.5 General Gradient Approximation

To improve the shortcomings of LDA, gradient corrections were introduced for each particle in the jellium above. This is expressed in the GGA equation. ⁽¹⁵⁰⁾

$$E_x^{GGA}[\rho] = \int \rho(\mathbf{r}) \epsilon_x^{GGA}(\rho(\mathbf{r}), \nabla\rho(\mathbf{r})) d\mathbf{r} \quad (30)$$

This method not only considers the exchange-correlation terms, just like LDA does, but GGA has also shown improvement in the calculation of weak inter-atomic bonding, bond lengths/angles, and binding energies. ⁽¹⁵¹⁾

This project has hence chosen GGA over LDA and is implemented with Perdew-Burke-Ernzerhof (PBE) functionals.

6.4 Analysis of DFT Optimised Structures

To analyse the results produced from DFT calculations, many tools utilised in the upcoming result chapters. This includes Thermal stress, electronic structure, elastic constants, and band structure to name a few. This section will discuss the background to these methods.

6.4.1 Band Structure

As mentioned in section 2.4, periodic boundary conditions apply.

Electronic properties describe the physical characteristics of a material in terms of its charge carriers and its response to electric and magnetic fields. It is apparent that for every individual material, the complexity of charge transfer and transport varies. It is interesting to investigate such intrinsic properties as there is a great influence on reactivity and conductivity. ⁽¹⁵²⁾

Therefore, the study of the band structure is interesting. This property provides an understanding of electronic movement and conducting/semiconducting/insulator behaviours are noted.

6.4.2 Density of states

To understand the “*packing*” of quantum states within the system in question, the density of states (DOS) can be investigated. This can provide further information on the optical properties of a material, particularly to determine the semi-conducting abilities of a system. When systems are periodic and contain a substantial number of atoms, the energy levels present are close. When this occurs, the energy level bands are continuous, and the DOS can help plot these bands.

Electrons in the outer shell of an atom can move freely within any given metal solid due to the nuclei hold the outer electron by weak electric forces. According to the

free-electron theory these atoms are free to delocalise through the solid. It can then be considered as a finite potential well, with the electrons have zero-potential energy. This value increases as you go further out to the edges of the atom.

It is apparent from the Pauli Exclusion Principle that only two electrons can occupy an orbital and that all the electrons within a system have a unique set of quantum numbers. The mathematical function, DOS, gives the distribution of possible quantum states that the electrons can take per unit volume, per unit energy.

The investigation of the number of states, $N(E)$, between E_1 and E_2 for example, the following equation is implemented:

$$N(E) = \int_{E_1}^{E_2} g(E) dE \quad (31)$$

The value for is obtained from DOS calculations and helps estimate the probable number of states occupied by electrons. The integration then provides an easy evaluation of possible quantum states through graphical representation, with the gradient indicating the number of states.

6.4.3 Thermal Stress / Temperature Stress Point

As temperature increases, solid materials tend to expand. This occurs due to an increase in kinetic energy within a system as a product of the rise in heat. The molecules start to vibrate and the once, well-defined shape, start to change as they collide and move away from each other, and expansion occurs.

With these volumetric changes, the level of what is known as, thermal stress, is seen to rise. Thermal Stress primarily affects the structure's strength and is a factor that can identify where deformation can occur. When the production of materials, such as glass, the temperature stress point can help classify limits – saving both costs and time.

6.4.4 Pulay Stress

An optimisation not bound just to the ionic position, but for the other cell parameters can produce this stress. The Pulay stress is an outcome of the incomplete planewaves basis set in relation to the changes in the systems volume. This error causes an underestimation of a system equilibrated volume during this process. To reduce this, the energy cut-off can be reduced or be kept at a fixed rate. To carry this out can be computationally expensive. However, if the cut-off can converge the stress tensor this will be appropriate. ⁽¹⁵³⁾

6.5 Elastic/Mechanical Properties

Investigating elastic properties is useful for many factors. In the case of glass, brittleness of the material is essential for commercial use. Understanding the breaking and molecular tensile strength can help the production phase by looking at mixed alkali ion contents and introducing this in process. As mentioned previously, glass is vastly used across fields and its malleability is a critical property to consider.

To understand the effects of pressure, stress and strain, there are many measurements that can be carried out. The following sections will outline some of these tools and the ones that have been carried out in this research project.

To investigate crystal strength, the elastic constant provides information on a materials elastic limit which is the point at which the material is unable to return to its original shape. Hence, this constant is a measure of how well a material responds to stress. Clearly, when the strain is applied, it is in all direction to which stress is impacted at certain points also making both a second-order tensor. Thus, the elastic constant is a fourth-order tensor. The equation below identifies the way stress is investigated.

$$\sigma_{ij} = \sum c_{ijkl} \epsilon_{kl} \quad (32)$$

The strain, ϵ , and stress, σ , are dependent on the symmetry of the crystals. The various elastic constants, c_{ijkl} , relate stress and strain along an axis or across a face. From the elastic constants, one is then able to identify the shear modulus (G) and Bulk modulus.

6.5.1 Bulk Modulus

The study of compression is useful for understanding certain properties of a material. Bulk modulus, B, is a measure of the compressibility when under a specific amount of external pressure. B is essentially the ratio which compares the change in the pressure of the system to the volume.

$$B = -V \left(\frac{\partial P}{\partial V} \right)_T \quad (33)$$

The calculation is carried out by distorting the unit cell in all three dimensions whilst collecting the energy as a function of volume. A higher B value indicates less compressibility and the material requiring higher pressures to reduce its volume.

Via the calculations for the elastic constants above, it is possible to mathematically derive Bulk Modulus values. Through the Voigt formulism, the bulk modulus can be expressed as follows:

$$B = (C_{11} + 2C_{12})/3 \quad (34)$$

6.5.2 Young's Modulus/Elastic Constant

To further understand how elongation and compression work for more linear objects (such as glass fibres and columns), we calculate a parameter called Young's Modulus, YM. This measurement helps with understanding how far an object can be stretched and connecting the effects of both stress and strain.

$$YM = \frac{\text{Stress}}{\text{Strain}} = \frac{P}{\Delta L/L} \quad (35)$$

The elastic constants produced is within a matrix, that contains the relation between the diagonal stress and strain tensor.

6.5.3 Dielectric Function

The dielectric function is a ratio which observes the permittivity of a structure against the permittivity of free space. It, therefore, is a measure of a response/reaction towards the implementation of an external force on a system. Sometimes, systems can be held within an electronic charge for a specific length of time. The materials that possess a high dielectric constant value are convenient for specific industries, such as the manufacturing of high value capacitors.

As the dielectric function is a measure of “*stretchy atoms/molecules*” and how degradable a system is within an electric field, this is important for the purpose of this study. In VASP, this calculation is carried out through the density functional perturbation theory and by setting the LEPSILON tag as “true” and is the recommending setting to determine the effective dielectric and piezoelectric tensors.

6.6 VASP

For all DFT calculation in this portion of the thesis, the Vienna *ab initio* simulation package (VASP) was used. The program uses each planewave basis set to describe valence electrons within a system. ⁽¹⁵⁵⁾

The simulation runs utilised the PBEsol functional. This was since the PBE functional is used most commonly for solid-state calculations as it utilises both density and its gradient at each point. The modified PBEsol functional is a newer, updated version which reduces overestimation of lattice constants by a factor of almost 4 in mean absolute error. ^(155,156)

6.7 Polyhedra Analysis

The polyhedra are geometric structures of a solid, described through three dimensional flat faces, edges, and vertices. These units provide a comprehensive description usually used for intermetallic compounds and minerals. The VESTA program assigns polyhedra by firstly identifying central atoms, in this case, it will be the Na and B atoms. Next bonds between this assigned centre and apex molecules are displayed such that they fit the criteria of faces and lengths to give them the classified name (tetrahedron, pentahedron etc.). Through this assignment in structure, additional data can be attained in regards to the coordination, volume, distortion and variances. ^(157–159)

7 ELECTRONIC CLASSIFICATION OF B_2O_3 CRYSTALS

7.1 Abstract

As dynamic properties have already been investigated in the first part of this thesis, the aim is now to characterise and collate data relating to other structural and electronic data. We noted from the MD simulations that as the crystal contained BO_3 subunits from the starting material, this continued through the production stages into the liquid and amorphous structures and formation of BO_4 is still sparse. Understanding the nature of the bonding in the crystalline forms is therefore of considerable interest.

The presence of Caesium changes the average B-O bond length to 1.355 Å and average B-O-B angle to 123.5°. Our simulations shows that although proportionally we would expect similar structural information for pure B_2O_3 , the size of the Caesium atom effects the occupancy of the boron and oxygen in the network, creating less dense system (2.4% decrease in $Cs_2O(B_2O_3)_9$) and more porous crystalline network (20.92% increase in porosity in $Cs_2O(B_2O_3)_9$).

7.2 Aims and Introduction

To fully understand the features of a pure B_2O_3 system, the electronic properties were investigated using the DFT techniques available in VASP code. There have been relatively few studies investigating the complexity of the structure of B_2O_3 and the subtle changes to the crystal network through the addition of other oxides. ^(168,169,173)

As mentioned previously, in **Section 6.6**, the VASP code utilises DFT methods for calculations which provide detailed models of the electronic properties of the material in question. The following section presents the results of our calculations. It also outlines the connections between structure and its related mechanical and electronic properties.

Alongside the DFT study on B_2O_3 , this chapter also investigates the addition of caesium oxide within the crystal structure. The ratio within the mixed system crystal is 1:9 of the caesium oxide to boron trioxide respectively, $Cs_2O(B_2O_3)_9$. This ratio was selected, such that the structure could resemble pure B_2O_3 structure but at the same time, an investigation of the influence of Cs_2O on B_2O_3 structure could be performed. Factors including pressure effects and material porosity are investigated and also compared between these two crystals.

7.3 Computational Details

The files containing the starting position for the two crystals studied in this chapter were obtained from the Inorganic Crystal Structure Database (ICSD) and the Crystallography Open Database (COD). The B_4O_6 crystal structure utilised in the following DFT calculations was obtained from experimental data where the crystal was under the pressure of 0.3 - 46 GPa at room temperature (ICSD code: 24711).⁽¹⁶⁰⁾

The $Cs_2O(B_2O_3)_9$ structure employed had been obtained from high-resolution powder diffraction and refined using the Rietveld technique.⁽¹⁶¹⁾

As noted, the calculations in this chapter used the VASP code and all crystals were optimised using the following option in the programs input file (INCAR). The conjugate gradient algorithm was selected and the exchange-correlation functional used in this research was PBEsol which is the Perdew-Burke-Ernzerhof version revised for solids.

(145)

After convergence testing of the cut-off energies for the planewave basis set, the value was set at 700 eV for both crystals. A 7x7x7 Monkhorst-Pack Γ -centred k-point grid was used for all calculations. Electronic convergence and ionic convergence criteria were chosen as 10^{-5} eV and 10^{-3} eV/Å.

For the optimised structure we calculated a range of properties as discussed in this chapter.

For the dielectric tensor calculations, we calculate both the static and high frequency values, using the standard procedures available in the VASP code.

7.4 Results and Discussion

7.4.1 B₂O₃

Large systems of pure B₂O₃, as seen in the A1, B1 and C1 systems, are computationally expensive to investigate. Hence, in this section the unit cell of the crystal form of B₂O₃ containing 10 atoms, hereby known as the D1 system, is investigated with the aim of studying the electronic, mechanical, and elastic properties. This simulation cell has a molecular formula of B₄O₆ as shown in **Figure 57**. In both the D1 system and Cs₂O(B₂O₃)₉ crystals, the bond angle and lengths were investigated after geometry optimisation

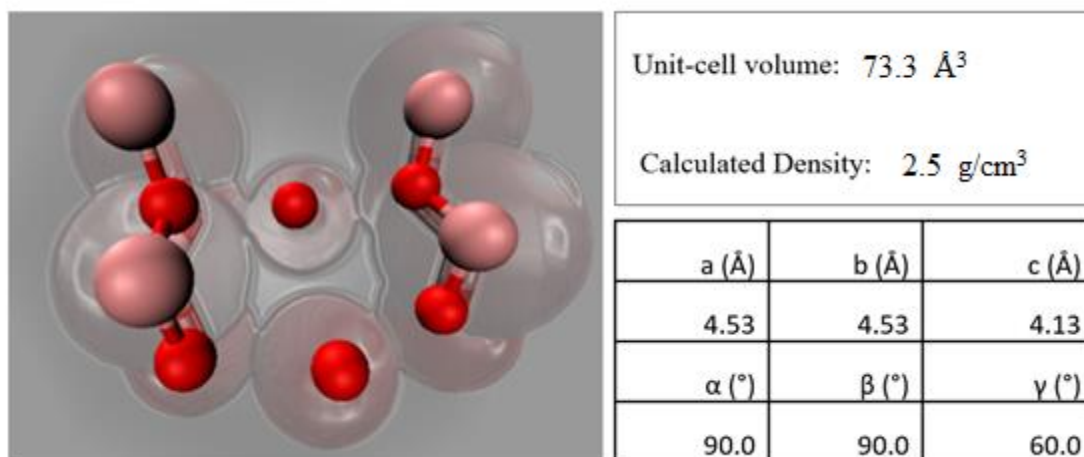


Figure 57- Calculated Structure of calculated crystal B₄O₆

The optimised experimental D1 Crystal, **Figure 57**, has a space group of P1 and has a B-O bond length of 1.506 Å, B-B distance of 2.53 Å and an O-O bond distance of 2.38 Å. Other structural properties include a density of 2.51 g/cm³ and a unit-cell volume of 73 Å³. The density is close to the experimental value of, 2.55 g/cm³. This experimental value was for a crystalline structure at room temperature with structural information most aligned with our computational results.⁽¹⁶²⁾ We note that all DFT simulations are carried out at zero Kelvin in contrast to the higher temperatures seen in MD simulations. Overall, however, there is good agreement between the calculations and the experimental data.

7.4.2 Caesium Enneaborate. Crystal, $\text{Cs}_2\text{O}(\text{B}_2\text{O}_3)_9$

The caesium borate crystal, $\text{Cs}_2\text{O}(\text{B}_2\text{O}_3)_9$, contains 172 atoms with 46 polyhedra. The polyhedra present in the system are highlighted in **Figure 58**. As mentioned previously, the chosen ratio of 9:1 (B_2O_3 : Cs_2O) allows an interesting comparison of the BO_3 groups with those in pure B_2O_3 . The structure has two twin interlocking B_2O_3 networks and due to the ratio in which B_2O_3 is prevalent within this crystal, a hypothesis would be similar structural relationships as pure B_2O_3 would be observed.

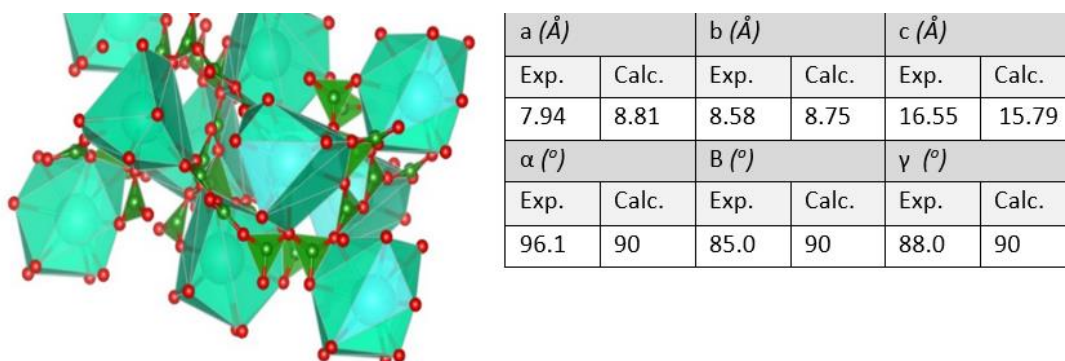


Figure 58 - Calculated Polyhedral representation of the $\text{Cs}_2\text{O}(\text{B}_2\text{O}_3)_9$ crystal. Cs is in centre of large polyhedra with the red spheres representing O and B in the centre of small polyhedra. Experimental data represented by (exp.)⁽¹⁶²⁾

The $\text{Cs}_2\text{O}(\text{B}_2\text{O}_3)_9$ crystal (**Figure 58**) has a space group of $P222_1$, and an orthorhombic cell. Hence, it is seen that on adding Cs_2O to B_2O_3 there is a transition from triclinic to orthorhombic cell structure. The addition of Cs_2O also increases the voids within the crystal as compared to B_2O_3 , resulting in a less dense material. The calculated density of $\text{Cs}_2\text{O}(\text{B}_2\text{O}_3)_9$ is 2.45 g/cm^3 as compared to B_2O_3 2.51 g/cm^3 . This is a 2.4% decrease from the pure B_2O_3 simulation, and from the experimental cell parameters we can see

a 10% difference between the data calculated in this research against previous experimental data.

Much like the B_2O_3 crystal, the $Cs_2O(B_2O_3)_9$ crystal is similar to the measured value of 2.485 g/cm^3 . In terms of density, although simulation cell sizes vary between pure B_2O_3 and the $Cs_2O(B_2O_3)_9$ complex, the presence of Caesium does not affect the density significantly. ⁽¹⁶³⁾

Table 11 shows the calculated bond lengths and bond angles in the optimised $Cs_2O(B_2O_3)_9$ crystal.

Table 11 - Comparison of structural information on calculated D1 and Caesium Crystals. Showing experimental (exp.) ⁽¹⁶²⁾ and simulated data (calc.)

	B_2O_3		$Cs_2O (B_2O_3)_9$	
Bond Length				
Bond	Distance (Å)			
	<i>Exp.</i>	<i>Calc.</i>	<i>Exp.</i>	<i>Calc.</i>
B1 – O1	1.47	1.506	1.36	1.38
O1 – B2		1.492		1.33
O1-O2	2.30	2.375		
Bond Angles				
Angle	Angle (°)			
	<i>Exp.</i>	<i>Calc.</i>	<i>Exp.</i>	<i>Calc.</i>
B1 – O1 – B2	120 -130	114.86	128	116.21
O1 – B2 – O3		104.99		121.52

We observe that the average length of the B – O bond is 1.506 Å, and 1.355 Å in pure B₂O₃ and Cs₂O(B₂O₃)₉, respectively, which shows that Caesium inclusion shortens bond lengths and increases bond angles, straining the bond in comparison. The average bond angle in the Caesium-containing crystal is significantly greater than the corresponding one in pure B₂O₃. This is due to many factors including the electronegativity, size of atoms and coordination, as will be discussed in later sections. The bond stances in both B₂O₃ and Cs₂O(B₂O₃)₉ have been closely matched to that shown in experimental research. In fact, for both simulated pure B₂O₃ and Cs₂O(B₂O₃)₉ the bond length for B-O, O-B and O-O have been accurately simulated compared to experimental data. However, where bond angles are concerned, the discrepancy may highlight the fact that experimental data show greater presence of boroxol rings within the structure. Usually around 130° in O-B-O angle represents data indicative of more boroxol rings.

7.4.3 Porosity

To evaluate further the structural properties of the Cs-containing system, porosity calculations were performed. Porosity analysis aids in identifying of how much empty space or “voids” is found within a cell. In this work, the porosity analysis tool provided in the VESTA program has been utilised. VESTA conducts the porosity analysis by applying a full occupancy value or zero. When the site shows less unity through bond and electronic information, the site is treated as a virtual site which displays no atoms are displayed, giving a strong indication of zero occupancy at the virtual site. ⁽¹⁵⁹⁾

Porosity calculations for the optimised crystal structure showed that the total filled space of atoms was 60.86% per unit cell, with a void space of 39.14% per unit cell. The calculated porosity for the B_2O_3 crystal was 18.22%, *i.e.*, a difference of 20.92% showing that upon Cs-inclusion, the material creates more void space, and hence a greater porosity.

This difference in porosity could be seen in terms of differences in cation radius. Caesium is a large atom, with a radius of 300 pm, in comparison to boron and oxygen, which have atomic/ionic radii of 180 and 60 pm, respectively. Therefore, inclusion of this large atom within this crystal causes an expansion and displacement from that seen in pure B_2O_3 , with corresponding changes in atomic positions and bond lengths. Further data relating to the polyhedral structure including the average length and distortion index alongside the polyhedra volume are reported in **Table 12**. Despite the presence of four boroxol rings within the structure, the BO_3 groups are identified as a three-separate polyhedron, after caesium ion addition to the system. The bond lengths in the rings are close to those found in the planar groups. The caesium forms a tetracaidecadeltahedron, *i.e.*, it has 9 vertices and is structured through square pyramids that are not uniform. These types of polyhedra have 21 edges and 14 faces, fitting the D_{3h} symmetry group. ⁽¹⁶⁴⁾ The boron, in this case, forms the regular triangular tetrahedron, with four equilateral faces.

Table 12 – Calculated polyhedron comparison of atoms within the caesium-containing crystal.

Polyhedron Centre	Cs	B
Bond Length (Å)	3.2761	1.3636
Polyhedral Volume (Å ³)	59.4247	0.0265
Distortion Index	0.02614	0.02259
Effective Coordination Number	9.6479	2.8993

As noted, the Cs-containing crystal has four boroxol rings, shown in **Figure 59**. The average B-O bond length is 1.355 Å whilst the average B-O-B angle is 123.5°. It is also still smaller than that seen for the D1 system but closer to the idealistic value of pure B₂O₃ boroxol ring information. ⁽¹¹⁷⁾

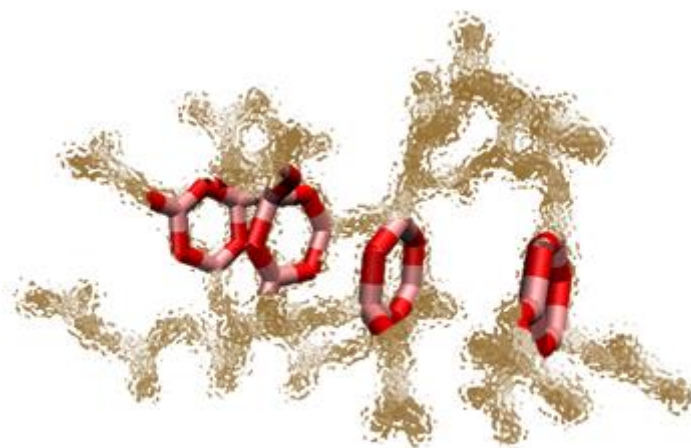


Figure 59 - Boroxol rings present in the caesium crystal, with pink as the boron atoms and red as oxygen atoms.

7.5 Chapter Conclusions

From studying the D1 and caesium-containing crystal, there were many similarities and differences. The distances pertaining to the boron and oxygen connectivity in the system, shows that the boron trioxide crystal has smaller B-O-B and O-B-O angles. A 9:1 ratio ($B_2O_3:Cs_2O$), caesium oxide doped B_2O_3 crystal was investigated hypothesising that it would closely mimic pure B_2O_3 . The results presented in this chapter indicate that the interatomic distances decrease with the inclusion of Cs_2O .

Despite the high B/Cs ratio, the caesium atoms cause significant structural changes, moving from triclinic to orthorhombic structures, and changes in the polyhedral structure (2.8). The structure remains dominated by BO_3 polyhedra.

In conclusion, the caesium crystals investigation has given us an insight into the electronic and structural properties. The addition of Cs_2O provides more void space within the system, possessing a greater level porosity. As the crystalline states were studied. There is an indication that the pure B_2O_3 crystal has a more packed and periodic structure.

8 SODIUM BORATE CRYSTAL

8.1 Abstract

Having obtained glassy structures from MD melt-quench and characterised the crystal structure using DFT we now move on to consider various crystalline sodium borate crystals, to see the effects on the B_2O_3 network within well-defined and accurately characterised structures. As seen for Cs-doping the structural groups pertaining to boron remained as BO_3 with no presence of BO_4 groups, except in $B_7Na_3O_{12}$. Detailed examination of these crystal structures containing different Na/B ratios can inform our understanding of the effect of alkali ions as network modifiers in glassy and amorphous phases.

The boron-centred polyhedra and the development of boroxol rings are directly influenced by Na concentration. The boron was found in a triangular planar group with a coordination of 3 in most sodium-doped crystals studied. The presence of these sodiums also increased semi conductive ability that pure B_2O_3 doesn't possess, and a clear indication with an additional of an alkali metal into the network. Small amount of sodium can also create substructures such as molecular cages seen with 1 and 1.5 ratios.

8.2 Aims and Introduction

One of the most utilised alkali ions used within borosilicate systems is sodium. In these types of systems, sodium acts as a network modifier, see **section 1.3.3.2**. This is due to sodium being one of the most abundant elements in the earth's crust. It is widely used a dopant or modifier in many different types of material.

In this chapter, a variety of different sodium oxide to boron trioxide ratios are investigated. The ratios include monosodium system ($\text{Na}_{36}\text{O}_{72}\text{B}_{36}$), a disodium system ($\text{Na}_4\text{B}_8\text{O}_{14}$), and a triborate ($\text{B}_7\text{Na}_3\text{O}_{12}$).

Furthermore, the electronic and elastic properties of these crystals were calculated. The main aim of this chapter is to discuss how the metal cations, B and Na, affect the bonding within the boron oxide network through looking at model crystalline systems. It allows for a comparison to the pure B_2O_3 crystal investigated in the previous chapter.

8.3 Computational Details

All crystal structures were obtained from the crystallographic database, ICSD. The data file of $\text{Na}_4\text{B}_8\text{O}_{14}$ was obtained from the crystallographic database and used throughout this experiment. (CIF ID: 1537502). The structure was determined by Kanischeva et al. using single crystal x-ray diffraction. The crystals were obtained experimentally from hydrated metaborates, by combining boric acid with sodium hydroxide. ⁽¹⁶⁷⁾ The structures of monosodium $\text{Na}_{36}\text{O}_{72}\text{B}_{36}$ (CIF ID: 1010015).⁽¹⁶⁸⁾ and $\text{B}_7\text{Na}_3\text{O}_{12}$ (CIF ID: 1534009) obtained by x-ray diffraction methods, the latter possessing a triclinic crystal system. ⁽¹⁶⁹⁾

The VASP optimisation settings from the previous chapter were employed here, **page 166**.

To define the Young's Modulus (YM) of the system we use the calculated elastic constants and bulk modulus values. The YM is calculated from the equation below.

$$YM = \frac{9\mu K}{(\mu + 3K)} \quad (36)$$

Where μ is the shear modulus and K represents the bulk modulus.

8.4 Results and Discussion

8.4.1 Disodium Borate $\text{Na}_4\text{B}_8\text{O}_{14}$

The resulting structure after optimisation as seen in

Figure 60 indicates a system with complex structure and connectivity. $\text{Na}_4\text{B}_8\text{O}_{14}$ has a strongly bonded structure due to the crystalline connectivity in the network, detailed later in this chapter.

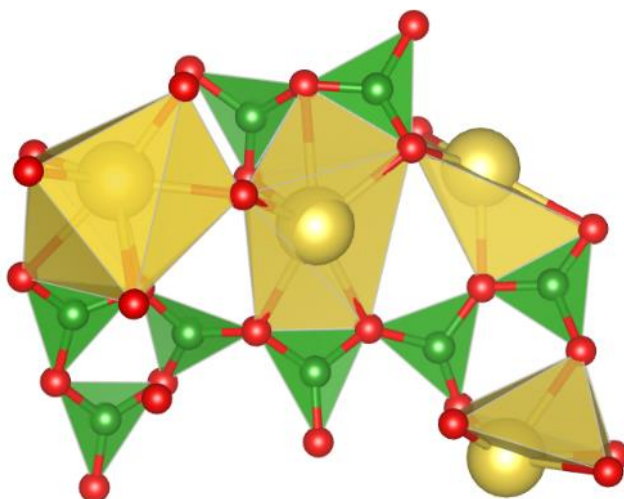


Figure 60 – Polyhedra representation of the $\text{Na}_4\text{B}_8\text{O}_{14}$ system showing the yellow sodium-based polyhedra and the green boron-based polyhedra. Red represents the oxygen atoms.

8.4.1.1 Structural Analysis of $\text{Na}_4\text{B}_8\text{O}_{14}$

This crystal is a triclinic type of system. Hence, the structural transition seen upon Cs-insertion in **Chapter 7** is not repeated here as that possessed an orthorhombic structure.

8.4.1.2 Na₄B₈O₁₄ Polyhedra

From the polyhedral analysis and the different structural motifs presented in **Figure 61**, it is seen that each the four sodiums present within this system are crystallographically distinct, and each occupies a different type of space within the cell. The green polyhedra are those containing boron, whilst the yellow polyhedra are sodium centred. The boron atoms have formed trigonal planar polyhedra but in the case of sodium, there is no consistent polyhedral type and the four Na exhibit coordination numbers of 7, 5, 4 and 3.

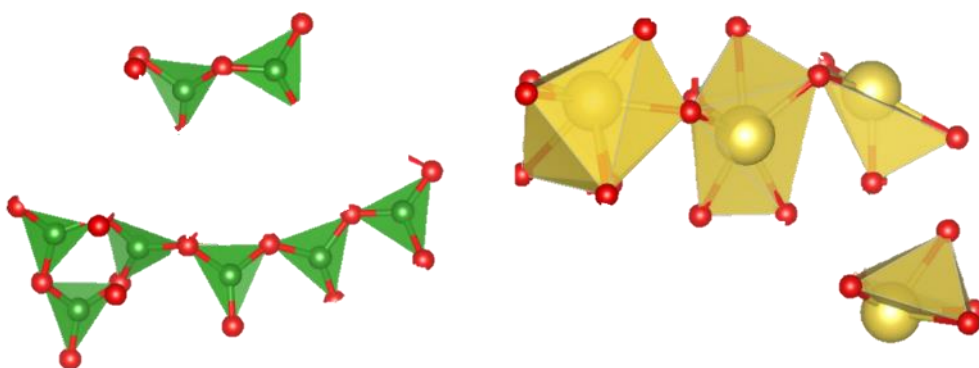


Figure 61 - Polyhedra identified within the Na₄B₈O₁₄ crystal. Green highlighting the Boron polyhedra and yellow highlighting the sodium-based polyhedra. Red spheres represent oxygen.

The Na₄B₈O₁₄ system contains 12 polyhedra, summarized in **Table 13**. The polyhedra are analysed in terms of polyhedral volume, each of the four sodium atoms present very different values. This difference in values is a result of the different coordination of each sodium atom attains.

In Vesta, the crystal structures can be represented by coordinating polyhedra. These consist of central atoms, linkages, and apex atoms. The polyhedral volume refers to the atoms or groups of atoms which are now express as solid spheres or displacement ellipsoids and the bonds within the structure which are represented by cylinders or lines. This can give us an idea of the volumetric occupancy of an atom or a series of atoms within an entire simulation cell.

Table 13 - Polyhedra data for the Na₄B₈O₁₄ crystal with effective coordination data rounded to 3 significant figures

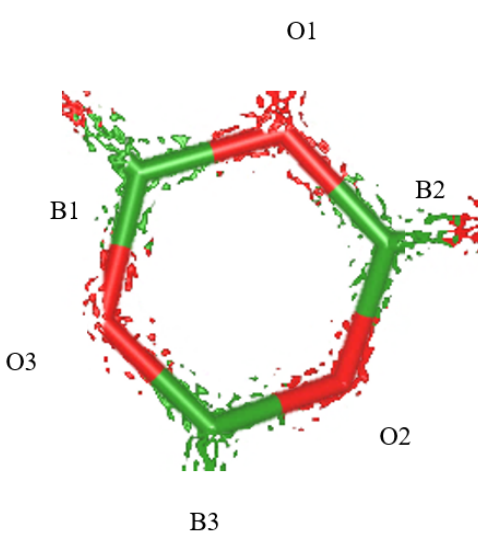
Polyhedron Type	Na1	Na 2	Na 3	Na 4	B
Bond Length (Å)	2.5779	2.4539	2.121	2.4355	1.3817
Polyhedral Volume (Å ³)	22.0530	12.6880	4.4413	8.4117	0.02815
Distortion Index (Å)	0.08141	0.05792	0.0381	0.09194	0.02527
Effective Coordination Number	6.98	5.10	4.68	3.17	2.87

In the Na₄B₈O₁₄ system, the coordination around the Boron atoms approximates to 3, representing three apex atoms within the polyhedra. This equates to the trigonal planar groups seen within the pure B₂O₃ compound. The value of the boron coordination is the same as found in the caesium-containing crystal investigated in the previous chapter, indicating that changing the alkali metal does not markedly affect the boron coordination. For the Na polyhedra, the coordination differs for each of the central sodium atoms. However, this does not affect the coordination seen for the BO₃ groups, as these are observed to have a constant value of 3.

8.4.1.3 Na₄B₈O₁₄ Ring and Bonding Info

Visual analysis of the crystal shows a group of planar linked triangles forming one boroxol ring in this crystal, **Table 14**. The average B-O bond length within this boroxol ring was 1.3872 Å. This differs from pure B₂O₃, which we saw in chapter 7 had an average B-O bond length of 1.499 Å. With the addition of sodium ions, the B-O bond length has decreased. However, compared to the B-O bond shortening observed upon Cs-doping (1.355 Å), Na-doping does not lead to as big a decrease in bond length. This difference might be due to dopant atom size effects, with sodium having markedly smaller radii (227pm) than Caesium (300 pm).^(160a) The average bond angle within the boroxol ring, B-O-B in Na₄B₈O₁₄ was calculated to be 116°. as compared to 114° for B₂O₃ and 116° for Cs-doped crystal.

Table 14 - Boroxol ring found within Na₄B₈O₁₄ and corresponding structure data.



Bond	Distance (Å)
B1 – O1	1.38
O1 – B2	1.40
B2 – O2	1.38
O2 – B3	1.38
B3 – O3	1.40
O3 – B1	1.40
Bond Angle	Angle (°)
B1 – O1 – B2	116.52
O1 – B2 – O2	116.97
B2 – O2 – B3	114.63
O2 – B3 – O3	117.26
B3 – O3 – B1	118.59

In the glass network, these alkali metal ions act as network modifiers which modify and disrupt the structural arrangement to a varying degree. The specific ion within the investigated crystal is sodium, with the $\text{Na}_2\text{O} : \text{B}_2\text{O}_3$ ratio being 2:1. The average bond distance from Boron-to-Boron atom was between 3.5-3.6Å.

Previous research involving a combination of alkali ions within the B_2O_3 structure has shown that having an approximate 1:2 ratio of Na_2O to B_2O_3 in the glass leads to B-O bond lengths approximating to 1.44 Å. ⁽¹⁷²⁾

This is comparable to our calculated data, though slightly longer on average. However, the experimental system did have an addition of 4% aluminium oxide, which would tend to increase the average bond length in the network. ⁽¹⁶¹⁾

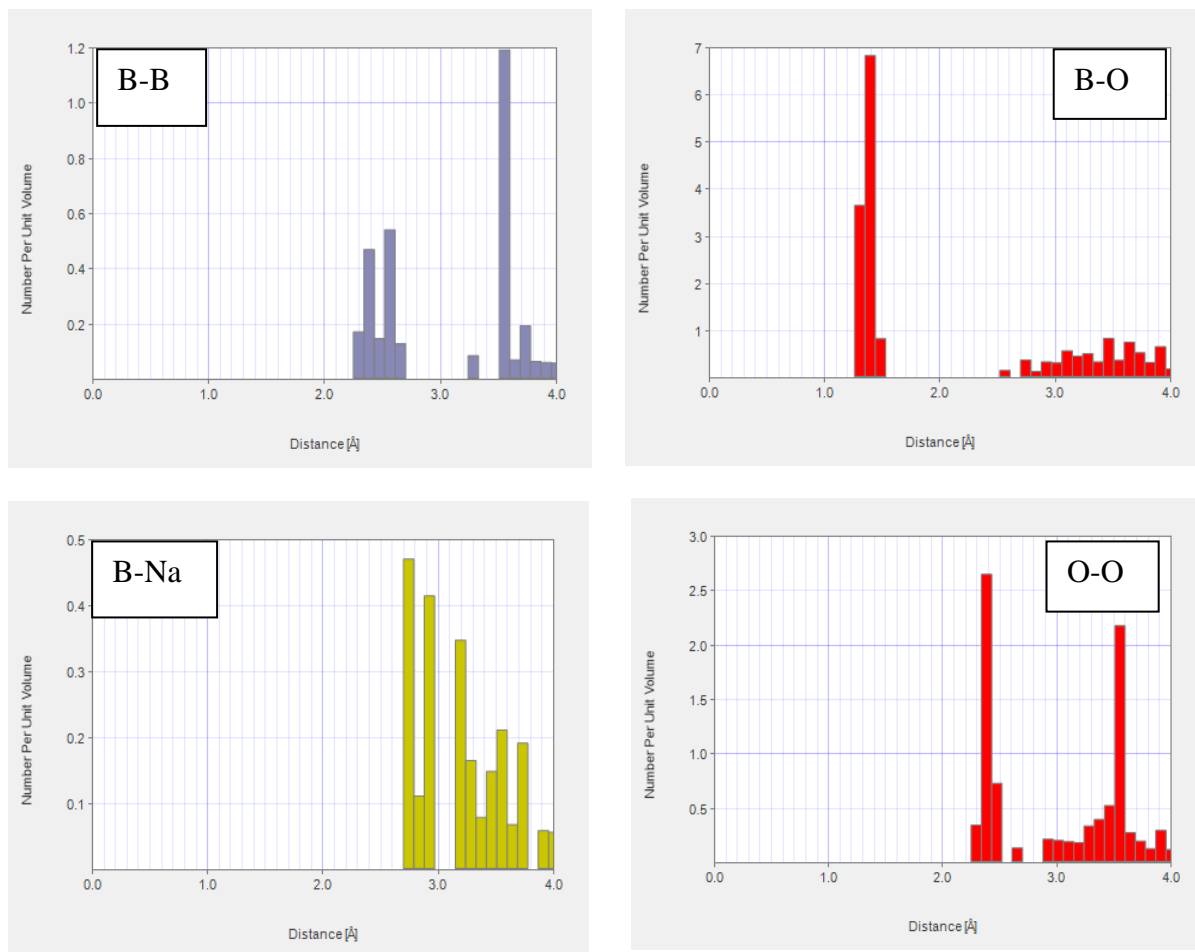


Figure 62 - Distribution plots of interatomic distances within the $\text{Na}_4\text{B}_8\text{O}_{14}$ structure.

Figure 62 gives more detailed information of the interatomic stances in $\text{Na}_4\text{B}_8\text{O}_{14}$. It provides a comparison of the average bond distances between the different bonds. As we can see the B-Na bond distances are between 3.6 and 4.0 Å. This is comparatively a lot higher than distances seen for B-O bond.

The structure contains a 6-membered ring with 2 B and one Na, as seen in **Figure 63**. The O-Na-O angle is 78.25° and hence the ring structure appears to be strained as the angles are more acute than seen elsewhere.

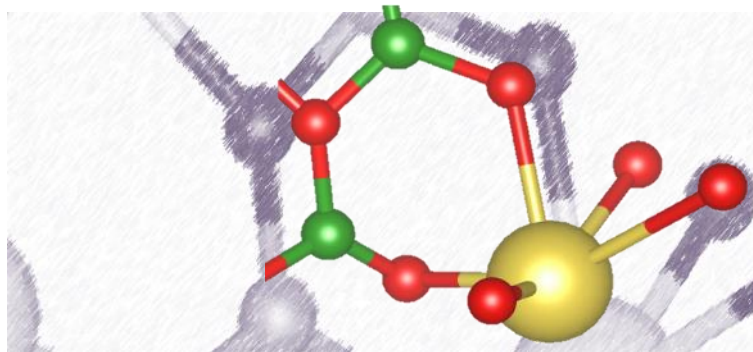


Figure 63 - The structural effect of sodium ion addition within boroxol ring.

One of the most common structural motifs present within this crystal is the 4-membered ring - encasing defined by one boron and one sodium atom with two oxygen atoms included as seen in **Figure 64**. This feature is not unique to boroxide glass but is commonly seen within silica-based glasses and crystals that are infused with alkali oxide or other addition ions such as Nitrogen. ⁽¹⁷³⁾

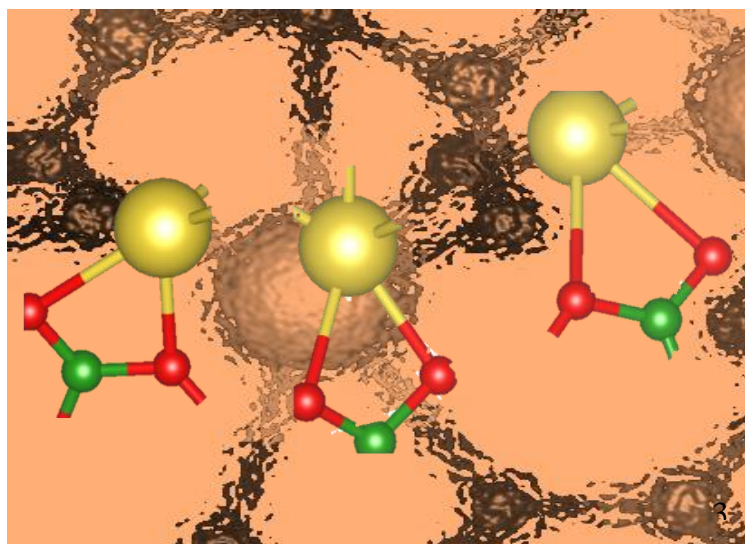


Figure 64 - Four-Membered Ring structures within the $\text{Na}_4\text{B}_8\text{O}_{14}$.

Table 15 - Four-Membered ring information found within the Na₄B₈O₁₄ system.

	Distances / Å		
	Ring 1	Ring 2	Ring 3
O – Na	2.39474	2.487405	2.801455
O – B	1.35365	1.396235	1.368035
	Angles / °		
Na - O - B	87.70515	95.47845	93.0443
O - B - O	124.2793	109.4647	121.7872

The angles and bond lengths in the four-membered ring are presented in **Table 15**. It is interesting to observe that the B-O bond length stays within similar ranges seen in the pure B₂O₃ system. In the RDF of B₂O₃, the values of the first peak for the B-O bond were around 1.35-1.37 Å. Now with the inclusion of sodium ions, the average B-O bond length is slightly increased to 1.39 Å, but no significant difference is seen. If we collate values from these four-membered rings, the average drops to 1.373 Å. It can be noted that the O-B-O angle in this structure exhibit a wide range from 109.5 ° to 124.3 °, averaging 118.51°. This value is a 3% increase in value to that seen within the pure B₂O₃ system.

8.4.1.4 Na₄B₈O₁₄ Electric and Elastic Properties

8.4.1.4.1 Dielectric Properties

To further understand the system's electronic properties, the dielectric constant was investigated. This produces a quantitative measure of the ability of a system to store energy within an electric field. Both the high frequency and static dielectric tensors were calculated during the study, resulting in a value of 1.29302. This value is related to free spaces within the structure and is defined in **Chapter 2**. The value is surprisingly low for an oxide, which usually has a higher dielectric constant, for instance Al₂O₃ has a value of around 9.

Nonetheless, this result indicates that the material in question would not hold its electrical charge for long periods of time. In the glassy state, the material would suffer from permanent damage if any changes to the electric field are made, giving important consequences within the industrial application as changes to any system can cause damage to equipment. However, this low value is beneficial for use in electronic equipment used as high-frequency transmitters as this will not degrade under the powerful electric fields. The calculated data can be seen in **Table 19** with '*Local field effects*' referring to the inclusion of any changes to the Hartree potential which results in the cell periodic microscopic changes of the local potential. In Sodium Phosphate and Sodium Dichromate, there is also a lower (than expected) dielectric value (1.6-1.9 and 2.9).⁽¹⁷⁴⁾ This doesn't rule out this material as a candidate for glass production as further addition of other metal can improve this dielectric property.

Table 16 - Table showing both the calculated High frequency and Static Tensors of the Na₄B₈O₁₄.

High Frequency – Macroscopic Dielectric Tensor (including local field effects in DFT)			Static Macroscopic Dielectric Tensor (including local field effects in DFT)		
2.121964	-0.28847	-0.011675	3.507452	0.105628	-0.262722
-0.028849	2.435516	0.001468	0.120802	8.150269	-0.122490
-0.011675	0.001469	2.475261	-0.57402	-0.78600	10.780829

The benefits of calculating the dielectric constant values are that they can provide information on conductor and semi-conductor abilities. Those properties can be identified through the two top bands, the conduction followed by the valency band. The difference between materials described as conductors, insulators and semiconductors are that between these bands are vacant sites which the conduction of electricity can happen. When the uppermost, conduction band is partly filled, it is described as a conductor. This is due to the electrons in this band which can move into vacant sites and act as free particles. When this top conduction band is nearly empty, the gap to the next valence band is important. Now, the difference between an insulator (material that is unable to conduct electricity) and semiconductor (material able to conduct electricity but not as well as a conductor) is that the semiconductor has a smaller gap to the conduction band. So therefore, the valence band electrons sometimes attain enough thermal energy to go into the conduction band. Knowing

this, helps us understand the sensitivity to changes in treatment conditions such as temperature changes and annealing processes. The dielectric value, itself is quite complex, as it has a dependency on various variables such as temperatures and pressure. It can be represented as a function of the frequency. ⁽¹⁷⁵⁾

8.4.1.4.2 Mechanical Properties

Depending on the crystal symmetry, the elastic constants require investigating different matrix elements. In the case of the Na₄B₈O₁₄, the crystal has triclinic type system and the values calculated here was seen also for other material in different literature investigation. ⁽¹⁷⁶⁾

Table 17 - Elastic Constants expressed in GPa for the Na₄B₈O₁₄ system

Property	Computational Result (GPa)
C ₁₁	293.757
C ₁₂	85.7473
C ₁₃	192.066
C ₁₄	-30.2516
C ₃₃	810.1672
C ₄₄	60.2725
$\equiv C_{66} \equiv (C_{11} - C_{12})/2$	104.00485

Calculated elastic constants are shown in table 20. The shear modulus provides a measure of rigidity, being the ratio between the shear stress and shear strain. Through the VASP output file, this is defined by the tensor. ⁽¹⁷⁷⁾ The value here, is 60.3 GPa. This result can be compared to pure silicon which provides a computationally calculated

value of 59 GPa. A higher shear modulus implies a greater force required to mechanically deform a system. ⁽¹⁷⁸⁾

Another calculated shear modulus value is of diamond which has been calculated to be 500 GPa.⁽¹⁷⁹⁾ This value is much higher but gives an idea of the strength of diamond in comparison to materials such as silicon and Na₄B₈O₁₄.

Another comparison was drawn to other sodium borate systems. Some research of sodium borate glasses with varying Na₂O portions has been carried out by Jaccani *et al.* ⁽¹⁸⁰⁾

The comparison here is difficult as this research looked at glasses and melt and furthermore these materials had higher proportions of B₂O₃ than Na₂O in comparison to this research.⁽¹⁸⁰⁾ When looking at annealed glasses with a mole percentage of 30% Na₂O – 70 % B₂O₃ (equating to almost 1:2), the shear modulus at the lowest temperature was ~24GPa. However, considering defect contribution and the configuration changes throughout the melt and quench phases, a reduced shear modulus value is to be expected as a system moves from crystal to melt and quench stages.

The calculated bulk modulus value is of Na₄B₈O₁₄ is 155.08 GPa. Other oxide-based crystal produced a bulk modulus value of 193.7 and 118.1 GPa for MgO and CaO respectively. For other silicon oxide-based crystals such as Al₂SiO₅, the calculated value ranges from 115.6 – 287.6 GPa.⁽¹⁴⁰⁾ The extensive difference in the range comes from larger percentages of silica oxide than aluminium oxide in the crystals

investigated, presenting a greater bulk modulus value. Hence, our calculated B sits within the expected values for a structure like ours.

As the bulk modulus is a relative change between a system's volume produced through a unit of compression and/or stress acting on a material, another way this property can be investigated is through a modification of pressure acting on a system and comparing this to the volume. This can be seen in **Figure 65**.

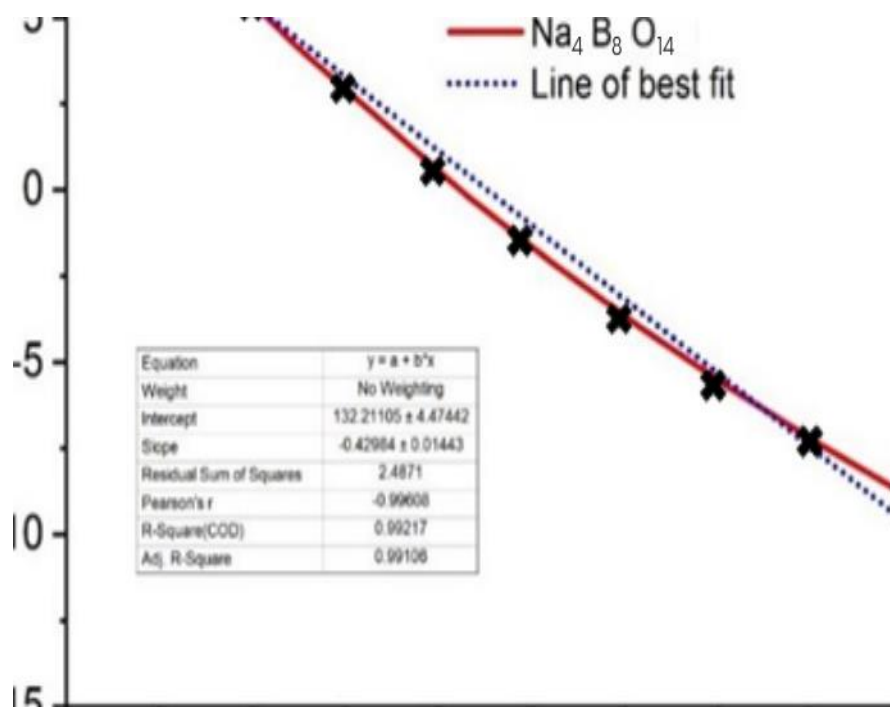


Figure 65 – Graph presenting pressure against volume to calculate the value of the Bulk Modulus for the $\text{Na}_4\text{B}_8\text{O}_{14}$

Through this method, the bulk modulus value becomes 132.211 GPa from the intercept of the line of best fit in the graph. The percentage difference between this new value is 15% from the previous.

Computational studies of Boron nitride and boron phosphide crystals have shown vastly different results from corresponding experimental studies. Through experimental research, by Greene *et al.* the bulk modulus was found to be 369 and 173 GPa for the nitride and phosphide crystals, respectively. DFT calculations of the bulk modulus gave values of 398.9 and 180.4 GPa for the same crystals respectively. ^(181,182) Therefore, our calculated value shows a good agreement with the experimental value. It must also be considered that within experimental data relates to crystals that may possess defects and impurities which would affect the values and “hardness” of the material.

Finally, to define Young’s Modulus (YM) for $\text{Na}_4\text{B}_8\text{O}_{14}$ system we require the elastic constants and bulk modulus values. YM is associated with a systems tensile elasticity, as shown in **Section 6.5.2**.

The value attained for the YM was 255.0086 GPa which will be compared later in this chapter.

8.4.1.4.3 $\text{Na}_4\text{B}_8\text{O}_{14}$ Charge Density

The charge distribution in the lattice (

Figure 66) obtained from the VASP calculations can be visualised using VESTA. The charge distribution is primarily based around the Oxygen atoms throughout the simulation cell, being the most electronegative element in the system studied. The image in

Figure 66 indicates a small degree of covalency between the sodium atom and the oxygen in the BO_3 formation. The charges lay solely on the oxygen atoms and the diagram also indicates how these ions are charged, Na^+ and O^- .

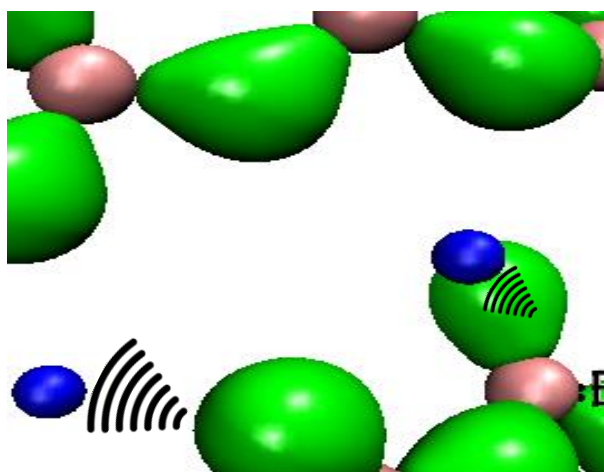


Figure 66 - Charge Distribution in $\text{Na}_4\text{B}_8\text{O}_{14}$ with the blue indicating sodium atoms and the pink indicating boron. Green displays a charge isosurface.

8.4.2 Monosodium Borate $\text{Na}_{36}\text{O}_{72}\text{B}_{36}$

Having established an understanding for the effect of Cs-doping, and Na-doping at the 2:1 ratio, the next ratio of sodium to be investigated was a monosodium crystal, $\text{Na}_{36}\text{O}_{72}\text{B}_{36}$ which has a 1:1 ratio between Na_2O : B_2O_3 . This ratio has been used experimentally for other household materials and is often used in borosilicate glass production. **Figure 67** shows the structure of this trigonal crystal.

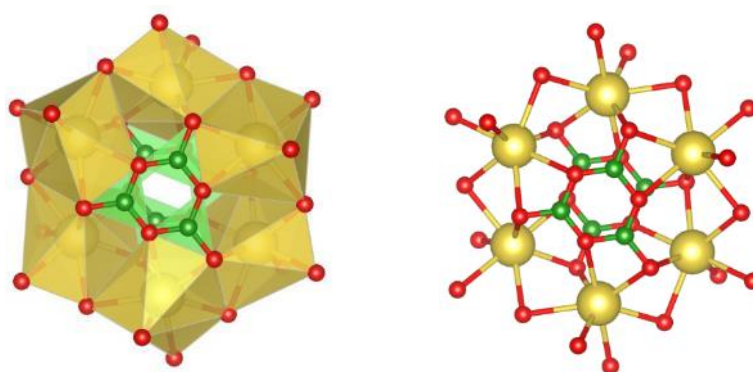


Figure 67 - $\text{Na}_{36}\text{O}_{72}\text{B}_{36}$ Crystal

This crystal also has a P1 space group with a volume of 266.011 \AA^3 with 67 atoms and 84 bonds and 20 polyhedra, further examined in the later sections.

8.4.2.1 $\text{Na}_{36}\text{O}_{72}\text{B}_{36}$ Structural Information

As seen in **Figure 68**, there are two visible boroxol rings that can be seen when using the visualisation software. **Table 18** gives bond distance and angle data, distinguishing between geometries within the rings, and those outside (or between) rings.

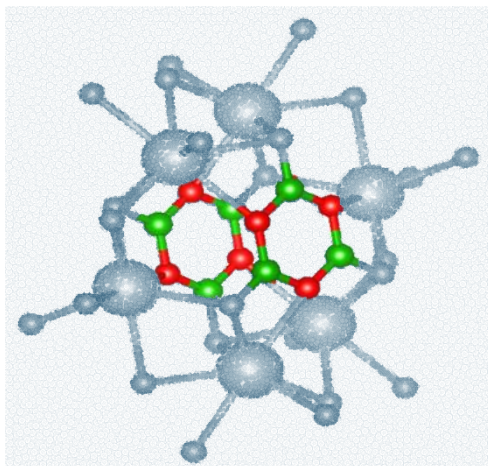


Figure 68 - $\text{Na}_{36}\text{O}_{72}\text{B}_{36}$ Crystal displaying the two Boroxol rings present within the system.

It can be seen the average distance for the B-O bond within the boroxol rings to be 1.337 Å. Now the data for this bond can be compared to the di-borate system (1.387 Å) and the caesium borate crystal (1.355 Å). Despite this crystal having a 1:1 ratio of $\text{Na}_2\text{O}:\text{B}_2\text{O}_3$, the bonding within the boroxol ring has the smallest lengths in comparison to all other materials investigated.

Table 18 - Average bonding within the $\text{Na}_{36}\text{O}_{72}\text{B}_{36}$

Bond	Average Distance (Å)
B-B (<i>ins</i>)	2.31518
B-B (<i>out</i>)	3.50010
B-O (<i>ins</i>)	1.33667
B-O (<i>out</i>)	1.39634
Na-O	2.53425
Bond	Average Angle (°)
B-O-B (<i>ins</i>)	120.000
B-O-B (<i>out</i>)	120.000
Na-O-B	142.0036

“*ins*” indicates within the ring system and “*out*” represents average distance outside the system.

The boroxol ring is not the only moiety that can be identified within this crystal structure. There are other groups that appear which were present in the previous sodium-based crystal. Previously four-membered rings had been noted. $\text{Na}_4\text{B}_8\text{O}_{14}$ had three of these types of rings, whereas this $\text{Na}_{36}\text{O}_{72}\text{B}_{36}$ crystal has twice as many.

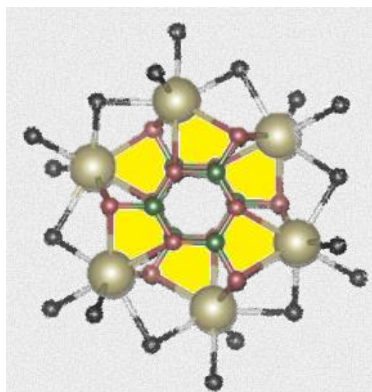


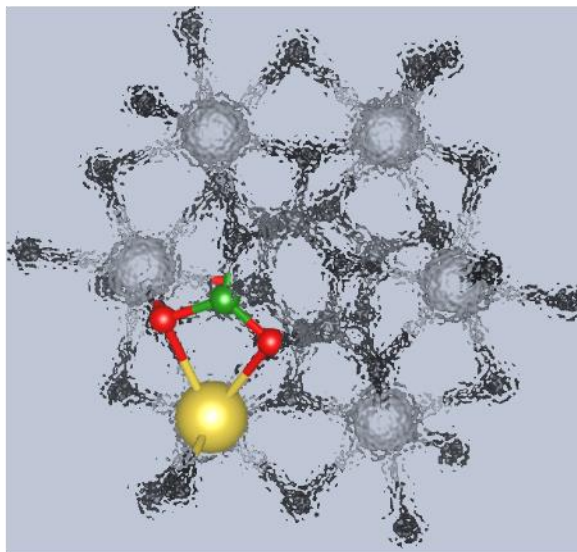
Figure 69 - $\text{Na}_{36}\text{O}_{72}\text{B}_{36}$ Crystal with the yellow highlighting four-membered ring

The rings highlighted in **Figure 69** were shown to be identical. Therefore, all bonds and angles in these four-membered rings were equal and did not differ as they did in the 2:1 ratio crystal described earlier.

In the 2:1 ratio crystal the O - Na bonds averaged 2.561 Å with the Na - O - B angle at 92.076°. Although this bond length is similar in both crystals, the average angles seem to differ. As noted, the Na - O - B angle was larger in the disodium crystal than in $\text{Na}_{36}\text{O}_{72}\text{B}_{36}$. The opposite is true for the O - B - O angle which is slightly smaller in this crystal than the disodium crystal which averages at 118.51°.

Table 19 - Data for four-membered rings in Na₃₆O₇₂B₃₆.

Bond	Distance / Å
O - Na	2.52379
O - B	1.3964
Bond	Angle (°)
Na - O - B	88.3741
O - B - O	120.000



In conclusion, 4-membered ring formation is common in both sodium borates yet occurs in higher proportions in the monosodium crystal. The disodium crystal exhibits the same moiety but the bond length and, particularly, angles differ. This can be related to other studies where boroxol rings see less distortion when smaller amounts of metal oxides are added to the system.

8.4.2.2 Na₃₆O₇₂B₃₆ Polyhedra

As seen in **Figure 67**, the VESTA output for polyhedra shows a symmetrical configuration in comparison to the previous crystal. There are 12 polyhedra within the structure, 6 surrounding Na and 6 B. As shown in **Table 20** the sodium polyhedra are much bigger than the boron counterpart, as the BO₃ polyhedra are essentially planar. Furthermore, the Na₄O₁₄B₈ showed a variety of diverse Na polyhedra this monosodium does not. The average for the previous crystal was 11.891 Å³. This

monosodium crystal provides a large volume for the sodium based polyhedra, at a value of 23.4298 Å³.

Table 20 - Polyhedra data with respect to the Monosodium crystal

Polyhedra Type	Na	B
Bond Length	2.3532	1.3566
Polyhedra Volume	23.4298	0.0001
Distortion Index	0.00643	0.01955
Effective Coordination Number	6.98	2.96

8.4.2.3 Na₃₆O₇₂B₃₆ Elastic Properties

To calculate the elastic constant the same properties are calculated from the Voigt matrix.

Table 21 - Elastic Constant Calculations for Na₃₆O₇₂B₃₆.

Property	Computational Result (GPa)
C ₁₁	471.37
C ₁₂	411.72
C ₁₃	331.71
C ₁₄	-68.23
C ₃₃	375.27
C ₄₄	76.56
$\equiv C_{66} \equiv (C_{11} - C_{12})/2$	29.83

This system has a shear modulus of 76.55 GPa, higher than the disodium borate crystal. The bulk modulus for this Na₃₆O₇₂B₃₆ crystal is calculated to be 188.28 GPa which is once again higher the Na₄B₈O₁₄ crystal. The Young's modulus this crystal was

84.99 GPa. This value is far greater than that seen within the disodium crystal, by 200%.

The high frequency and static dielectric constants were calculated to obtain the dielectric constant value. In this monosodium system, of the value was 1.0701. This value is lower than that of the disodium system by 17.2%. This is due to the additional sodium, changing the connectivity within the crystalline network. While both systems have a similar chemical configuration, the additional of an extra sodium atom changes the way in which the atoms occupy space. For any structure we can see some increased/reduction in bond length, changing the bond angles and other such structural information.

8.4.2.4 Na₃₆O₇₂B₃₆ Density of States

The DOS for the monosodium system shows a bandgap 3.37eV, indicating that the monosodium may also be a semiconductor. In fact, this is smaller than the previous sodium-based borate crystal. This material shows that in comparison with pure B₂O₃, the addition of sodium ion transforms the material to be more conductive. This is foreseeable through the fact that the sodium metal oxides are added, and similar trends have been seen with the sodium-based crystals investigated in this research. Nevertheless, there is very little difference between doubling the proportion of B₂O₃ and keeping the ratio 1:1.

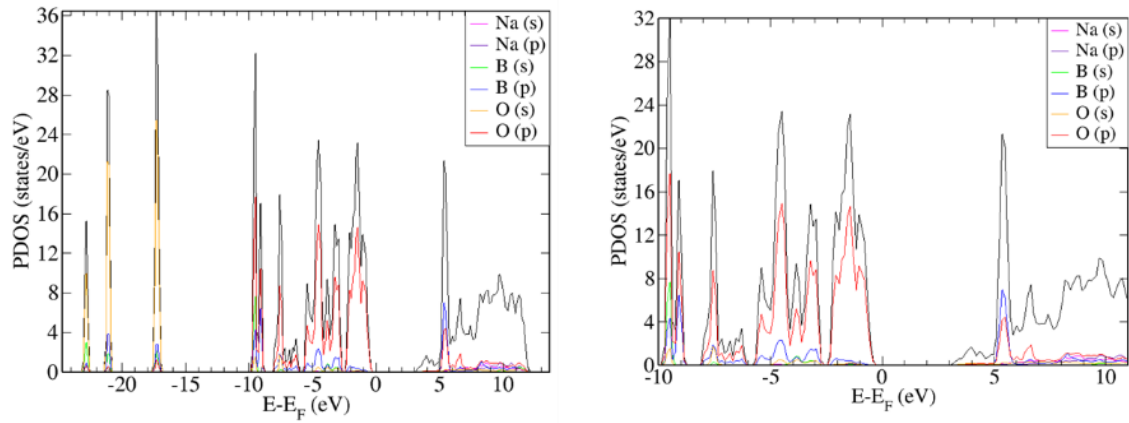


Figure 70 - Density of states for Na₃₆O₇₂B₃₆, a) Showing full DOS graph and b) Zoomed in to indicate conduction band.

8.4.2.5 Na₃₆O₇₂B₃₆ RDF

Figure 71 shows the RDF plots for this system. The regularity and sharpness of all peaks within **Figure 71**, is characteristic of a crystalline material. The prominent peak at 1.345 Å is indicative of the B-O bonded distance. This was also found in the crystalline B₂O₃ at 1.401 Å. A higher initial peak at 2.431 Å which is also found in the B₂O₃ at 2.387 Å with a secondary peak at 2.611 Å. The addition of Sodium introduces new data, including a Na-Na, B-Na and O-Na peak.

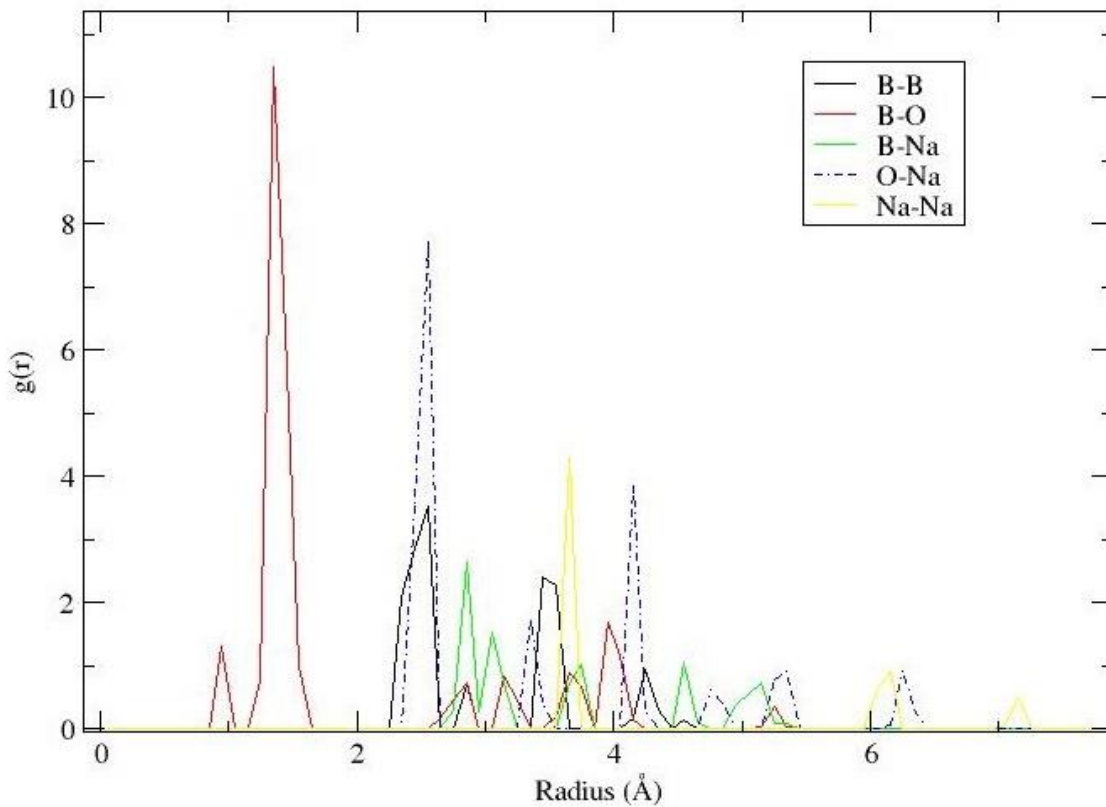


Figure 71 - RDFs for Na₃₆O₇₂B₃₆

8.4.3 B₇Na₃O₁₂ Crystal

B₇Na₃O₁₂, has a 1.5:3.5 ratio of Na₂O to B₂O₃. The unit cell contains 68 atoms and 82 bonds.

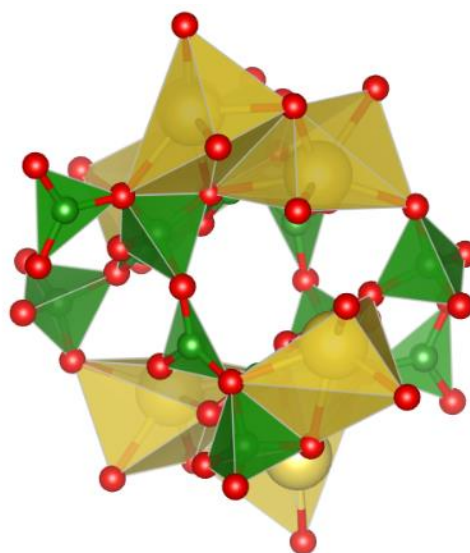
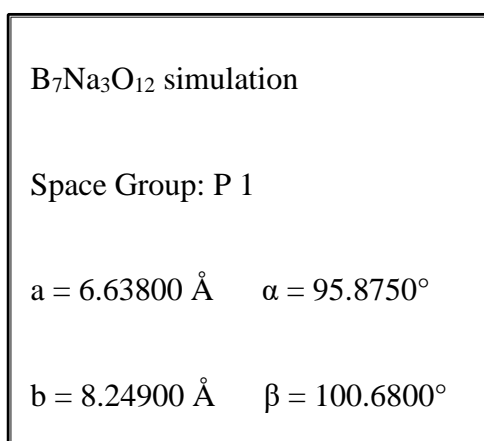


Figure 72 - Polyhedra highlighted for B₇Na₃O₁₂ with yellow highlighting the Na-based polyhedra and green indicating the boron-based polyhedra.

The material was simulated in P1 symmetry. The structure includes a molecular cage similarly to the monosodium crystal. ^(171a)

Many co-crystals of sodium borate and organic molecules such as 1,1,1-tris(hydroxymethyl)ethane form cage-like complexes due to the way in which sodium ions coordinate to multiple oxygen atoms whilst the boron trigonal units form important secondary building units. ⁽¹⁸⁶⁾

8.4.3.1 B₇Na₃O₁₂ Polyhedra

In this case, there are a total of 20 polyhedra present. We use these units to characterise the bonding geometries and other such structural information more easily. In the case of the sodium, there was a total of 6 polyhedra with two different types existing. Therefore, unlike the monosodium crystal, this sodium borate contains inequivalent polyhedra for both Na and B atoms. In the case of the first type of sodium polyhedron, the sodium atom is connected to 5 oxygen atoms. Additionally, BO₃ and BO₄ polyhedra are both present in the system, the presence of the tetrahedra. **Table 22** gives information on the polyhedra, including coordination numbers.

Table 22 - Polyhedra data for B₇Na₃O₁₂.

Polyhedron Type	Na Type 1	Na Type 2	B Type 1	B Type 2
Bond Length (Å)	2.4374	2.353105	1.37045	1.4729
Polyhedra Volume (Å ³)	12.84895	7.7959	0.0142	1.6347
Distortion Index	0.05835	0.04336	0.0077325	0.01055
Effective Coordination Number	5.10	4.38	2.99	3.97

The coordination numbers differ from the other crystals, as sodium adopts 4 and 5 coordination in this 1.5:3.5 ratio (Na₂O: B₂O₃) crystal. By contrast, the monosodium crystal structure showed Na coordination numbers up to 7, as did the disodium crystal.

8.4.3.2 B₇Na₃O₁₂ Density of States

The electronic density of states for the B₇Na₃O₁₂ shown in **Figure 73** indicates that most of the occupied states are found slightly below the Fermi level.

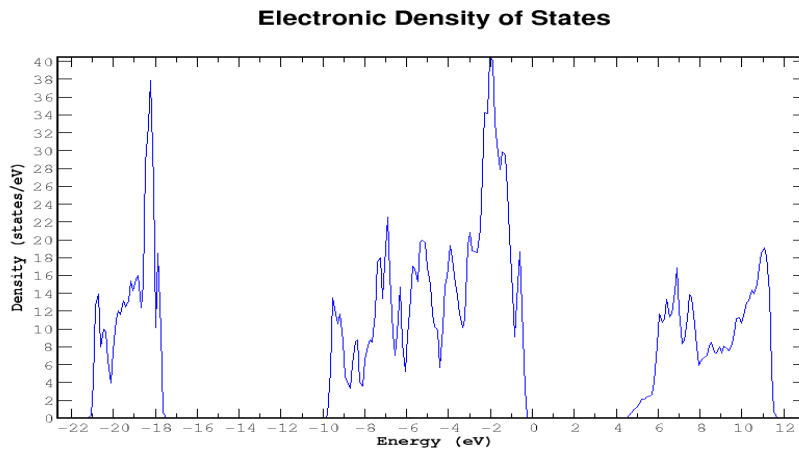


Figure 73 - Density of states for B₇Na₃O₁₂.

From the DOS, it is seen that the band gap is 4.5 eV. This is notably larger than the value for the monoborate system studied in the previous section, 3.37 eV. Commonly, materials with band gaps larger than 4 eV, are considered insulating. The resulting value corresponds with the use of borate systems in insulating fibreglass. Increased Na content appears to result in larger band gaps for borate systems, moving from semi-conductor towards insulator.

However, we note that the band gap value is far lower than the 8.48 eV seen with pure B₂O₃. This indicates that the difference between the conduction and valence band of electrons is lower in this sodium borate system, meaning the conductive properties are greater. This is observable with the present of the alkali metal atom, Sodium.

8.4.3.3 B₇Na₃O₁₂ Elastic Properties

Once again, the elastic properties were investigated as collated in **Table 23**. The shear modulus is calculated to be 70.6352 GPa, with the bulk modulus value of 174.3793 GPa. The Young's modulus value has been calculated as 243.717 GPa.

Table 23 – Calculated elastic constants (in GPa) calculated in the Voigt notation for B₇Na₃O₁₂.

Property	Computational Result (GPa)
C ₁₁	302.6113
C ₁₂	110.2633
C ₁₃	258.5563
C ₁₄	-50.6980
C ₃₃	625.7422
C ₄₄	70.6352
$C_{66} \equiv (C_{11} - C_{12})/2$	96.1740

The values are very interesting when considering the levels of sodium within each crystal. The trend has become apparent as the levels of sodium in the borate crystals increases the shear and bulk modulus decreases. The opposite is true for the Young's modulus values that see an increase in value as the proportion of sodium increases.

8.5 Chapter Conclusions

In this chapter, the effect of Na composition on sodium borate crystals was investigated using DFT techniques. A selection of varying concentrations were investigated: 1:1, 2:1 and 1.5:3.5 ($\text{Na}_2\text{O}:\text{B}_2\text{O}_3$).

Table 24 - The B-O bond distances for each of the crystal structures investigated in this research, indicating crystal ratio and configuration. Where X specifies the Alkali Oxide investigated.

Crystal Name	Crystal Configuration	Ratio (X: B_2O_3)	Bond Length (Å)
Pure Boron Trioxide	B_2O_3	-	1.50
Monosodium Borate	$\text{Na}_{36}\text{O}_{72}\text{B}_{36}$	1:1	1.36
Disodium Borate	$\text{Na}_4\text{O}_{14}\text{B}_8$	2:1	1.38
Sodium Triborate Crystal	$\text{B}_7\text{Na}_3\text{O}_{12}$	1.3:3.5	1.37
Caesium Enneaborate	$\text{Cs}_2\text{O}(\text{B}_2\text{O}_3)_9$	1:9	1.355

Polyhedral analysis revealed that Na-doping, and Na-concentration directly impacts the boron-centred polyhedra and the formation of boroxol rings. All sodium-doped crystals investigated placed boron in a triangular planar group with coordination of 3. An exception to this is the sodium “triborate” $\text{B}_7\text{Na}_3\text{O}_{12}$ where BO_4 tetrahedra are also present. The bond length varied as shown within **Table 24**. The calculated results in this research indicated that the Na atom does indeed affect the connectivity between BO_3 subunits.

Further to structural changes and trends observed upon Na-doping, the electronic structure of B_2O_3 was also shown to be directly impacted, especially looking at changes in band gaps between different Na concentration. The band gap of pure B_2O_3 (8.48 eV) was seen to decrease upon Na-doping, with the sodium-based crystals providing lower band gaps between 3-4 eV. Hence, upon Na-doping an insulator to semiconductor transition is seen.

9 CONCLUSION AND FUTURE WORK

From the research carried out in this project, we have been able to identify the key characteristics of the pure B_2O_3 structure. As many have suggested the trigonal planar subunits are found to be the most prevalent in this structure. However, it was also seen, that there are many key ring sub-structures that make up the entirety of the B_2O_3 glass network.

The boroxol group is, of course, a key structural unit in which some of the components are connected. Its presence creates a change in bond length and angle size. In the research carried out other rings are also present. One included a very small number of 4 membered rings in the molten state, which are full of torsion strain and are too weak to be maintain its shape in the glassy phase.

This research has also brought attention to the use of two and three body terms in interatomic potentials. The use of the two-body potential increases the amount of flexibility a system has but leads to difficulties in forming glassy- B_2O_3 .

In the case of the three-body term, the potential adds a restriction to the model and forming a suitable melt can be difficult, as the bonds are far more rigid, indicating a less accurate molten structure, but assisting in forming the glassy state. Despite these

issues, both were able to model each of the required states. A recommendation would be to include the three body terms once the system has melted appropriately.

Varying the system size has created an insight into the connectivity of the system on a larger scale than possible in previous investigations. Our research has revealed that the size of the simulation cell has no direct impact on which rings sizes are more dominant throughout the network. In fact, it was seen that BO_3 subunits gave the greatest frequency despite an increase in the number of atoms.

Although the BO_3 was the most dominant subunit present, there was an overall decrease in this portion, as the system size increased from 480 to 12960 to 30720 atoms, where less boron atoms were found to be in the BO_3 coordination and more BO_4 units became present.

Moving to the systems with addition alkali ions through alkali oxides, the results of simulations showed interesting result pertaining to the elastic constant data. This project has shown that the elastic constants show a direct trend with an increase in the portion of sodium within borate crystals, **Figure 74**. There was a decreased value of shear and bulk modulus indicating that when an internal force is applied, a borate with more sodium has a reduced ability to resist transverse deformation and less resistant to compression. However, this is correspondent with the fact that a greater portion of sodium also affects the stiffness of the system in its crystalline state, hence a higher Young's modulus value as there is a shown increase.

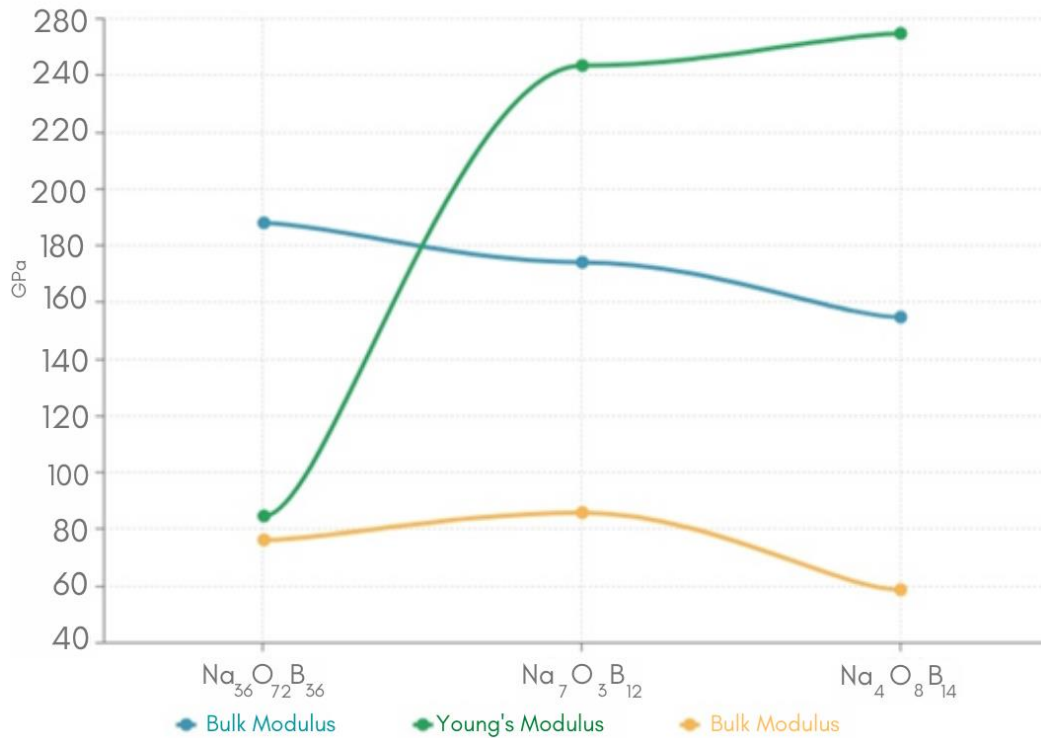


Figure 74 - Comparisons of Mechanical Properties for the sodium borate crystals investigated

The calculated elastic constants *via* the Voigt notation have several advantages but some drawbacks. The stress and strain constants are viewed and calculated separately, the coordinate systems rotation uses the bond relations and Mohr's circle (*a principle regarding bonding angles*) which may introduce algebraic errors. ⁽¹⁹⁰⁾

However, the advantage for the use of this method is the fact that this notation preserves the elastic density energy and elastic stiffness where other methods fail to do so. Furthermore, this type of notation is the most frequently employed. Further studies could potentially investigate the Kelvin notation; however, the stiffness components are changed, and it would be difficult to draw any comparisons.

With caesium addition, the ratio was thought to be large enough to mimic the properties of pure B_2O_3 . However, the results indicate that due to the size of the ion the system network was affected. The caesium creates a complex that adds steric factor altering that would be seen in pure B_2O_3 . This also corresponds to the elastic and mechanical properties calculated.

Understanding the way in which pure B_2O_3 is connected, helps identify the role in which it plays in borosilicate glasses. Boron trioxide is a vital component in understanding the connectivity of oxygen and boron when forming glass. The coordination investigation provides details of how the addition of alkali ion plays a major factor in the network these system display. This is essential in understanding that electrical and mechanical properties are indeed affected by these additions. The study of crystals in this way gives insight into industrial processes which aim to optimise properties such as dielectric constants can be investigated.

This project is a first step in crystal structural and property investigations varying the composition of borates. There are greater complexities with additional oxide components. As mentioned previously, the scope of alkali oxide additions in borate and borosilicates in endless and further variation in their compositions can optimise key mechanical, structural and chemical properties.

10 BIBLIOGRAPHY

1. Chakravorty, D. (1970). Inorganic Glasses. *Modern Aspects of Solid-State Chemistry*, 391–423. https://doi.org/10.1007/978-1-4684-1875-0_16
RSC (2015). Royal Society Chemistry. Retrieved 01/03/2015, from <https://edu.rsc.org/resources/roman-glass-and-its-chemistry/1962.article>
2. Karmakar, B., Som, T., Singh, S. P., & Nath, M. (2010). Nanometal-Glass Hybrid Nanocomposites: Synthesis, Properties and Applications. *Transactions of the Indian Ceramic Society*, 69 (3), 171–186.
<https://doi.org/10.1080/0371750x.2010.11090834>
3. Rasmussen, S. C. (2012). *How Glass Changed the World: The History and Chemistry of Glass from Antiquity to the 13th Century (SpringerBriefs in Molecular Science Book 3)* (2012th ed.). Springer.
4. Wacey, D., Fisk, M., Saunders, M., Eiloart, K., & Kong, C. (2017). Critical testing of potential cellular structures within microtubes in 145 Ma volcanic glass from the Argo Abyssal Plain. *Chemical Geology*, 466, 575–587.
<https://doi.org/10.1016/j.chemgeo.2017.07.006>
5. Brumagen, R., Davis, E., Elliott, K., Nace, A., (2014). A Century of Pyrex. Retrieved 01/03/2015, from <http://www.cmog.org/article/pyrex>
6. Davila, T., Epstein, M. J., & Shelton, R. (2006). *The Creative Enterprise [3 volumes]: Managing Innovative Organizations and People (Praeger Perspectives)* (Illustrated ed.). Praeger.

7. Cmog.org. Lantern Image [Internet]. Corning Museum of Glass. 2015 [cited 2015 Sep 20]. All About Glass. Available from:
<http://www.cmog.org/article/lighting-way-fresnel-lens>
8. M. Corrêa Pinto, A., Macedo, M. F., & G. Vilarigues, M. (2018). The conservation of stained-glass windows in Latin America: A literature overview. *Journal of Cultural Heritage*, 34, 172–181.
<https://doi.org/10.1016/j.culher.2018.04.019>
9. Curtin C. Fact or Fiction? : Glass Is a (Supercooled) Liquid - Scientific American [Internet]. [cited 2017 Nov 9]. Available from:
<https://www.scientificamerican.com/article/fact-fiction-glass-liquid/>
10. History of Glass. Glassmaking - History of Glass Making [Internet]. 2017 [cited 2017 Jul 28]. Available from: <http://www.historyofglass.com/glass-history/glass-making/>
11. Johnson J, Allred D, Turley R, Evans W, Sandberg R. Thorium-Based Thin Films as Highly Reflective Mirrors in the EUV. *MRS Proceedings*. 2005;893.
12. Meeker M, Kundu S, Maurya D, Kang M, Sosa A, Mudiyanse R *et al*. The permittivity and refractive index measurements of doped barium titanate (BT-BCN). *Optical Materials*. 2017; 73:793-798. 8
13. Bach H, Neuroth N. The Properties of Optical Glass. *Springer Science & Business Media*; 1998.
14. Eastaugh B, Sternal-Johnson C. Ferrebeekeeper [Internet]. [cited 2017 Oct 25]. Available from:
<https://ferrebeekeeper.wordpress.com/tag/manganese/GlassforEurope>. The Float Process [Internet]. [cited 2017 Jul 28]. Available from:
<http://www.glassforeurope.com/en/industry/float-process.php>

15. Kriven W. A collection of papers presented at the 66th Conference on Glass Problems. Hoboken, NJ: Wiley; 2006.
16. Varshneya AK. Fundamentals of inorganic glasses. *Academic Press*; 1994. 570
17. Ashlie Caldwell. Polymer and Ceramic Processing [Internet]. 2015 [cited 2017 Jul 28].
18. Henry Bessemer - Biography, Facts and Pictures [Internet]. [cited 2017 Nov 19]. Available from: <https://www.famousscientists.org/henry-bessemer/>
19. Zarzycki J. Special Methods of Obtaining Glasses and Amorphous Materials. In: Materials Science and Technology [Internet]. Weinheim, Germany: Wiley-VCH Verlag GmbH & Co. KGaA; 2006 [cited 2017 Aug 11]. Available from: <http://doi.wiley.com/10.1002/9783527603978.mst0091>
20. Kawashita, M., Miyaji, F., et al. (1999). Preparation of phosphorus-containing silica glass microspheres for radiotherapy of cancer by ion implantation. *Journal of Materials Science: Materials in Medicine*, 10(8), 459–463. <https://doi.org/10.1023/a:1008940823818>
21. Hines RL. Radiation Effect of Positive Ion Bombardment on Glass. *J Appl Phys.* 1957;28(587). Available from: <https://doi.org/10.1063/1.1722808>
22. Andersson O. Proceedings of the 7th International Symposium on Ceramics in Medicine. Oxford: Pergamon; 1994.
23. Andersson OH, Örjan H, Åbo akademi (1918-). Bioceramics. Volume 7, Proceedings of the 7th International Symposium on Ceramics in Medicine, Turku, Finland, July 1994. 446 p.
24. Paul A. Chemistry of glasses. Chapman and Hall; 1990 [cited 2017 Jul 30]. 367 p.

25. Muñoz, F., & Sánchez-Muñoz, L. (2019). The glass-forming ability explained from local structural differences by NMR between glasses and crystals in alkali metaphosphates. *Journal of Non-Crystalline Solids*, 503–504, 94–97.
<https://doi.org/10.1016/j.jnoncrysol.2018.09.026>
26. Martin, J. D., & Hou, F. (2018). Transition zone theory of the glass transition. *Journal of Non-Crystalline Solids*, 491, 24–33.
<https://doi.org/10.1016/j.jnoncrysol.2018.03.037>
27. Greiner W, Neise L, Stöcker H. Thermodynamics, and statistical mechanics. New York: Springer; 2005.
28. Seyler R. Assignment of the glass transition. Philadelphia, Pa: *American Society for Testing and Materials*; 1994.
29. Maes J, Castro N, De Nolf K, Walravens W, Abécassis B, Hens Z. Size and Concentration Determination of Colloidal Nanocrystals by Small-Angle X-ray Scattering. *Chemistry of Materials*. 2018;30(12):3952-3962.
30. Varshneya AK. Fundamentals of inorganic glasses. Academic Press; 1994. 570 p.
31. Pye LD, Fréchette VD, Kreidl NJ. Borate Glasses: Structure, Properties, Applications. Springer US; 1978. 648 p.
32. Zachariasen W. The Atomic Arrangement in Glass. *Journal of the American Chemical Society*. 1932;54(10):3841-3851.
33. Tomozawa M. Fundamentals of inorganic glasses. *Journal of Non-Crystalline Solids*. 1994;170(1):112.
34. Tu Y, Tersoff J, Grinstein G, Vanderbilt D. Properties of a Continuous-Random-Network Model for Amorphous Systems. *Physical Review Letters*. 1998;81(22):4899-4902.

35. Greaves G. EXAFS and the structure of glass. *Journal of Non-Crystalline Solids*. 1985;71(1-3):203-217.
36. Wright, A., Dalba, G., Rocca, F., & Vedishcheva, N. (2010). Borate Versus Silicate Glasses: Why Are They So Different? *Physics and Chemistry of Glasses*, 51(5), 233–265
37. De Graef M, McHenry M. Structure of materials. Cambridge: Cambridge University Press; 2013.
38. Ropp R. Inorganic polymeric glasses. Amsterdam: Elsevier; 1992. 321p.
39. Schneider, J., Mastelaro, V., et al. (2003). Qn distribution in stoichiometric silicate glasses: thermodynamic calculations and ²⁹Si high resolution NMR measurements. *Journal of Non-Crystalline Solids*, 325(1–3), 164–178.
[https://doi.org/10.1016/s0022-3093\(03\)00332-6](https://doi.org/10.1016/s0022-3093(03)00332-6)
40. Ebrahimi, E., & Rezvani, M. (2018). Optical and structural investigation on sodium borosilicate glasses doped with Cr₂O₃. *Spectrochimica Acta Part A: Molecular and Biomolecular Spectroscopy*, 190, 534–538.
<https://doi.org/10.1016/j.saa.2017.09.031>
41. Glass Fluxes and Modifiers. (2018, March 6). Elan Technology.
<https://www.elantechnology.com/support/technical-library/glass-fluxes-modifiers/>
42. Oey, T., Frederiksen, K. F., et al. (2019). The role of the network-modifier's field-strength in the chemical durability of aluminoborate glasses. *Journal of Non-Crystalline Solids*, 505, 279–285.
<https://doi.org/10.1016/j.jnoncrysol.2018.11.019>

43. Frolenkov K, Matyukhin S, Frolenkova L. Infrared Spectra and Differential-Thermal Analysis of Ceramic Glaze Frits. *Glass and Ceramics*. 2019;75(9-10):372-374.
44. Frolenkov, K. Y., Matyukhin, S. I., & Frolenkova, L. Y. (2019). Infrared Spectra and Differential-Thermal Analysis of Ceramic Glaze Frits. *Glass and Ceramics*, 75(9–10), 372–374. <https://doi.org/10.1007/s10717-019-00088-4>
45. Hurd P. Fulgurites. *Rocks & Minerals*. 1950;25(3-4):135-135.
46. Malitson, I. H. (1965). Interspecimen Comparison of the Refractive Index of Fused Silica*, *Journal of the Optical Society of America*, 55(10), 1205. <https://doi.org/10.1364/josa.55.001205>
47. Shelby, J. E. (2005b). *Introduction to Glass Science and Technology (Rsc Paperbacks)* (2nd ed.). Royal Society of Chemistry.
48. Deshpande, V., & Taikar, R. N. (2010). Effect of cerium oxide addition on electrical and physical properties of alkali borosilicate glasses. *Materials Science and Engineering: B*, 172(1), 6–8. <https://doi.org/10.1016/j.mseb.2010.04.003>
49. Vallet-Regí M. Ceramics for medical applications. *Journal of the Chemical Society, Dalton Transactions*. 2001;(2):97-108.
50. Nandi, S. K., Mahato, A., Kundu, B., & Mukherjee, P. (2016). Doped Bioactive Glass Materials in Bone Regeneration. *Advanced Techniques in Bone Regeneration*. <https://doi.org/10.5772/63266>
51. Wananuruksawong R, Jinawath S, et al. Fabrication of Silicon Nitride Dental Core Ceramics with Borosilicate Veneering material. *IOP Conference Series: Materials Science and Engineering*. 2011;18(19):192010.

52. Lu, H. H., El-Amin, S. F., Scott, K. D., & Laurencin, C. T. (2003). Three-dimensional, bioactive, biodegradable, polymer-bioactive glass composite scaffolds with improved mechanical properties support collagen synthesis and mineralization of human osteoblast-like cells *in vitro*. *Journal of Biomedical Materials Research*, 64A (3), 465–474. <https://doi.org/10.1002/jbm.a.10399>
53. Bretcanu, O., Misra, S. K., et al. (2009). Electrospun nanofibrous biodegradable polyester coatings on Bioglass®-based glass-ceramics for tissue engineering. *Materials Chemistry and Physics*, 118(2–3), 420–426. <https://doi.org/10.1016/j.matchemphys.2009.08.011>
54. McNeil H, Piddini E. Chemically inert glassware. *Curr Opin Cell Biol*. 1997 [cited 2017 Aug 8];9(6):914.
55. Quynh, L. M., Tien, N. T., Loc, N. B., Tho, V. Q., Lan, N. T., Thanh, P. V., Hieu, N. M., Hoang, N. L. H., & Luong, N. H. (2017). Thermal resistant efficiency of Nb-doped TiO₂ thin film-based glass window. *Journal of Science: Advanced Materials and Devices*, 2(3), 392–397. <https://doi.org/10.1016/j.jsamd.2017.07.002>
56. Ewing, R., Weber, W., & Clinard, F. (1995). Radiation effects in nuclear waste forms for high-level radioactive waste. *Progress in Nuclear Energy*, 29(2), 63–127. [https://doi.org/10.1016/0149-1970\(94\)00016-y](https://doi.org/10.1016/0149-1970(94)00016-y)
57. Weber, W. (1988). Radiation effects in nuclear waste glasses. Nuclear Instruments and Methods in Physics Research Section B: *Beam Interactions with Materials and Atoms*, 32(1–4), 471–479. [https://doi.org/10.1016/0168-583x\(88\)90257-1](https://doi.org/10.1016/0168-583x(88)90257-1)
58. Staff, I., (2014, September 23). Kurion, Inc. Turns Nuclear Waste into Glass for Safer Long-Term Storage. *Inhabitat - Green Design, Innovation*,

- Architecture, Green Building. <https://inhabitat.com/kurion-inc-turns-nuclear-waste-into-glass-for-safer-long-term-storage/comment-page-1/>
59. International symposium on ceramics in nuclear waste management. (1978). *Ceramurgia International*, 4(3), 140. [https://doi.org/10.1016/0390-5519\(78\)90099-6](https://doi.org/10.1016/0390-5519(78)90099-6)
60. Lcd TFT. Borates in borosilicate glass. Available from:
http://www.borax.com/docs/euf_pdfs/euf-borates-boratesinborosilicateglass.pdf?sfvrsn=4borosilicate-glass-34770602 @
www.thomasnet.com [Internet].
61. *Understanding Glass - Types of Glass and Glass Fabrication Processes*. (n.d.). Thomasnet.Com. <https://www.thomasnet.com/articles/plant-facility-equipment/types-of-glass/#borosilicate>
62. British Glass. (2021, February 2). *Physical Properties of Alkali Borosilicate Glasses*. <https://www.britglass.org.uk/knowledge-base/digital-library-and-information-services/physical-properties-alkali-borosilicate>
63. Boltres B. schott_fiolax-academy_modul1_a5_en-16-04-2013_einzelseiten-19-2 @ www.schott.com [Internet]. Available from:
http://www.schott.com/tubing/images/schott_fiolax-academy_modul1_a5_en-16-04-2013_einzelseiten-19-2.jpg
64. Smith W, Todorov IT. A short description of DL_POLY. Vol. 32, *Molecular Simulation*. 2006. p. 935–43.
65. Kieu, L. H., Kilymis, D., Delaye, J. M., & Peugot, S. (2014). Discussion on the Structural Origins of the Fracture Toughness and Hardness Changes in Rapidly Quenched Borosilicate Glasses: *A Molecular Dynamics Study*.

Procedia Materials Science, 7, 262–271.

<https://doi.org/10.1016/j.mspro.2014.10.034>

66. Kilymis, D., & Delaye, J. (2014b). Nanoindentation studies of simplified nuclear glasses using molecular dynamics. *Journal of Non-Crystalline Solids*, 401, 147–153. <https://doi.org/10.1016/j.jnoncrysol.2013.12.016>
67. Stoch, P., & Stoch, A. (2015). Structure and properties of Cs containing borosilicate glasses studied by molecular dynamics simulations. *Journal of Non-Crystalline Solids*, 411, 106–114. <https://doi.org/10.1016/j.jnoncrysol.2014.12.029>
68. Takada, A., Catlow, C. R. A., & Price, G. D. (1995). Computer modelling of B₂O₃. I. New interatomic potentials, crystalline phases and predicted polymorphs. *Journal of Physics: Condensed Matter*, 7(46), 8659–8692. <https://doi.org/10.1088/0953-8984/7/46/003>
69. Takada, A., Catlow, C. R. A., & Price, G. D. (1995b). Computer modelling of B₂O₃. II. Molecular dynamics simulations of vitreous structures. *Journal of Physics: Condensed Matter*, 7(46), 8693–8722. <https://doi.org/10.1088/0953-8984/7/46/004>
70. Takada A, Richet P, Atake T. New description of structural disorder in silica glass. *J Non Cryst Solids* [Internet]. 2009;355(10–12):694–9. Available from: <http://dx.doi.org/10.1016/j.jnoncrysol.2008.11.024>
71. Shao, G., Wu, X., Kong, Y., Cui, S., Shen, X., Jiao, C., & Jiao, J. (2015). Thermal shock behavior and infrared radiation property of integrative insulations consisting of MoSi₂/borosilicate glass coating and fibrous ZrO₂ ceramic substrate. *Surface and Coatings Technology*, 270, 154–163. <https://doi.org/10.1016/j.surfcoat.2015.03.008>

72. Peitl, O., & Zanotto, E. (1999). Thermal shock properties of chemically toughened borosilicate glass. *Journal of Non-Crystalline Solids*, 247(1–3), 39–49. [https://doi.org/10.1016/s0022-3093\(99\)00029-0](https://doi.org/10.1016/s0022-3093(99)00029-0)
73. Takebe, H., Harada, T., & Kuwabara, M. (2006). Effect of B₂O₃ addition on the thermal properties and density of barium phosphate glasses. *Journal of Non-Crystalline Solids*, 352(6–7), 709–713. <https://doi.org/10.1016/j.jnoncrysol.2005.11.066>
74. Zapata, J., Moretto, E., Hannan, S., Murru, L., et al. (2017). Epilepsy and intellectual disability linked protein Shrm4 interaction with GABABRs shapes inhibitory neurotransmission. *Nature Communications*, 8(1). <https://doi.org/10.1038/ncomms14536>
75. Rao, K. J. (2002). *Structural Chemistry of Glasses* (1st ed.). Elsevier Science.
76. Kalidasan, M., Asokan, K., Baskar, K., & Dhanasekaran, R. (2015). Effect of gamma ray irradiation on sodium borate single crystals. *Radiation Physics and Chemistry*, 117, 70–77. <https://doi.org/10.1016/j.radphyschem.2015.07.016>
77. Killerglass, Hi Performance Glass [Internet]. [cited 2017 Oct 25]. Available from: <http://www.killerglass.com/store/>
78. Laplante, P. A. (2005). *Comprehensive Dictionary of Electrical Engineering* (2nd ed.). CRC Press.
79. Society, E. (2003). *Semiconductor Wafer Bonding: Science, Technology, and Applications VI: Proceedings of the International Symposium*. *Electrochemical Society*.
80. Ferrari, M., & Righini, G. C. (2015). Glass-Ceramic Materials for Guided-Wave Optics. *International Journal of Applied Glass Science*, 6(3), 240–248. <https://doi.org/10.1111/ijag.12129>

81. Mittemeijer E, Somers M. Thermochemical Surface Engineering of Steels: Improving Materials Performance. *Woodhead Publishing*. 2015: 827p
82. Saravanan R. Nano semiconducting materials. 3rd ed. *Materials Research Forum LLC*;2016: 76-78 p.
83. Eckert, H. (1992). Structural characterization of noncrystalline solids and glasses using solid state NMR. *Progress in Nuclear Magnetic Resonance Spectroscopy*, 24(3), 159–293. [https://doi.org/10.1016/0079-6565\(92\)80001-v](https://doi.org/10.1016/0079-6565(92)80001-v)
84. Hwang, S. J., Fernandez, C., Amoureux, J., Cho, J., Martin, S., & Pruski, M. (1997). Quantitative study of the short-range order in B₂O₃ and B₂S₃ by MAS and two-dimensional triple-quantum MAS 11B NMR. *Solid State Nuclear Magnetic Resonance*, 8(2), 109–121. [https://doi.org/10.1016/s0926-2040\(96\)01280-5](https://doi.org/10.1016/s0926-2040(96)01280-5)
85. Pye L, Fréchette V, Kreidl N. Borate Glasses. 2012. 170-179p
86. Ferlat, G., Charpentier, T., Seitsonen, A. P., Takada, A., Lazzeri, M., Cormier, L., Calas, G., & Mauri, F. (2008). Boroxol Rings in Liquid and Vitreous B₂O₃ from First Principles. *Physical Review Letters*, 101(6). <https://doi.org/10.1103/physrevlett.101.065504>
87. Maranas, J. K., Chen, Y., Stillinger, D. K., & Stillinger, F. H. (2001). Polarization interactions and boroxol ring formation in boron oxide: A molecular dynamics study. *The Journal of Chemical Physics*, 115(14), 6578–6589. <https://doi.org/10.1063/1.1401817>
88. Swenson, J., & Börjesson, L. (2006). Fraction of Boroxol Rings in Vitreous Boron Oxide from a First-Principles Analysis of Raman and NMR Spectra. *Physical Review Letters*, 96(19). <https://doi.org/10.1103/physrevlett.96.199701>

89. Swenson, J., & Börjesson, L. (1998). Intermediate range ordering in a network glass. *Journal of Non-Crystalline Solids*, 223(3), 223–229.
[https://doi.org/10.1016/s0022-3093\(97\)00432-8](https://doi.org/10.1016/s0022-3093(97)00432-8)
90. Cho, J. Y., Moon, M. H., Lee, Y. H., Kim, K. W., & Kim, S. H. (2009). Measurement of compensatory hyperplasia of the contralateral kidney: usefulness for differential diagnosis of fetal unilateral empty renal fossa. *Ultrasound in Obstetrics and Gynecology*, 34(5), 515–520.
<https://doi.org/10.1002/uog.7336>
91. Peter Puls, S., & Eckert, H. (2007). Spatial distribution of lithium ions in glasses studied by ${}^7\text{Li}\{6\text{Li}\}$ spin echo double resonance. *Physical Chemistry Chemical Physics*, 9(30), 3992. <https://doi.org/10.1039/b705338j>
92. Pisarska, J., Kos, A., & Pisarski, W. A. (2014). Spectroscopy and energy transfer in lead borate glasses doubly doped with $\text{Dy}^{3+}\text{--Tb}^{3+}$ and $\text{Tb}^{3+}\text{--Eu}^{3+}$ ions. *Spectrochimica Acta Part A: Molecular and Biomolecular Spectroscopy*, 129, 649–653. <https://doi.org/10.1016/j.saa.2014.04.142>
93. Abdelghany, A., & Hammad, A. H. (2015). Impact of vanadium ions in barium borate glass. *Spectrochimica Acta Part A: Molecular and Biomolecular Spectroscopy*, 137, 39–44.
<https://doi.org/10.1016/j.saa.2014.08.012>
94. Faraday M. Experimental researches in electricity. Santa Fe, N.M.: Green Lion Press; 2000. 1-20 p.
95. Jagadeesha G. International Journal of Engineering and Advanced Research Technology (IJEART). *International Journal of Engineering and Advanced Research Technology (IJEART)*. 2018;3(5):228-232.

96. Rezayati S, Hajinasiri R. Boric acid as a highly efficient and reusable catalyst for the one-pot synthesis of 1,8-dioxo-octahydroxanthenes under solvent-free conditions. *Iranian Journal of Catalysis*. 2014;4(3):157-162.
97. Palmer J. Boric acid catalysis of decomposition of the N-nitrosohydroxylamine-N-sulfonate anion. *Journal of Catalysis*. 1978;53(3):345-355.
98. Zachariasen W. The Crystal Lattice of Boric Acid, BO_3H_3 . *Zeitschrift für Kristallographie - Crystalline Materials*. 1934;88(1-6):150-161
99. Bethell D, Sheppard N. The infra-red spectrum and structure of boric acid. *Transactions of the Faraday Society*. 1955; 51:9.
100. Kawaguchi M, Ohnishi K, Yamada K, Mura Matsu Y. Intercalation Chemistry and Electronic Structure of Graphite-Like Layered Material $\text{BC}[\text{sub } 2]\text{N}$. *Journal of The Electrochemical Society*. 2010;157(3): P13.
101. Lipp, A.; Schwetz, K. A.; Hunold, K.: *Journal of the European Ceramic Society* 5 (1989) Nr. 1, S. 3 - 9.
102. Joo C, Werner-Zwanziger U, Zwanziger J. The ring structure of boron trioxide glass. *Journal of Non-Crystalline Solids*. 2000;261(1-3):282-286.
103. Gautam, C., Yadav, A. K., & Singh, A. K. (2012). A Review on Infrared Spectroscopy of Borate Glasses with Effects of Different Additives. *ISRN Ceramics*, 2012, 1–17. <https://doi.org/10.5402/2012/428497>
104. Jensen F. Introduction to computational chemistry. 3rd ed. Wiley; 2017. 20-100 p.
105. Atkins P and de Paula, J. Physical Chemistry for the Life Sciences. New York, N.Y. W. H. Freeman Company, 2006. (469-472).

106. Democritus: The Radial Distribution Function [Internet]. [cited 2017 Aug 15].

Available from:

<http://www.comsoc.man.ac.uk/~lucky/Democritus/Theory/rdf.html>

107. Tarantino N, Tinevez J-Y, Crowell EF, et al. TNF and IL-1 exhibit distinct ubiquitin requirements for inducing NEMO–IKK supramolecular structures. *J Cell Biol* (2014); 204(2). Available from:

<http://jcb.rupress.org/content/204/2/231>

108. etomica.org. Mean square displacement [Internet]. [cited 2017 Aug 3].

Available from:

<http://www.etomica.org/app/modules/sites/Ljmd/Background2.html>

109. Catlow R, Bell R, Cora F, French S., Slater B, Sokol A. 25 Computer modelling of inorganic materials. Annu Reports Sect “A” (*Inorganic Chem.* 2005;513–47.

110. Todorov IT, Smith W, Trachenko K, Dove MT. DL_POLY. *J Mater Chem* [Internet]. 2006; 16:1911–8. Available from:

http://www.ccp5.ac.uk/DL_POLY/

111. Humphrey W, Dalke A, Schulten K. VMD: Visual molecular dynamics. *J Mol Graph.* 1996;14(1):33–8.

112. Momma, K., & Izumi, F. (2011). VESTA 3 for three-dimensional visualization of crystal, volumetric and morphology data. *Journal of Applied Crystallography*, 44(6), 1272–1276.

<https://doi.org/10.1107/s0021889811038970>

113. Ferlat, G., Seitsonen, A. P., Lazzeri, M., & Mauri, F. (2012). Hidden polymorphs drive vitrification in B₂O₃. *Nature Materials*, 11(11), 925–929.

<https://doi.org/10.1038/nmat3416>

114. van Beest, B. W. H., Kramer, G. J., & van Santen, R. A. (1990). Force fields for silicas and aluminophosphates based on ab initio calculations. *Physical Review Letters*, 64(16), 1955–1958.
<https://doi.org/10.1103/physrevlett.64.1955>
115. Herzbach, D., Binder, K., & Müser, M. H. (2005). Comparison of model potentials for molecular-dynamics simulations of silica. *The Journal of Chemical Physics*, 123(12), 124711. <https://doi.org/10.1063/1.2038747>
116. Sanders, M. J., Leslie, M., & Catlow, C. R. A. (1984). Interatomic potentials for SiO₂. *Journal of the Chemical Society, Chemical Communications*, 19, 1271. <https://doi.org/10.1039/c39840001271>
117. Machon, D., Meersman, F., Wilding, M., Wilson, M., & McMillan, P. (2014). Pressure-induced amorphization and polyamorphism: Inorganic and biochemical systems. *Progress in Materials Science*, 61, 216–282.
<https://doi.org/10.1016/j.pmatsci.2013.12.002>
118. Pattison P, Hansen N, Schneider J. Identifying the bonding in diamond and silicon using compton scattering experiments. *Chemical Physics*. 1981;59(3):231-242.
119. Tilocca A, De Leeuw NH, Cormack AN. Shell-model molecular dynamics calculations of modified silicate glasses. *Phys Rev B - Condens Matter Mater Phys*. 2006;73(10).
120. Wang, M., Anoop Krishnan, N., Wang, B., Smedskjaer, M. M., Mauro, J. C., & Bauchy, M. (2018). A new transferable interatomic potential for molecular dynamics simulations of borosilicate glasses. *Journal of Non-Crystalline Solids*, 498, 294–304. <https://doi.org/10.1016/j.jnoncrysol.2018.04.063>

121. Kieu, L. H., Delaye, J. M., Cormier, L., & Stolz, C. (2011). Development of empirical potentials for sodium borosilicate glass systems. *Journal of Non-Crystalline Solids*, 357(18), 3313–3321.
<https://doi.org/10.1016/j.jnoncrysol.2011.05.024>
122. Guillot, B., & Sator, N. (2007). A computer simulation study of natural silicate melts. Part II: High pressure properties. *Geochimica et Cosmochimica Acta*, 71(18), 4538–4556. <https://doi.org/10.1016/j.gca.2007.05.029>
123. Milberg, M. E., & Meller, F. (1959). Structure of Vitreous $B_2O_3 \cdot \frac{1}{3}H_2O$. *The Journal of Chemical Physics*, 31(1), 126–129.
<https://doi.org/10.1063/1.1730278>
124. Vegiri, A., Varsamis, C. P. E., & Kamitsos, E. I. (2005). Composition and temperature dependence of cesium-borate glasses by molecular dynamics. *The Journal of Chemical Physics*, 123(1), 014508.
<https://doi.org/10.1063/1.1943414>
125. Patzek T. Fick's Diffusion Experiments Revisited —Part I. *Advances in Historical Studies*. 2014;03(04):194-206.
126. Möncke, D., & Tricot, G. (2015). On the connectivity of borate tetrahedra in borate and borosilicate glasses. *European Journal of Glass Science and Technology Part B Physics and Chemistry of Glasses*, 56.
<https://doi.org/10.13036/17533562.56.5.203>
127. Wolff, R., Radeaglia, R., & Vogel, C. (1990). Theoretical interpretation of ^{29}Si NMR chemical shifts of aluminosilicates—III. semiempirical determination of the paramagnetic shielding constant. *Journal of Physics and Chemistry of Solids*, 51(1), 5103–5111. [https://doi.org/10.1016/0022-3697\(90\)90082-Q](https://doi.org/10.1016/0022-3697(90)90082-Q)

128. Brown, D. I. (2006). *The Chemical Bond in Inorganic Chemistry: The Bond Valence Model* (International Union of Crystallography Monographs on Crystallography, 12). Oxford University Press.
129. Johnson, P. A., Wright, A. C., & Sinclair, R. N. (1982). A neutron diffraction investigation of the structure of vitreous boron trioxide. *Journal of Non-Crystalline Solids*, 50(3), 281–311. [https://doi.org/10.1016/0022-3093\(82\)90092-8](https://doi.org/10.1016/0022-3093(82)90092-8)
130. Kulikova LF, Dyuzheva TI, Nikolaev N a., Brazhkin V. Single-crystal growth of the high-pressure phase B₂O₃ II. *Crystallogr Reports*. 2012;57(2):332–5.
131. Lu, K., & Li, Y. (1998). Homogeneous Nucleation Catastrophe as a Kinetic Stability Limit for Superheated Crystal. *Physical Review Letters*, 80(20), 4474–4477. <https://doi.org/10.1103/physrevlett.80.4474>
132. Landau, D. P., Mon, K., & Schüttler, H. (2012). Computer Simulation Studies in Condensed-Matter Physics VIII: Recent Developments Proceedings of the Eighth Workshop Athens, GA, USA, February 20–24, 1995, *Springer Proceedings in Physics*.
133. Pauling, L. (1929). The Principles Determining the Structure of Complex Ionic Crystals. *Journal of the American Chemical Society*, 51(4), 1010–1026. <https://doi.org/10.1021/ja01379a006>
134. Toofan J. A Simple Expression between Critical Radius Ratio and Coordination Number. *Journal of Chemical Education*. 1994;71(2):147.
135. Maranas, J. K., Chen, Y., Stillinger, D. K., & Stillinger, F. H. (2001b). Polarization interactions and boroxol ring formation in boron oxide: A molecular dynamics study. *The Journal of Chemical Physics*, 115(14), 6578–6589. <https://doi.org/10.1063/1.1401817>

136. Kuo, C. T., Neumann, M., Balamurugan et al. (2016). Exfoliation and Raman Spectroscopic Fingerprint of Few-Layer NiPS₃ Van der Waals Crystals. *Scientific Reports*, 6(1). <https://doi.org/10.1038/srep20904>
137. Borosilicate Glass Fiber 1.5 micron|Filters | Environmental Express [Internet]. [cited 2018 Jun 18]. Available from: <http://www.envexp.com/products/7-General-Lab-Supplies/FIL-Filters/BORO-Borosilicate-Glass-Fiber-1-5-micron>
138. Momma K, Izumi F. VESTA 3 for three-dimensional visualization of crystal, volumetric and morphology data. *J Appl Crystallogr.* 2011;44(6):1272–6. Available from: <http://scripts.iucr.org/cgi-bin/paper?S0021889811038970>
139. Gurr, G. E., Montgomery, P. W., Knutson, C. D., & Gorres, B. T. (1970). The crystal structure of trigonal diboron trioxide. *Acta Crystallographica Section B Structural Crystallography and Crystal Chemistry*, 26(7), 906–915. <https://doi.org/10.1107/s0567740870003369>
140. Miyake, M., Suzuki, T., Morikawa, H., Takagi, Y., & Marumo, F. (1984). Structural analysis of molten B₂O₃. *Journal of the Chemical Society, Faraday Transactions 1: Physical Chemistry in Condensed Phases*, 80(7), 1925. <https://doi.org/10.1039/f19848001925>
141. Boron Oxides, Hydroxides, and Oxyanions [Internet]. [cited 2018 Jul 11]. Available from: <https://archive.cnx.org/contents/3e34c618-09b0-4aa6-8708-2f830381d0f0@3/boron-oxides-hydroxides-and-oxyanions>
142. Le Roux, S., & Jund, P. (2010). Ring statistics analysis of topological networks: New approach and application to amorphous GeS₂ and SiO₂ systems. *Computational Materials Science*, 49(1), 70–83. <https://doi.org/10.1016/j.commatsci.2010.04.023>

143. Skuja, L., Hirano, M., Hosono, H., & Kajihara, K. (2005). Defects in oxide glasses. *Physica Status Solidi (c)*, 2(1), 15–24.
<https://doi.org/10.1002/pssc.200460102>
144. Du J, Cormack A. The medium range structure of sodium silicate glasses: a molecular dynamics simulation. *Journal of Non-Crystalline Solids*. 2004;349:66-79.
145. Lei, X., Jee, Y., & Huang, K. (2015). Amorphous Na₂Si₂O₅ as a fast Na⁺ conductor: an ab initio molecular dynamics simulation. *Journal of Materials Chemistry A*, 3(39), 19920–19927. <https://doi.org/10.1039/c5ta04474j>
146. Allen MP. John von Neumann Institute for Computing [Internet]. Vol. 23, Lecture Notes, Norbert Attig. 2004 [cited 2018 Dec 27]. Available from: <http://www.fz-juelich.de/nic-series/volume23>
147. Zhang, S., Li, H., Li, H., Zhou, S., & Cao, X. (2007). Calculation of the Bulk Modulus of Simple and Complex Crystals with the Chemical Bond Method. *The Journal of Physical Chemistry B*, 111(6), 1304–1309.
<https://doi.org/10.1021/jp0651539>
148. Sousa SF, Fernandes PA, Ramos MJ. General performance of density functionals. *J Phys Chem A*. 2007;111(42):10439–52.
149. Hummel R. Electronic properties of materials. 4th ed. *Springer Science*; 2011.p40-50
150. Hafner J. Chem Inform Abstract: Ab-initio Simulations of Materials Using VASP: Density-functional Theory and Beyond. *Chem Inform*. 2008;39(47).
151. Tang W, Sanville E, and Henkelman G, A grid-based Bader analysis algorithm without lattice bias, *J. Phys.: Condens. Matter* 21, 084204 (2009).

152. Kresse G, Furthmuller J. VASP the Guide. Comput Physics, Fac Physics, Univ [Internet]. 2012; Available from: <http://scholar.google.com/scholar?hl=en&btnG=Search&q=intitle:VASP+the+GUIDE#0>
153. Perdew JP, Ruzsinszky A, Csonka GI, Vydrov OA, Scuseria GE, Constantin LA. Restoring the density-gradient expansion for exchange in solids and surfaces (Physical Review Letters (2008) 100 (136406)). Vol. 102, *Physical Review Letters*. 2009.
154. Mak, T. C. W., Lam, C. N., & Lau, O. W. (1977). Drinking-straw polyhedral models in structural chemistry. *Journal of Chemical Education*, 54(7), 438. <https://doi.org/10.1021/ed054p438>
155. Features - VESTA [Internet]. [cited 2018 Nov 22]. Available from: <http://jp-minerals.org/vesta/en/features.html>
156. Momma, K., & Izumi, F. (2011b). VESTA 3for three-dimensional visualization of crystal, volumetric and morphology data. *Journal of Applied Crystallography*, 44(6), 1272–1276. <https://doi.org/10.1107/s0021889811038970>
157. Cherednichenko K, Le Godec Y, Kalinko A, Mezouar M, Solozhenko V. Orthorhombic boron oxide under pressure: In situ study by X-ray diffraction and Raman scattering. *Journal of Applied Physics*. 2016;120(17):175901.
158. Wright AC, Sinclair RN, Stone CE, Knight KS, Polyakova IG, Vedishcheva NM. Structure of crystalline caesium enneaborate. *Physics and Chemistry of Glasses*. 2003.

159. Aziz, M. J., Nygren, E., Hays, J. F., & Turnbull, D. (1985). Crystal growth kinetics of boron oxide under pressure. *Journal of Applied Physics*, 57(6), 2233–2242. <https://doi.org/10.1063/1.334368>
160. Krogh-Moe, J., & Ihara, M. (1967). The crystal structure of caesium enneaborate, $\text{Cs}_2\text{O}\cdot 9\text{B}_2\text{O}_3$. *Acta Crystallographica*, 23(3), 427–430. <https://doi.org/10.1107/s0365110x67002907>
161. Johnson, N. W. (1966). Convex Polyhedra with Regular Faces. *Canadian Journal of Mathematics*, 18, 169–200. <https://doi.org/10.4153/cjm-1966-0218>
162. Li, D., & Ching, W. Y. (1996). Electronic structures and optical properties of low- and high-pressure phases of crystalline B_2O_3 . *Phys. Rev. B*.
163. Tokuda, Y., Takahashi, Y., Masai, H., Kaneko, S., Ueda, Y., Fujimura, S., & Yoko, T. (2015). Local structure of alkalis in mixed-alkali borate glass to elucidate the origin of mixed-alkali effect. *Journal of Asian Ceramic Societies*, 3(4), 412–416. <https://doi.org/10.1016/j.jascer.2015.09.002>
164. Kanishcheva, A.S., Egorysheva, et al. (2004). Crystal structure of the metastable polymorph $\gamma\text{-Na}_2\text{O}\cdot 2\text{B}_2\text{O}_3$. *Zhurnal Neorganicheskoy Khimii*, 49(6), 1006-1011.
165. Fang B. On The Crystal Structure of Sodium Metaborate, NaBO_2 . *Journal of the American Ceramic Society*. 1937;20(1-12):214-214.
166. Penin N, Touboul M, Nowogrocki G. Crystal Structure of Two New Sodium Borates $\text{Na}_3\text{B}_7\text{O}_{12}$ and $\text{Na}_2\text{Tl}_2\text{B}_{10}\text{O}_{17}$. *ChemInform*. 2004;35(11).
167. Alvarez S. Polyhedra in (inorganic) chemistry. *Dalton Transactions*. 2005;(13):2209.
168. Ospadov E, Tao J, Staroverov V, Perdew J. Visualizing atomic sizes and molecular shapes with the classical turning surface of the Kohn–Sham

- potential. *Proceedings of the National Academy of Sciences*. 2018;115(50): E11578-E11585.
169. El-Falaky, G. E., & Guirguis, O. W. (2012). Effect of zinc on the physical properties of borate glasses. *Journal of Non-Crystalline Solids*, 358(15), 1746–1752. <https://doi.org/10.1016/j.jnoncrysol.2012.05.009>
170. Schmidt-Baese, D., & Klingebiel, U. (1989). ChemInform Abstract: Synthesis of (SiNSiO) Four-Membered Rings. Crystal Structure of Cyclic (Me₃C)₂SiOSi (CMe₃)₂NSiMe₃. *ChemInform*, 20(36).
<https://doi.org/10.1002/chin.198936267>
171. Koops C. On the Dispersion of Resistivity and Dielectric Constant of Some Semiconductors at Audiofrequencies. *Physical Review*. 1951;83(1):121-124.
172. Gross E, Dreizler R. Density Functional Theory. Boston, MA: Springer US; 995.
173. Brown, J. M., Abramson, E. H., & Angel, R. J. (2006). Triclinic elastic constants for low albite. *Physics and Chemistry of Minerals*, 33(4), 256–265.
<https://doi.org/10.1007/s00269-006-0074-1>
174. Levitin, V. (2013). Interatomic Bonding in Solids. Wiley.
175. Darmawan A. Shear yield strength, modulus of rigidity, and modulus of rupture of nodular cast iron on Magnesium Addition. *International Journal of Emerging Trends in Engineering Research*. 2020;8(6):2365-2369.
176. Hebbache M. Shear modulus and hardness of crystals: density functional calculations [Internet]. [cited 2018 Dec 21]. Available from:
www.elsevier.com/locate/ssc

177. Jaccani, S. P., & Huang, L. (2016). Understanding Sodium Borate Glasses and Melts from Their Elastic Response to Temperature. *International Journal of Applied Glass Science*, 7(4), 452–463. <https://doi.org/10.1111/ijag.12250>
178. Greene, R., & Luo, H. (1994). Pressure Induced Metastable Amorphization of BAs: Evidence for a Kinetically Frustrated Phase Transformation. *APS Physics*. Published. <https://doi.org/10.1103/PhysRevLett.73.2476>
179. Miller, A. J., Saunders, G. A., & Yogurtcu, Y. K. (1981). Pressure dependences of the elastic constants of PbTe, SnTe and Ge_{0.08}Sn_{0.92}Te. *Journal of Physics C: Solid State Physics*, 14(11), 1569–1584. <https://doi.org/10.1088/0022-3719/14/11/018>
180. Henkelman G, Arnaldsson A, Jónsson H. A fast and robust algorithm for Bader decomposition of charge density. *Comput Mater Sci* [Internet]. 2006 Jun 1 [cited 2019 Jan 25];36(3):354–60. Available from: <https://www.sciencedirect.com/science/article/pii/S0927025605001849>
181. Henkelman, G., Arnaldsson, A., & Jónsson, H. (2006). A fast and robust algorithm for Bader decomposition of charge density. *Computational Materials Science*, 36(3), 354–360. <https://doi.org/10.1016/j.commatsci.2005.04.010>
182. Zhang L, Xiang L, Hang C, Liu W, Huang W, Pan Y. From Discrete Molecular Cages to a Network of Cages Exhibiting Enhanced CO₂ Adsorption Capacity. *Angewandte Chemie*. 2017;129(27):7895-7899.
183. Taylor, M. J., Grigg, J. A., & Rickard, C. E. (1992). The structure of the cage-like complex anion formed by sodium borate and 1,1,1-tris(hydroxymethyl)ethane. *Polyhedron*, 11(8), 889–892. [https://doi.org/10.1016/s0277-5387\(00\)83337-9](https://doi.org/10.1016/s0277-5387(00)83337-9)

184. House, J. E., & House, K. A. (2010). Boron. *Descriptive Inorganic Chemistry*, 189–205. <https://doi.org/10.1016/b978-0-12-088755-2.00008-2>
185. Prewitt C, Shannon R. Crystal structure of a high-pressure form of B₂O₃. *Acta Crystallographica Section B Structural Crystallography and Crystal Chemistry*. 1968;24(6):869-874.
186. Leach A. Molecular modelling. Harlow: Pearson/Prentice Hall; 2009.
187. Faggella M, Gigliotti R, Morrone C, Spacone E. Mohr Circle-based Graphical Vibration Analysis and Earthquake Response of Asymmetric Systems. *Procedia Engineering*. 2017; 199:128-133.